CDF/ANAL/EXOTIC/PUBLIC/7953
September 5, 2006
version 2.1

Search for Gluino and Squark Production in Multijets Plus Missing $\mathrm{E_T}$ Final States

Xavier Portell, Carlos Sánchez, Mario Martínez
(IFAE-Barcelona)

Abstract

We present a search for squarks and gluinos in proton-antiproton collisions with a center-of-mass energy of 1.96 TeV at the Tevatron, based on 371 pb^{-1} of data collected by the CDF detector during Run II. Events with multiple jets of hadrons and large missing energy in the final state are studied within the framework of minimal supergravity and assuming R-parity conservation. No excess with respect to Standard Model predictions is observed. In a mSUGRA scenario with $A_0 = 0$, $\mu < 0$ and $\tan\beta = 5$, we exclude masses up to 380 GeV/c^2 at 95% C.L. in the region where gluino and squark masses are similar.

1 Introduction

The Standard Model (SM) of particle physics is remarkably successful in describing the presently known phenomena. However, it will have to be extended to describe the physics at arbitrarily high energies. Over the past few decades, Supersymmetry [1] has become the leading candidate to undertake this job as fundamental theory beyond the SM. The Minimal Supersymmetric Standard Model (MSSM) is a straightforward supersymmetrization of the SM [2]. It is minimal in the sense that the number of superfields and interactions are kept to the smallest number possible. Even with this, a general parametrization of supersymmetry breaking in the MSSM introduces about 100 free parameters. This is not particularly interesting as the predictive power of a theory with so many free parameters is quite limited. Thus, models with much fewer parameters have been constructed. Probably, the most popular among these models is Minimal Supergravity (mSUGRA) [3].

In this analysis, we consider the framework of mSUGRA with R-parity conservation. This model is characterized by five free parameters described as follows:

- m_0: the common scalar mass at the GUT scale;
- $m_{1/2}$: the common gaugino mass at the GUT scale;
- A_0: the common soft trilinear SUSY breaking parameter at the GUT scale;
- tan β: the ratio of the Higgs vacuum expectation values at the electroweak scale;
- sign μ: the sign of the Higgsino mass term.

At the Tevatron, supersymmetric particles could be produced according to the following partonic reactions, where superparticles are created in pairs as consequence of conserving R-parity:

$$\begin{aligned}
\tilde{q}\bar{\tilde{q}} \text{ production:} \quad & q_i + \bar{q}_j \longrightarrow \tilde{q}_k + \bar{\tilde{q}}_l && (1)\\
& g + g \longrightarrow \tilde{q}_i + \bar{\tilde{q}}_i && (2)\\
\tilde{q}\tilde{q} \text{ production:} \quad & q_i + q_j \longrightarrow \tilde{q}_i + \tilde{q}_j \text{ and } c.c. && (3)\\
\tilde{g}\tilde{g} \text{ production:} \quad & q_i + \bar{q}_i \longrightarrow \tilde{g} + \tilde{g} && (4)\\
& g + g \longrightarrow \tilde{g} + \tilde{g} && (5)\\
\tilde{q}\tilde{g} \text{ production:} \quad & q_i + g \longrightarrow \tilde{q}_i + \tilde{g} \text{ and } c.c. && (6)
\end{aligned}$$

In mSUGRA, all supersymmetric particles except the neutralino are unstable and therefore will decay into their SM counterparts right after being produced. This cascade will result in a final state consisting on several jets, which come from squarks and/or gluinos, plus missing transverse energy ($\not\!\!E_T$) coming from the neutralinos which leave CDF undetected.

In this note we present the results of searching for Supersymmetry in the mSUGRA framework at CDF. This is an update of the blind analysis described on [4]. This update includes all the CDF Run II data collected before the beginning of 2005. Also, a complete scan of the $M_{\tilde{q}}$ vs $M_{\tilde{g}}$ space has been done. The analysis is a continued investigation of a similar study performed during Run I [5]. That analysis excluded gluino masses below 195 GeV/c^2 (95 % C.L) for any squark mass. In the case of $M_{\tilde{g}} \approx M_{\tilde{q}}$, gluino masses were excluded below 300 GeV/c^2.

The structure of the note is as follows. Section 2 describes the trigger and event selection. A description of the Monte Carlo samples used in this study is given in section 3. Sections 4 and 5 are devoted to a detailed description of the selection cuts and signal to background optimization. Section 6 shows some signal studies and section 7 describes the systematic uncertainties associated with the analysis. A summary with the number of signal and background events expected in the data is given in section 8. Finally, we give our results, and set new limits for the masses of squarks and gluinos.

2 Trigger and Event Pre-selection

The analysis presented on this note is based on 371 pb^{-1} of Run II data collected before the beginning of 2005. The run number is in the range 138809 - 186598 and the DQM GoodRun List v7 (0,0,0,0) was used. There is roughly ten million events in this sample.

2.1 Trigger

The three-level trigger logic that was employed to collect the event sample requires the presence of at least two jets in the final state together with large $\not\!\!E_T$. Table 1 shows in detail the trigger requirements at the different levels.

Trigger Level	requirement	Prescale
L1	MET 25	1
L2	TWO-JET10 .and. L1-MET25	1
L3	MET 35	1

Table 1: Summary of the MET35 trigger logic used in collecting the data.

The stability of the trigger cross section versus time was studied. Figure 1 shows the effective cross section of the MET35 trigger versus run number. No significant dependence of the measured cross section with the run number is observed.

2.2 Pre-selection Cuts

Events are pre-selected using the following basic criteria:

- A class 12 Zvertex is required with z-component, V_z, in the region $|V_z| < 60$ cm. Events where no vertex is found are excluded.

- At least three jets with corrected transverse energy, E_T^{jet}, above 25 GeV and pseudorapidity in the range $|\eta^{\mathrm{jet}}| < 2.0$. Jets are reconstructed using the CDF Run I JETCLU algorithm with a radius R=0.7 and the jet transverse energy is corrected back to the hadron level (level 5) using the default CDF jet correction package version 04a.

- At least one of the three leading jets is required to be central with a pseudorapidity in the region $|\eta^{\mathrm{jet}}| < 1.1$.

- Corrected missing transverse energy, $\not{E}_{\mathrm{T}}$, above 70 GeV. The threshold is dictated by the trigger and is defined to be away from the trigger turn-on curve, (see appendix A). $\not{E}_{\mathrm{T}}$ is defined as the norm of $-\sum_i E_T^i \cdot \vec{n}_i$, where $\vec{n}_i$ is the unit vector in the azimuthal plane that points from the beamline to the i-th calorimeter tower. A further correction is applied to $\not{E}_{\mathrm{T}}$ by using the average-corrected jet transverse energies:

$$\not{E}_{\mathrm{T}} = \not{E}_{\mathrm{T}}{}^{\mathrm{raw}} - \sum_{\mathrm{i=1}}^{\mathrm{N_{jets}}} \mathrm{E}_{\mathrm{T_i}}^{\mathrm{uncorr}} + \sum_{\mathrm{i=1}}^{\mathrm{N_{jets}}} \mathrm{E}_{\mathrm{T_i}}^{\mathrm{corr}}$$

The following requirements are added in order to remove contributions from beam-halo, beam-gas and cosmic rays. These cuts remove events with insufficient electromagnetic energy deposition in the calorimeter or insufficient tracking activity, inconsistent with jets of hadrons coming from the interaction point (see appendix B).

- Averaged electromagnetic fraction of jets, defined as EEMF $= \frac{\sum_{\mathrm{jets}} E_T^{\mathrm{jet}} \cdot f_{\mathrm{emf}}^{\mathrm{jet}}}{\sum_{\mathrm{jets}} E_T^{\mathrm{jet}}}$, greater than 0.15, where the sum runs over the three leading jets in the event.

- Averaged jet charge fraction, ECHF ≥ 0.15. The quantity ECHF is defined for central jets ($|\eta^{\mathrm{jet}}| < 1.1$) as the averaged ratio between the momentum of the jet, as computed using tracks, and the jet transverse energy:

$$\mathrm{ECHF} = \frac{1}{N_{\mathrm{jets}}} \sum_{\mathrm{jets}} \frac{\sum_{\mathrm{tracks}} P_T^{\mathrm{track}}}{E_T^{\mathrm{jet}}}, \text{ where } |\eta^{\mathrm{jets}}| < 1.1 \qquad (7)$$

  where only tracks in a cone of radius 0.4 around the jet's direction, and passing the following quality cuts are considered:

  - $|z - z_0| < 2$ cm,
  - $0.3 < p_T < 500$ GeV/c,
  - $|\eta| < 1.5$,
  - $d_0 < 2$ cm,

– Number of axial + stereo hits > 20.

Above, $|z - z_0|$ is the difference in the z-direction between the track and the vertex, and d_0 is the impact parameter of the track.

3 Monte Carlo Samples

A large amount of Monte Carlo samples are needed to perform this analysis. In particular, the generation and simulation of the different signal samples for different squark, and gluino masses translate into a substantial amount of CPU time. In addition, and thanks to the help of the LHC Tier 1 center in Barcelona, it was possible to generate enough luminosity for the different QCD multijet background samples. For the rest of the background processes, and when possible, samples generated by other analysis groups were used. Here, we give a detailed description of the different samples.

3.1 Signal Monte Carlo Samples

The study was limited to the mSUGRA scenario ($M_{\tilde{q}} \gtrsim M_{\tilde{g}}$) for which five parameters (m_0, $m_{1/2}$, A_0, sgn(μ) and $\tan\beta$) are sufficient to determine the spectra of particle masses and interaction couplings. Following the values adopted by other CDF SUSY analyses in Run II, we set $A_0 = 0$, sgn(μ)=-1 and $\tan\beta = 5$. In addition, 2-to-2 processes involving stop and sbottom production were excluded.

The gluino-squark mass plane is then scanned via variations of m_0 and $m_{1/2}$ parameters. Two different leading-order Monte Carlo programs, ISAJET [6] and PYTHIA [7], were initially considered to generate mSUGRA points. More than 100 different point were generated in a grid with different squark and gluino masses up to approximately 500 GeV/c^2 (see Figure 2). The predicted squark and gluino masses by ISAJET and PYTHIA agree well with differences smaller than 1%, see Figure 3. The observed differences are negligible for this study and can be attributed to the different numerical methods employed in solving the renormalization group equations that determine the running masses.

PYTHIA Monte Carlo was used to generate the different mSUGRA samples, with CTEQ5L PDFs, initial-state gluon radiation and underlying event settings as determined by Tune A, and $\Lambda_{QCD} = 146$ MeV [1]. The comparison between ISAJET and PYTHIA hadronic final states (see Figure 4) indicates that, for fixed squark and gluino masses, ISAJET produces much harder distributions than PYTHIA, which translates into a significantly larger signal selection efficiencies and better exclusion limits when ISAJET is used instead of PYTHIA. This is attributed to the limited (non-proper) initial- and final-state gluon radiation in ISAJET, compared to that implemented in PYTHIA, which makes ISAJET not suitable for this analysis. Additional PYTHIA samples were generated with enhanced and reduced initial- and

[1]This follows the standards suggested by the Top and Higgs Working Groups.

final-state gluon radiation to determine the systematic uncertainty due to the parton shower modeling in the Monte Carlo.

We used PROSPINO [8] to calculate the next-to-leading order (NLO) cross section for squark and gluino production at the Tevatron. PROSPINO does not include the 3^{rd} squark family in its calculations. It divides squark and gluino production into four different subprocesses: gluino-gluino (gg), squark-gluino (sg), squark-squark (ss), and squark-antisquark (sb), and the cross section is calculated for each of these subprocesses separately. Using the different cross sections, σ^i_{NLO} with $i = gg, sg, ss$, and sb, we calculate the number of expected events of each subprocess for 371 pb^{-1}. After dividing the PYTHIA samples in a similar way, we normalize them according to:

$$\text{PYTHIA NLO} = \sum_{\mathrm{i}=1}^{4} \frac{\text{Events }^{\mathrm{i}}_{\mathrm{NLO}}}{\text{Events }^{\mathrm{i}}_{\mathrm{LO}}} \tag{8}$$

where i runs through the four different subprocesses explained before. We believe the shape of the PYTHIA distributions for each of the four contributions but not the cross section. We have set the default value of the renormalization scale as follows:

- gluino-gluino (gg): $\mu = \mathrm{M}_{\tilde{\mathrm{g}}}$
- squark-gluino[2] (sg): $\mu = 0.5[\mathrm{M}_{\tilde{\mathrm{g}}} + \overline{\mathrm{M}}_{\tilde{\mathrm{q}}}]$
- squark-squark (ss): $\mu = \overline{\mathrm{M}}_{\tilde{\mathrm{q}}}$ (in this subprocess we also find antisquark-antisquark production)
- squark-antisquark (sb): $\mu = \overline{\mathrm{M}}_{\tilde{\mathrm{q}}}$

where $\overline{\mathrm{M}}_{\tilde{q}}$ is the average of all eight squark masses considered.

3.2 Background Monte Carlo

The SM background in this analysis is dominated by QCD[3] multijet processes where the observed $\not\!\!E_{\mathrm{T}}$ comes from an inadequate determination of the jet transverse energies. In addition, there are contributions from Z and W production in association with jets, top production and diboson production. In particular, the contribution from Z + 3 jets production, where the Z decays into neutrinos, constitutes an irreducible background to the mSUGRA signal. A list of the most relevant background processes is given in table 2.

The Monte Carlo programs used for the background processes are leading order generators. Thus, the samples must be normalized to next-to-leading order calculations. The different boson + jets and diboson samples were normalized using LO-to-NLO k-factors determined by MCFM [4] [9]. The default value of the renormalization

[2] $\overline{\mathrm{M}}_{\tilde{q}}$ indicates the average squark masses for the first two squark generations.

[3] A large effort was put forward to increase the statistics of the QCD sample at relatively low $\hat{p}_T$. As a result several million QCD events were generated requiring $\not\!\!E_{\mathrm{T}} > 25$ GeV.

[4] MCFM provides k-factor upto two partons in the final state. However, as shown by separate measurements at DØ, the use of k-factors for the three parton on is a reasonable approximation.

Sample	Dataset and MC Gen.	Lumi (pb-1)	k-factor (NLO/LO)
$Z \to \nu\nu + 3\ jets$	Own samples (AH)	1.66×10^3	1.13
$Z/\gamma* \to ee + 2\ jets$	atop4z, atop76,atop71 (AH)	1.16×10^4	1.18
$Z/\gamma* \to \mu\mu + 2\ jets$	atop67, atop86, atop72 (AH)	7.76×10^3	1.18
$Z/\gamma* \to \tau\tau + 2\ jets$	atopxb, atop96, atop93 (AH)	7.93×10^3	1.18
$W \to e\nu + 3\ jets$	atop6a (AH)	2.62×10^3	1.09
$W \to \mu\nu + 3\ jets$	atopeb (AH)	3.21×10^3	1.09
$W \to \tau\nu + 2\ jets$	atop8t (AH)	7.61×10^2	1.09
$t\bar{t}$ (all decays)	ttop0z (H)	3.45×10^4	NLO theory σ
WW (all decays)	Own samples (P)	4.17×10^3	1.41
QCD $60 < \hat{p}_T < 90$ GeV	jqcdgg + own samples(*) (P)	4.36×10^1	from data
QCD $90 < \hat{p}_T < 120$ GeV	jqcdhg + own samples(*) (P)	7.64×10^2	from data
QCD $120 < \hat{p}_T < 150$ GeV	jqcdig + own samples(*) (P)	9.58×10^2	from data
QCD $150 < \hat{p}_T < 200$ GeV	jqcdjg (P)	1.54×10^3	from data
QCD $200 < \hat{p}_T < 300$ GeV	jqcdkg (P)	7.03×10^3	from data
QCD $300 < \hat{p}_T < 400$ GeV	jqcdlg (P)	1.65×10^5	from data
QCD $400 < \hat{p}_T < 500$ GeV	jqcdmg (P)	3.07×10^6	from data
QCD $\hat{p}_T > 500$ GeV	jqcdng (P)	5.76×10^7	from data

Table 2: List of SM background processes considered for this analysis. The second column show the name of the dataset used and the MC Generator in parenthesis: (AH) ALPGEN+HERWIG; (H) HERWIG; (P) PYTHIA. The samples with (*) have a cut on $\not\!\!E_T > 25$ GeV.

scale in MCFM was set to $\mu = M_W$ in the case of W processes and $\mu = M_Z$ in the case of Z processes. To normalize the $t\bar{t}$ production, the NLO theoretical cross section was used [10]. Dedicated studies were carried out to determine the normalization of the QCD samples from the data. We compared the QCD multijet Monte Carlo to the JET20 trigger data sample. The ratio data/MC indicates that no k-factor different than 1.0 is necessary. We cross checked our findings in four different regions in $\not\!\!E_T$ and $E_T^{jet1} + E_T^{jet2} + \not\!\!E_T$, and we found again no indication that a different k-factor is needed. A complete description of the procedure is in note [4]. Here, the final results are presented. Figure 5 shows the comparison of the $\not\!\!E_T$ distribution between PYTHIA and the data, and figure 6 shows the data/MC ratio.

3.2.1 $\hat{p}_T$ Study

In the case of QCD multijet background, it is important to determine the minimum $\hat{p}_T$ that contributes to the $\not{E}_T$ trigger data, since it is virtually impossible to generate sufficient Monte Carlo statistics for an arbitrarily low $\hat{p}_T$ threshold. Events are required to pass all of the pre-selection cuts described in section 2.2. At this point the data sample is completely dominated by the QCD multijet background.

Figure 7 shows Monte Carlo distributions of H_T, defined as $H_T = E_T^{jet1} + E_T^{jet2} + E_T^{jet3}$, for different $\hat{p}_T$ cuts: 60, 70, 80, 90, 95, 100, 110, 120, and 130 GeV, compared to the data. Figure 9 shows similar plots for E_T^{jet2}. The ratios data/MC are shown in figures 8 and 10, respectively. From these plots one can see that the data favors a minimum $\hat{p}_T$ cut.

We thus perform a χ^2 fit comparing the nine H_T distributions to the data. The results are shown in figure 11. A similar study is done for the E_T of the second leading jet distributions, see figure 12. Both fits suggest that the data is "best" reproduced with a $\hat{p}_T$ around 95-100 GeV. Therefore, only QCD samples with $\hat{p}_T \gtrsim 90$ GeV are considered in the analysis. As already mentioned, a significant effort was made to generate multijet QCD samples with an integrated luminosity significantly larger than the data.

4 Additional Background Rejection

In addition to the pre-selection criteria described in section 2, a number of selection cuts are applied to significantly reduce the different SM backgrounds.

4.1 Multijets Background (QCD)

The production of multiple jet events coming from QCD processes has a huge cross section. A priori, these events should not be characterized for having much $\not{E}_T$. However, large missing energy may arise from the mismeasurement of the jet energy due to cracks and/or other detector effects. When a jet is partially reconstructed in the detector, it is expected that the azimuthal direction of the resulting $\not{E}_T$ will be aligned to the jet in the transverse plane. Figure 14 shows the azimuthal angle between the $\not{E}_T$ and each of the three leading jets. As expected, we observed a peak at $\Delta\phi = 0$. For comparison, figure 13 shows a similar plot for three representative mSUGRA signal points where no peak is observed. Therefore, to remove the contribution from multijet QCD background we require the azimuthal distance between $\not{E}_T$ and the direction of the three leading jets to be larger than the cone size of the jet.

$$\Delta\phi(\not{E}_T, \mathrm{jet}) > 0.7 \tag{9}$$

4.2 Electron Veto

W and Z bosons will decay into electrons a fraction of the time. These electrons can be misidentified as jets. To reject this contribution, we require that the electromagnetic fraction (EMF), defined as the ratio between the transverse electromagnetic energy of the jet to the total transverse energy of the jet, measured by the calorimeter, to be less than 0.9.

$$\mathrm{EMF}_{\mathrm{jets}} < 0.9 \tag{10}$$

Figure 15 shows the EMF distribution of the three leading jets for representative mSUGRA points. Similarly, figure 16 shows the EMF distribution for $W \to e\nu$. The peak at one is due to electrons. In the case of the mSUGRA samples, electrons comes from semileptonic decays in the development of the gluino and squark cascades.

4.3 Muon Veto

W and Z bosons can also decay into muons. These muons, if not detected, can produce large $\not\!\!E_{\mathrm{T}}$ in the event becoming a significant background in the analysis. Muons can be identified in the COT as isolated tracks. We define isolation for those tracks with $\mathrm{p_T} > 10$ GeV/c. A track is considered isolated if the scalar $\mathrm{p_T}$ sum of all additional tracks in a cone of radius, $\mathrm{R} = 0.4$, is less than 2 GeV/c, where only tracks as defined in section 2 are considered.

With the above definitions we implement two different cuts to reject these specific backgrounds:

- $Z/\gamma^* \to \mu\mu$: events are rejected if the invariant mass of the two highest isolated tracks falls in $76 < \mathrm{M_{inv}} < 106$ mass window. The invariant mass distribution for the mSUGRA points is shown on the left column of figure 17. As we can see, there are very few signal events which have two or more isolated tracks. Figure 18 show the distribution for $Z/\gamma^* \to \mu\mu$ and $W \to \mu\nu$ events. Most of the events from the first one are rejected by this cut.

- $W \to \mu\nu$: events are rejected if the azimuthal angle between the highest isolated track and the $\not\!\!E_{\mathrm{T}}$ is below 0.7. This cut is analogous to the cut for QCD rejection as it eliminates events where the $\not\!\!E_{\mathrm{T}}$ is caused by an undetected muon. Figure 19 show the azimuthal angle distribution between the $\not\!\!E_{\mathrm{T}}$ and isolated tracks for $Z/\gamma^* \to \mu\mu$ and $W \to \mu\nu$. Both distribution peak at zero due to events in which the $\not\!\!E_{\mathrm{T}}$ is aligned with an isolated track. The right column of figure 17 shows a similar distribution for the mSUGRA signal points. This cut removes a large fraction of the backgrounds while keeping most of the signal

5 Optimization

The previous cuts were introduced to reduce specific background processes. However, the background contribution can be further reduced using the fact that squarks and gluinos have large masses. We expect the mSUGRA signal events to be characterized by isotropic (spherical) final-state topologies with large amounts of transverse energy measured in the calorimeter. The variables that help to discriminate signal from background at this point are the following:

- $E_T^{\text{jet 1}}$: transverse energy of the leading jet.
- $E_T^{\text{jet 2}}$: transverse energy of the second leading jet.
- $E_T^{\text{jet 3}}$: transverse energy of the third leading jet.
- $\mathrm{H_T}$: total transverse energy defined as the sum of the transverse energies of the three leading jets ($H_T = \sum_{\text{jets}}^{3} E_T^{\text{jet}}$).
- $\not{E}_{\mathrm{T}}$: missing transverse energy corrected by the energy lost in the jets [11].

A careful MC study has been performed to set the optimal values for these variables and maximize their ability to separate the mSUGRA signal from the background. This ability is quantified by $\mathrm{S}/\sqrt{\mathrm{B}}$, where S denotes the expected number of signal events and $\sqrt{\mathrm{B}}$ is the statistical error on the Standard Model background. Due to the complexity of optimizing 103 points of signal with five variables that are correlated, a step-by-step procedure has been implemented:

- First, we reduced the number of points (see figure 2) in the study and we selected a set of points with similar squark mass and increasing gluino mass (row points 31-91), and a set of points with $\mathrm{M_{\tilde{q}}} \approx \mathrm{M_{\tilde{g}}}$ (diagonal points 23-91). We note that the difference between the points belonging to the same column, or same gluino mass, is small. At the bottom of a column, squarks and gluinos have similar masses, and therefore they tend to be produced with similar probability. As the mass of the squark increases (we move up the column), the squark cross section becomes smaller. Thus, at the top of the column most of the events tend to come from gluinos, whose mass has not changed.

  All optimization plots have been done with these limited set of mSUGRA points, with the aim to determine the different cuts defining the minimum number of zones into which the mSUGRA mass plane can be divided.

- Figure 20 and 21 show the $\mathrm{S}/\sqrt{\mathrm{B}}$ distributions for the points with $\mathrm{M_{\tilde{q}}} \approx \mathrm{M_{\tilde{g}}}$ (diagonal), and the points with similar squark masses (row). Each triangle in each of the plots corresponds to a different cut on $\mathrm{H_T}$. From these plots, we identify three different regions. In region A, we set the $\mathrm{H_T}$ cut to 255 GeV. Region B has a $\mathrm{H_T}$ cut of 330 GeV. Finally, region C has a cut of 355 GeV. All of these cuts are directly extracted from the maximum of the $\mathrm{S}/\sqrt{\mathrm{B}}$ distributions.

  Figures 22 and 23 show the $\mathrm{H_T}$ distributions for the points with $\mathrm{M_{\tilde{q}}} \approx \mathrm{M_{\tilde{g}}}$ (diagonal), and similar squark mass (row) respectively. When comparing the distributions from the histograms on those figures, we see that the difference is negligible between two points with similar gluino mass and different squark masses (points 23-31, 35-42, 46-52, etc).

- We now apply the $\mathrm{H_T}$ cut to the mSUGRA points and perform a similar study for the $\not{E}_{\mathrm{T}}$. Figures 24 and 25 show the $\mathrm{S}/\sqrt{\mathrm{B}}$ distribution for the points along the diagonal and the row. From these plots, we assign a $\not{E}_{\mathrm{T}}$ cut of 75 GeV for region A. The cuts for regions B and C are 100 GeV and 130 GeV, respectively. Figure 26 shows the $\not\!\!E_{\mathrm{T}}$ distribution for the points along the diagonal. Similarly, figure 27 shows the $\not\!\!E_{\mathrm{T}}$ distribution for the points along the row.

- After applying the $\mathrm{H_T}$ and $\not\!\!E_{\mathrm{T}}$ cuts, the $\mathrm{E_T}$ of the jets have less discriminating power. As an example, figure 28 shows the $\mathrm{S}/\sqrt{\mathrm{B}}$ distribution of the leading jet for points along the diagonal. The distribution is flat until it starts to drop, which implies that signal and background have the same shape. Therefore, the cut on this variables is chosen so that the signal acceptance remains high and the low-end tails of the jet's $\mathrm{E_T}$ distributions are removed. This can be seen in figures 29 through 31, where the arrows show the placement of the cut for the different regions. The only cut applied to the third jet transverse energy is the one from pre-selection (25 GeV).

We investigated the order in which the cuts are applied and chose the ordering which maximizes the $\mathrm{S}/\sqrt{\mathrm{B}}$. In conclusion, the entire generated mSUGRA plane is divided into three distinct regions as a function of the gluino mass, as seen in figure 2. Table 3 shows the value of the different thresholds which defined the three different signal regions. In table 4, the efficiencies for each of the cuts applied in the analysis (pre-selection and optimized cuts) are given for three representative mSUGRA points together with the number of expected events after all cuts. Only statistical uncertainties are considered at this point.

6 Signal Studies

In order to understand better the signal behavior with different gluino and squark masses, the variation of different quantities such as efficiencies, significances and relative contributions to the production subprocesses, were studied along columns (constant $M_{\tilde{g}}$), along rows (constant $M_{\tilde{q}}$) and along the diagonal ($M_{\tilde{g}} \approx M_{\tilde{q}}$) in the signal plane. The relative contributions for the different production subprocesses, gluino-gluino (gg), squark-gluino (sg) and squark-squark (or with anti-squarks) (ss) have been studied before any cut and after all the analysis cuts. The results and their interpretation follows:

- **Study along column s1 ($M_{\tilde{g}} \approx 185$ GeV/c^2)** In Figure 32 their relative contributions for the different production subprocesses is shown together with their efficiencies and significances. Before the cuts, the gg contribution is steadily increasing as long as the ss contribution is being suppressed due to the increasing squark mass. After the cuts, the gg contribution is slightly reduced. The most probable explanation for this effect is the fact that the jets coming from the gluino tend to be softer than a single jet produced from a squark of a similar mass. Therefore, it is the minimum threshold condition of the first and the second jet (in zone A: $E_T^{\mathrm{1stjet}} \geq 95$ GeV and $E_T^{\mathrm{2ndjet}} \geq 55$ GeV) which are reducing the gg contribution.

	$\not\!\!E_{\mathrm{T}}$ (GeV)	$\mathrm{H_T}$ (GeV)	$\mathrm{E_T^{jet\,1}}$ (GeV)	$\mathrm{E_T^{jet\,2}}$ (GeV)	$\mathrm{E_T^{jet\,3}}$ (GeV)
Region A	75	230	95	55	25
Region B	90	280	120	70	25
Region C	120	330	140	100	25

Table 3: Cut thresholds for the three different regions in which the signal plane is divided.

Cuts	mSUGRA s35	mSUGRA s56	mSUGRA s80
Initial Exp. # of Events	2149	561	83
Vertex: $\|V_z\| < 60$ cm	96.6 $\pm$ 0.2 %	96.7 $\pm$ 0.1 %	96.7 $\pm$ 0.1 %
$\geq$ 3 jets ($E_T > 25$ GeV and $\|\eta\| < 2.0$)	75.3 $\pm$ 0.4 %	75.3 $\pm$ 0.4 %	75.6 $\pm$ 0.4 %
1 Central jet ($\eta < 1.1$)	75.2 $\pm$ 0.4 %	74.9 $\pm$ 0.4 %	75.3$\pm$ 0.4 %
$\not\!\!E_{\mathrm{T}} > 70$ GeV	47.0 $\pm$ 0.4 %	55.0 $\pm$ 0.4 %	61.7 $\pm$ 0.4 %
EEMF > 0.15	47.0 $\pm$ 0.4 %	55.0 $\pm$ 0.4 %	61.7 $\pm$ 0.4 %
ECHF > 0.15	46.6 $\pm$ 0.4 %	54.7 $\pm$ 0.4 %	61.1 $\pm$ 0.4 %
$\Delta\phi$ ($\not\!\!E_{\mathrm{T}}$, jets)	24.7 $\pm$ 0.4 %	30.3 $\pm$ 0.4 %	34.4 $\pm$ 0.4 %
EMF of the jets	23.2 $\pm$ 0.3 %	28.3 $\pm$ 0.4 %	32.0 $\pm$ 0.4 %
Minv < 76 or Minv > 106 GeV/c^2	23.2 $\pm$ 0.3 %	28.3 $\pm$ 0.4 %	32.0 $\pm$ 0.4 %
$\Delta\phi$ ($\not\!\!E_{\mathrm{T}}$, max iso track)	22.5 $\pm$ 0.3 %	27.8 $\pm$ 0.4 %	31.3 $\pm$ 0.4 %
$\mathrm{E_T}$ of the jets	16.9 $\pm$ 0.3 %	17.3 $\pm$ 0.3 %	15.9 $\pm$ 0.3 %
$\not\!\!E_{\mathrm{T}}$	16.0 $\pm$ 0.3 %	14.7 $\pm$ 0.3 %	11.3 $\pm$ 0.3 %
$\mathrm{H_T}$	14.5 $\pm$ 0.2 %	12.8 $\pm$ 0.2 %	10.6 $\pm$ 0.2 %
$\mathrm{N_{exp}}$ Events (371 $\mathrm{pb}^{-}1$)	310.8 $\pm$ 3.8	71.6 $\pm$ 0.9	8.9 $\pm$ 0.1

Table 4: Efficiencies for mSUGRA events in regions A, B, and C. The points shown are representative for each region.

- **Study along diagonal s34** ($M_{\tilde{g}} \approx M_{\tilde{q}}$) Same quantities as in the previous case are shown in Figure 33, but now along the diagonal where the mass of the squark is comparable to the gluino mass. The two vertical lines separate the three optimized regions. As expected, the three different signal production processes keep their relative contribution along the diagonal, even after the analysis cuts. The efficiencies increase along the diagonal and the significances drop with increasing mass, as expected, but the different optimizations per each region helps on reducing the falling rates.

- **Study along row s6** ($M_{\tilde{q}} \approx 355$ GeV/c^2) Same quantities as in the previous case are shown in Figure 34. The drop at high gluino masses can be explained by the fact that it is a region where squark production dominates and topologies with only two jets in the final state are favored.

7 Systematic Uncertainties

A complete study of systematic uncertainties on the estimation of signal and background expected events has been carried out. The resulting quoted systematic uncertainties for signal and background are collected in Tables 5 to 8.

- **Energy scale**: $\pm 1\sigma$ variations in the jet energy corrections were considered to account for the uncertainty on the jet energy scale. The corresponding shift in the $\not\!\!E_{\mathrm{T}}$ was also included.

- **Luminosity**: We quote a 6% uncertainty on the total integrated luminosity [12].

- **ISR/FSR**: We followed the standard prescription, as determined for Top and Higgs analyses, to estimate the systematic uncertainty on the expected signal events related to the modeling of the initial and final state radiation in the Monte Carlo. For each point in the mSUGRA mass plane, additional samples were generated with modified Λ_{QCD} values (See CDF Joint Physics www page for details).

7.1 Renormalization Scale

- **PROSPINO Calculation**: The default value of the renormalization scale in PROSPINO is set as explained in section 3.1. To investigate the effects of the renormalization scale on the PROSPINO cross section we shift the value of μ to $\mu * 2$ and $\mu/2$. The systematic uncertainty associated with the renormalization scale is then given by half the difference of the cross sections obtained from the previous two scenarios. The uncertainty due to the renormalization scale on the signal cross section is shown in the figures 49 and 50. The first plot shows the evolution of the cross section values along two columns (points with constant gluino mass). Likewise, the second plot shows the cross section when

$M_{\tilde{q}} \approx M_{\tilde{g}}$ (diagonal). As we can see, this uncertainty is of the order of 20 %. Also shown in the plots is the combined uncertainty from the renormalization scale and PDF uncertainty (see below).

- **MCFM Calculation**: A similar strategy is used for the background processes whose NLO cross section is calculated using MCFM. However, for Z/W + jets we only use the uncertainty returned by setting the renormalization to $2 * \mu$. This is due to the fact that for $\mu/2$ the renormalization scale is in a region where the NLO cross section calculation is unstable [13].

- **QCD Multijet Background**: The uncertainty on the multijet background due to the renormalization scale is 10 %, taken from [14].

7.2 PDF uncertainty

- **Top Production**: The top PDF uncertainty is taken directly from the theoretical calculation by Cacciari *et al.* [10]. For this analysis we have assumed a top mass of 175 GeV.

- **PROSPINO and MCFM Calculations**: We apply the Hessian method [15] to calculate the uncertainty due to the choose of the PDF. In our case this corresponds to PDFs CTEQ6L1 (LO) and CTEQ6.1M (NLO). We run PROSPINO and MCFM using each of the 40 PDFs and we compute the uncertainty associated with the PDF uncertainty following the next recipe:

  - For each eigenvalue we check to see if the +1 σ and -1 σ PDFs have produced a positive and negative shift respectively. If that is the case then the positive and negative systematic uncertainties are given by the following formula: $\mathrm{d}X_{\pm}^2 = \sum_i^{20}(X_{\pm}^i - X_{\mathrm{CTEQ6.1M}})^2$. Here, X, is the quantity you are interested in.
  - If the +1 σ and -1 σ PDFs for a given eigenvalue result on just a positive shift with respect to the nominal value, only the largest uncertainty contributes to $\mathrm{d}X_+$. There is no contribution to $\mathrm{d}X_-$ from this eigenvalue.
  - If the +1 σ and -1 σ PDFs for a given eigenvalue result on just a negative shift with respect to the nominal value, only the largest uncertainty contributes to $\mathrm{d}X_-$. There is no contribution to $\mathrm{d}X_+$ from this eigenvalue.

In the case of the signal, the uncertainty on the PDF produces dramatic consequences as we can see in figures 35 through 37. The plots shown correspond to the cross section [5] for each of the PROSPINO subprocesses for mSUGRA point 23, 56, and 80 respectively. As we can see, the largest source of uncertainty in the plots comes from eigenvalue 15, which is associated with the high-x gluon content in the PDF. The overall effect of the PDF uncertainty on the signal

[5] We remind the reader that these cross sections are very small, and any increase still results on a very small cross section

cross section is about 30 % (figures 49 and 50). However, the uncertainty introduced by the PDFs on the signal cross section does not translate into a large effect on the signal efficiency (see table 5). Figures 38 through 40 show the distribution of the cross section for W + 2 jets, Z + 2 jets, and WW respectively. Here, the uncertainty on the PDF has little effect on the calculation of the k-factor (σ_{NLO}/σ_{LO}). It makes sense since the above background processes are dominated by contributions with $q\bar{q}$ in the initial state.

- **QCD Multijet Background**: We quote a 20% uncertainty on the QCD mutijet background due to PDF following studies on inclusive jet production at CDF [14].

In Figure 41 the different contributions of the systematic uncertainties to the signal efficiency are shown for the three representative points close to the diagonal (mSUGRA s35, mSUGRA s56 and mSUGRA s80). The most important contribution is the Jet Energy Scale, followed by ISR/FSR and the PDF uncertainties.

Region	Samples	JES	$\mathcal{L}$	Renorm.	PDF	ISR/FSR	**Total**
A	mSUGRA s35	± 1.05 %	± 0.87 %	± 0.02 %	± 0.24 %	± 0.70 %	**± 1.55 %**
	(w.r.t nominal eff.)	7.2%	6.0%	0.1%	1.7%	4.8%	10.7%
B	mSUGRA s56	± 1.04 %	± 0.77 %	± 0.02 %	± 0.34 %	± 0.67 %	**± 1.50 %**
	(w.r.t nominal eff.)	8.1%	6.0%	0.2%	2.7%	5.2%	11.7%
C	mSUGRA s80	± 1.12 %	± 0.64 %	± 0.02 %	± 0.47 %	± 0.42 %	**± 1.43 %**
	(w.r.t nominal eff.)	10.6 %	6.0%	0.2%	4.4%	4.0%	13.5%

Table 5: Systematic uncertainties on the selection efficiency for some representative mSUGRA signal points. The upper numbers are the different uncertainties on the efficiencies and the lower numbers the uncertainties relative to the nominal efficiencies, quoted in Table 4.

8 Observed Data Events and Expected Background

In this section the number of observed events, and expected background are presented for a total luminosity of 371 pb^{-1}. Table 9 gives the number of data events observed in each region defined in the analysis. Table 10 shows the total number of background expected events for each of the regions. A breakdown of the different backgrounds in each of the regions is included in tables 11, through 13. Figures 42 show the different relative contributions to the overall background after all the cuts have been applied. Figures 43 through 48 show the H_T and $\not{E}_T$ distributions for the final results. In these plots, all cuts have been applied except the one on the variable that is represented. The arrows in the figures indicate the position where the cuts on this variable will

Region	JES	$\mathcal{L}$	Renorm.	PDF	**Total**
Region A	$\pm$ 30.66	$\pm$ 12.66	$\pm$ 15.48	$\pm$ 23.78	$\pm$ **44.03**
(w.r.t. Exp. Bkg.)	14%	6%	7%	11%	21%
Region B	$\pm$ 11.91	$\pm$ 3.34	$\pm$ 4.02	$\pm$ 5.66	$\pm$ **14.26**
(w.r.t. Exp. Bkg.)	21%	6%	7%	10%	26%
Region C	$\pm$ 2.33	$\pm$ 0.49	$\pm$ 0.57	$\pm$ 0.85	$\pm$ **2.60**
(w.r.t. Exp. Bkg.)	28%	6%	7%	10%	32%

Table 6: Systematic uncertainties on the background expected number of events (in number of events and with respect to the total background expectations, quoted in Table 10) for the different regions considered in the analysis.

be placed. Each figure shows the data together with the Monte Carlo predictions for the SM background and a representative mSUGRA signal mass point from the correspondent optimized region. The background Monte Carlo predictions provide a reasonable description of the data in all regions and no excess with respect to the SM predictions is observed [6].

9 Exclusion limits

Since no excess with respect to the Standard Model predictions is observed in the data, as can be seen from tables 9 and 10, as well as from figures 43 through 48, we proceed to stablish exclusion limits on gluino and squark production. Applying a Bayesian technique we can exclude a range of squark and gluino masses and production cross-sections to a 95 % confidence level (C.L). The Poisson probability of obtaining the observed result is:

$$\frac{e^{-(s\epsilon+b)}(s\epsilon+b)^n}{n!}\,, \tag{11}$$

where n is the number of observed events, s is the cross section for our mSUGRA samples, b is the number of expected background and ϵ is the product of the acceptance times luminosity, and has units of inverse cross section.

In the Bayesian approach, a prior function need to be defined. Assuming a flat function $\pi(s) = 1$ for $s \geq 0$ and $\pi(s) = 0$ for $s < 0$, the upper limit s_u at confidence level β is computed, in a finite Bayesian prior-ensemble approximation by solving:

$$I(s_u) = (1-\beta)I(0)\,, \tag{12}$$

where $I(s_0)$ is the integral:

[6]See the same distributions but with the total background systematic uncertainties in Figure 69. See also Appendix C for more comprehensive data vs MC comparisons.

Background	Region A	Region B	Region C
QCD	$\pm$ 7.11	$\pm$ 1.48	$\pm$ 0.22
WW	$\pm$ 0.07	$\pm$ 0.02	$\pm$ 0.00
$W \to e\nu$	$\pm$ 1.93	$\pm$ 0.53	$\pm$ 0.10
$W \to \mu\nu$	$\pm$ 0.07	$\pm$ 0.48	$\pm$ 0.12
$W \to \tau\nu$	$\pm$ 1.93	$\pm$ 0.60	$\pm$ 0.04
$Z/\gamma^* \to ee$	$\pm$ 0.07	$\pm$ 0.00	$\pm$ 0.00
$Z/\gamma^* \to \mu\mu$	$\pm$ 1.93	$\pm$ 0.02	$\pm$ 0.01
$Z/\gamma^* \to \tau\tau$	$\pm$ 0.07	$\pm$ 0.03	$\pm$ 0.00
$Z \to \nu\nu$	$\pm$ 1.93	$\pm$ 0.85	$\pm$ 0.07

Table 7: Systematic uncertainty on the background expected number of events due to the uncertainty on the renormalization scale.

$$I(0) = \frac{1}{M}\sum_{i=1}^{M}\left[\int_{s_0}^{\infty}\frac{e^{-(s\epsilon+b)}(s\epsilon+b)^n}{n!}ds\right] , \tag{13}$$

with M being the number of random pairs of ϵ and b events in this finite approach.

This procedure and the program that implements it is described thoroughly in the note [16]. This program allows to use correlated and uncorrelated uncertainties into the limit calculation process as well as choose from different random generators. Due to the fact that our theoretical uncertainties on the cross-section can be close to 30% as shown in Table 5 , we choose a gamma function as a random generator in order to avoid non-converging integrals. The statistical and the ISR/FSR uncertainties are considered uncorrelated. The rest of the systematics (renormalization scale, PDF, jet energy scale and luminosity) are considered correlated. The PDF and renormalization scale uncertainties that affect the signal cross-section are properly translated into signal acceptance uncertainties and introduced into the limit calculation. All systematic contributions are quoted as 1 sigma uncertainties except for the PDF which corresponds to 1.64 sigmas [17].

We use a poissonian fluctuation to calculate the expected cross section using the following formula:

$$\sigma_{exp} = \sum P(n^i_{obs}|n_{exp}) * \sigma^i_{obs} , \tag{14}$$

where σ_{obs} is the cross section upper limit with the number of observed events, n_{obs}, $P(n^i_{obs}|n_{exp})$ is the poisson probability of observing n_{obs} events when the mean value is the number of expected background events, n_{exp}, and the sum is over all the possible values that give a significant contribution to this poisson fluctuation. In any case, for numbers larger or similar to 10, it is a good approximation to avoid the poissonian fluctuation and use $n_{obs} = n_{exp}$, instead.

Background	Region A	Region B	Region C
QCD	$\pm$ 14.2	$\pm$ 2.97	$\pm$ 0.45
$t\bar{t}$	$\pm$ 5.78	$\pm$ 1.55	$\pm$ 0.25
WW	$\pm$ 0.07	$\pm$ 0.02	$\pm$ 0.00
$W \rightarrow e\nu$	$\pm$ 0.86	$\pm$ 0.24	$\pm$ 0.05
$W \rightarrow \mu\nu$	$\pm$ 0.75	$\pm$ 0.21	$\pm$ 0.05
$W \rightarrow \tau\nu$	$\pm$ 0.78	$\pm$ 0.27	$\pm$ 0.02
$Z/\gamma^* \rightarrow ee$	$\pm$ 0.00	$\pm$ 0.00	$\pm$ 0.00
$Z/\gamma^* \rightarrow \mu\mu$	$\pm$ 0.02	$\pm$ 0.01	$\pm$ 0.00
$Z/\gamma^* \rightarrow \tau\tau$	$\pm$ 0.04	$\pm$ 0.01	$\pm$ 0.00
$Z \rightarrow \nu\nu$	$\pm$ 1.23	$\pm$ 0.39	$\pm$ 0.03

Table 8: Systematic uncertainty on the background expected number of events due to the uncertainty on the PDFs.

Since we have three set of cuts, three different expected limits can be stablished per each point. We associate to each point a single set of cuts which is the one that gives the highest expected limits. Then, the observed limits are calculated with this criteria.

We generate 1.5 million (ϵ, b) pairs of random events to evaluate the integrals and estimate the maximum cross section for each of the points in the mSUGRA plane. The cross sections results are shown in Figures 49 and 50. Since the theoretical uncertainties are properly taken into account inside the limit calculation, the crossing between the 95% C.L. cross section with the nominal cross section gives an upper estimation for the squarks/gluino masses along the first column of points generated ($M_{\tilde{g}} \sim 185$ GeV/c^2) or along the diagonal $M_{\tilde{q}} \sim M_{\tilde{g}}$, respectively.

After this procedure, we have a set of points that are either excluded or not. In order to determine the excluded region independently from our generation set, as shown in Figure 51, a smooth line is linearly interpolated between any pair of points on the boundary regions. For each of these points, the ratio $r = \sigma_{95}/\sigma$ has been computed so that excluded points have $r < 1$ and not excluded points $r > 1$, being $r^* \equiv r = 1$ the point that lies on the exclusion line. Then, between every pair of excluded (E) and not excluded (NE) points, the corresponding squark/gluino masses of the intermediate point (m^*) are extracted by solving equations of type:

$$r^* = r_E + \frac{r_{NE} - r_E}{m_{NE} - m_E} \cdot (m^* - m_E) = 1\,, \tag{15}$$

where m_E and m_{NE} are the masses of the excluded and not excluded points, respectively.

In Figure 51 the previous exclusion regions determined by other experiments are also presented. Since we observe less events than expected, the observed excluded

Cuts	Bkg. Region A	Bkg. Region B	Bkg. Region C
GoodRun List	9.93×10^6		
Trigger (MET35 + 2 jets)	3.10×10^6		
Vertex: $\|V_z\| < 60$ cm	2.32×10^6		
≥ 3 jets ($E_T > 25$ GeV and $\eta < 2.0$)	356713		
1 Central jet ($\eta < 1.1$)	345771		
$\not{E}_{\mathrm{T}} > 70$ GeV	15414		
EEMF > 0.15	14090		
ECHF > 0.15	13127		
$\Delta\phi$ ($\not{E}_{\mathrm{T}}$, jets)	2301		
EMF of the jets	1425		
Minv < 76 or Minv > 106 GeV/c^2	1410		
$\Delta\phi$ ($\not{E}_{\mathrm{T}}$, max iso track)	1204		
$\mathrm{E_T}$ of the jets	296	141	39
$\not{E}_{\mathrm{T}}$	250	62	4
$\mathrm{H_T}$	185 ± 14	40 ± 6	$2^{+2.6}_{-1.3}$

Table 9: Observed number of data events for regions A, B, and C. The optimization procedure for the final three cuts is explained in the previous section. These numbers are to be compared with the ones given in table 10.

area is bigger than the expected one. Topologies involving three jets in the final state are specially important close to the diagonal, where the production of one squark and one gluino dominates, and it is where we reach higher excluded masses with our 3-jets analysis. The drop below the diagonal is mainly due to the fact that squark pair-production dominates and hence, two jets in the final state dominate this portion of the plane. The region of low gluino masses and high squark masses is very sensitive to the systematic effects provided that the crossing between the observed/expected lines with the nominal cross-sections is very shallow, as it can be seen in Figure 49.

In the region where $M_{\tilde{g}} \approx M_{\tilde{q}}$, we exclude masses up to 380 GeV/c^2 at 95% C.L. In any case, we found that $M_{\tilde{g}} > 220$ GeV/c^2. The most energetic event found after all the cuts have been applied is shown in Figure 52.

References

[1] J. Wess and B. Zumino *Nucl. Phys* **B70** (1974); see also: D. V. Volkov and V. P. Akulov, *Phys. Lett* **B46** (1973) 109.

[2] J. R. Ellis, S. Kelley, and D. V. Nanopolous *Phys. Lett.* **B260**, 131 (1991).

Cuts	Bkg. Region A	Bkg. Region B	Bkg. Region C
Initial Exp. # of Events	9.83×10^6		
Vertex: $\lvert V_z \rvert < 60$ cm	$(2.878 \pm 0.001) \times 10^6$		
≥ 3 jets ($E_T > 25$ GeV and $\eta < 2.0$)	$(8.898 \pm 0.007) \times 10^5$		
1 Central jet ($\eta < 1.1$)	$(8.707 \pm 0.007) \times 10^5$		
$\not\!\!E_{\mathrm{T}} > 70$ GeV	12645 ± 61		
EEMF > 0.15	12642 ± 61		
ECHF > 0.15	12518 ± 60		
$\Delta\phi$ ($\not\!\!E_{\mathrm{T}}$, jets)	2527.8 ± 22.6		
EMF of the jets	1606.4 ± 19.1		
Minv < 76 or Minv > 106 GeV/c^2	1587.5 ± 19.1		
$\Delta\phi$ ($\not\!\!E_{\mathrm{T}}$, max iso track)	1291.2 ± 18.0		
$\mathrm{E_T}$ of the jets	325.3 ± 8.6	145.0 ± 5.6	58.1 ± 3.5
$\not\!\!E_{\mathrm{T}}$	276.8 ± 7.9	76.3 ± 3.9	11.0 ± 1.4
$\mathrm{H_T}$	211.0 ± 6.9	55.7 ± 3.4	8.2 ± 1.2
Total Expected with Systematics	**$211.0 \pm 6.9 \pm 44.0$**	**$55.7 \pm 3.4 \pm 14.3$**	**$8.2 \pm 1.2 \pm 2.6$**

Table 10: Expected number of background events for regions A, B, and C. Recall that the last three cuts are optimized differently for each of the regions.

[3] A.H. Chamseddine, R. Arnowitt, and P. Nath *Phys. Rev. Lett.* **49** (1982) 970. R. Barbieri, S. Ferrara, and C. A. Savoy *Phys. Lett.* **B119** (1982) 343. L.J. Hall, J. Lykken, and S. Weinberg *Phys. Rev.* **D27** (1983) 2359. For a review, see H.P. Nilles *Phys. Rep.* **110** (1984) 1.

[4] X. Portell, M. Martínez, C. Sánchez, CDF Note 7561.

[5] T. Affolder *et al.*, The CDF Collaboration, Phys. Rev. Lett. 88, 041801 (2002).

[6] H. Baer, F.E. Paige, S.D. Protopopescu, and X. Tata, *ISAJET 7.48: A Monte Carlo Event Generator for pp, $p\bar{p}$, and e^+e^- Reactions*, hep-ph/0001086.

[7] T. Sjöstrand *et al. Computer Phys. Commun.* 135 (2001)

[8] W. Beenakker, R. Höpker, and M. Spira, *PROSPINO: A Program for the Production of Supersymmetric Particles in Next-To-Leading Order QCD.*

[9] J, Campbell, and R. K. Ellis, *MCFM: A Monte Carlo for FeMtobarn processes at Hadron Colliders.*

[10] M. Cacciari, S. Frixione, M. L. Mangano, P. Nason, and G. Ridolfi, hep/ph-0303085.

[11] CDF Collaboration, F. Abe *et al.*, Phys. Rev. **D45**, 1448 (1992).

[12] S. Klimenko *et al.*, FERMILAB-FN-0741 (2003); D. Acosta *et al.*, Nucl. Instrum. Meth. **A494**, 57 (2002).

[13] J. Campbell, and R. K. Ellis *Phys. Rev.* **D64** (2002), hep-ph/0202176.

[14] R. Lefèvre, M. Martínez, and O. Norniella, CDF Note 7576.

[15] D. Sutmp, J. Huston, J. Pumplin, and W. Tung, hep-ph/0303013. A.D. Martin, R. G. Roberts, W. J. Stirling, and R.S. Thorne, hep/ph-0211080. J. Pumplin, D. Stump, R. Brock, D. Casey, and J. Huston, hep-ph/0101032.

[16] Joel Heinrich, CDF Note 7587.

[17] J. Pumplin, D.R. Stump, J. Huston, H.L. Lai, P. Nadolsky, W.K. Tung, hep-ph/0201195; JHEP 0207 (2002) 012.

[18] UA1 Collaboration, C. Albajar *et al.*, Phys. Lett. **B198** (1987) 261.

[19] UA2 Collaboration, S. Albachi *et al.*, Phys. Lett. **B235** (1990) 363.

[20] DØ Collaboration, B. Abbott *et al.*, Phys. Rev. Lett. **83** (1999) 4937. CDF Collaboration, T. Affolder *et al.*, Phys. Rev. Lett. **88** (2002) 041801.

[21] DØ Collaboration, P. Verdier, DØ Note 4737-CONF.

[22] The LEP-SUSY working group: *http://lepsusy.web.cern.ch/lepsusy/*

[23] C. Rott, CDF Note 7526.

[24] V. Veszpremi, D. Bortoletto, A. Garfinkel, O. González, C. Rott, CDF Note 7719.

Cuts	$W \rightarrow e\nu + 3\ jets$	$W \rightarrow \mu\nu + 3\ jets$	$W \rightarrow \tau\nu + 2\ jets$
Initial Exp. # of Events	36214	36214	99710
Vertex: $\|V_z\| < 60$ cm	34910 ± 13.1	34898 ± 12.6	96154 ± 40.9
≥ 3 jets ($E_T > 25$ GeV and $\eta < 2.0$)	6974 ± 27.7	1840 ± 14.7	4783 ± 47.1
1 Central jet ($\eta < 1.1$)	6758 ± 27.4	1784 ± 14.5	4632 ± 46.4
$\not\!\!E_{\mathrm{T}} > 70$ GeV	1041 ± 11.7	505 ± 7.9	585 ± 16.8
EEMF > 0.15	1041 ± 11.7	505 ± 7.9	585 ± 16.8
ECHF > 0.15	1027 ± 11.7	501 ± 7.8	575 ± 16.7
$\Delta\phi$ ($\not\!\!E_{\mathrm{T}}$, jets)	820 ± 10.5	387 ± 6.9	375 ± 13.5
EMF of the jets	191 ± 5.1	346 ± 6.5	295 ± 12.0
Minv < 76 or Minv > 106 GeV/c^2	191 ± 5.1	345 ± 6.5	295 ± 12.0
$\Delta\phi$ ($\not\!\!E_{\mathrm{T}}$, max iso track)	182 ± 5.0	190 ± 4.8	272 ± 11.5
Region A			
$\mathrm{E_T^{jets}} > 95$, 55, and 25 GeV	36.2 ± 2.2	33.2 ± 2.0	36.6 ± 4.2
$\not\!\!E_{\mathrm{T}} > 75$ GeV	31.5 ± 2.1	29.8 ± 1.9	31.2 ± 3.9
$\mathrm{H_T} > 230$ GeV	23.3 ± 1.8	20.5 ± 1.6	21.5 ± 3.2
Region B			
$\mathrm{E_T^{jets}} > 120$, 70, and 25 GeV	17.3 ± 1.5	13.4 ± 1.3	14.1 ± 2.6
$\not\!\!E_{\mathrm{T}} > 90$ GeV	8.9 ± 1.1	9.0 ± 1.1	7.8 ± 2.0
$\mathrm{H_T} > 280$ GeV	6.4 ± 0.9	5.8 ± 0.9	7.3 ± 1.9
Region C			
$\mathrm{E_T^{jets}} > 140$, 100, and 25 GeV	8.3 ± 1.1	4.5 ± 0.7	4.9 ± 1.5
$\not\!\!E_{\mathrm{T}} > 120$ GeV	1.5 ± 0.5	2.2 ± 0.5	1.0 ± 0.7
$\mathrm{H_T} > 330$ GeV	1.2 ± 0.4	1.5 ± 0.4	0.5 ± 0.5

Table 11: Expected number of background events from Standard Model W production processes. Only statistical uncertainties are shown.

Cuts	$Z \to \nu\nu + 3\ jets$	$Z/\gamma^* \to ee + 2\ jets$	$Z/\gamma^* \to \mu\mu + 2\ jets$	$Z/\gamma^* \to \tau\tau + 2\ jets$
Initial Exp. # of Events	21800	32441	32441	32441
Vertex: $\lvert V_z \rvert < 60$ cm	21080 ± 12.0	31276 ± 8.4	31282 ± 8.7	31287 ± 8.3
3 jets	1039 ± 14.9	4243 ± 11.5	424 ± 5.1	1887 ± 8.8
1 Central jet ($\eta < 1.1$)	1004 ± 14.6	4081 ± 11.3	408 ± 5.0	1816 ± 8.6
$\not{E}_T > 70$ GeV	320 ± 8.4	31 ± 0.9	65 ± 1.7	67 ± 1.6
EEMF > 0.15	320 ± 8.4	31 ± 0.9	65 ± 1.7	67 ± 1.6
ECHF > 0.15	317 ± 8.3	30 ± 0.9	64 ± 1.7	66 ± 1.6
$\Delta\phi$ ($\not{E}_T$, jets)	240 ± 7.3	7.4 ± 0.4	48 ± 1.5	29 ± 1.0
EMF of the jets	214 ± 6.9	1.1 ± 0.2	43 ± 1.4	22 ± 0.9
M_{inv} window	214 ± 6.9	0.9 ± 0.2	27 ± 1.2	22 ± 0.9
$\Delta\phi$ ($\not{E}_T$, max iso track)	214 ± 6.9	0.2 ± 0.1	9.2 ± 0.7	11 ± 0.7
Region A				
$E_T^{jets} > 95$, 55, and 25 GeV	43.5 ± 3.11	0.03 ± 0.10	1.5 ± 0.30	2.4 ± 0.31
$\not{E}_T > 75$ GeV	38.8 ± 2.94	0.02 ± 0.10	1.3 ± 0.28	1.8 ± 0.26
$H_T > 230$ GeV	27.9 ± 2.49	0.02 ± 0.10	0.51 ± 0.15	1.4 ± 0.23
Region B				
$E_T^{jets} > 120$, 70, and 25 GeV	19.4 ± 2.08	0.00 ± 0.10	0.36 ± 0.14	1.1 ± 0.21
$\not{E}_T > 90$ GeV	14.1 ± 1.77	0.00 ± 0.10	0.22 ± 0.13	0.47 ± 0.13
$H_T > 280$ GeV	8.7 ± 1.39	0.00 ± 0.10	0.22 ± 0.13	0.29 ± 0.11
Region C				
$E_T^{jets} > 140$, 100, and 25 GeV	4.5 ± 1.00	0.00 ± 0.10	0.11 ± 0.11	0.39 ± 0.13
$\not{E}_T > 120$ GeV	1.3 ± 0.55	0.00 ± 0.10	0.07 ± 0.11	0.01 ± 0.09
H_T 330 GeV	0.67 ± 0.39	0.00 ± 0.10	0.07 ± 0.11	0.00 ± 0.09

Table 12: Expected number of background events from Standard Model Z production processes. Only statistical uncertainties are shown.

Cuts	$t\bar{t}$	WW	QCD
Initial Exp. # of Events	2484	4653	9.53×10^6
Vertex: $\lvert V_z\rvert < 60$ cm	2390 ± 1.0	4509 ± 3.5	$2.59\times10^6 \pm 1364$
≥ 3 jets ($E_T > 25$ GeV and $\eta < 2.0$)	2130 ± 1.8	1765 ± 9.9	864755 ± 661
1 Central jet ($\eta < 1.1$)	2119 ± 1.8	1709 ± 9.8	846405 ± 652
$\not\!\!E_{\mathrm{T}} > 70$ GeV	429 ± 2.0	86 ± 2.7	9517 ± 55.8
EEMF > 0.15	429 ± 2.0	86 ± 2.7	9514 ± 55.8
ECHF > 0.15	427 ± 1.9	85 ± 2.7	9425 ± 55.6
$\Delta\phi$ ($\not\!\!E_{\mathrm{T}}$, jets)	295 ± 1.7	64 ± 2.4	261 ± 10.2
EMF of the jets	222 ± 1.5	29 ± 1.6	242 ± 9.8
Minv < 76 or Minv > 106 GeV/c^2	221 ± 1.5	29 ± 1.6	242 ± 9.8
$\Delta\phi$ ($\not\!\!E_{\mathrm{T}}$, max iso track)	156 ± 1.3	23 ± 1.4	234 ± 9.7
Region A			
$\mathrm{E_T^{jets}} > 95$, 55, and 25 GeV	63.3 ± 0.8	3.2 ± 0.5	105.3 ± 6.0
$\not\!\!E_{\mathrm{T}} > 75$ GeV	56.2 ± 0.8	2.9 ± 0.5	83.1 ± 5.4
$\mathrm{H_T} > 230$ GeV	43.0 ± 0.7	1.7 ± 0.4	71.1 ± 4.9
Region B			
$\mathrm{E_T^{jets}} > 120$, 70, and 25 GeV	25.5 ± 0.5	1.1 ± 0.3	52.7 ± 4.0
$\not\!\!E_{\mathrm{T}} > 90$ GeV	15.9 ± 0.4	0.7 ± 0.3	19.4 ± 2.4
$\mathrm{H_T} > 280$ GeV	11.5 ± 0.4	0.5 ± 0.2	14.8 ± 2.0
Region C			
$\mathrm{E_T^{jets}} > 140$, 100, and 25 GeV	8.8 ± 0.3	0.27 ± 0.15	26.4 ± 2.6
$\not\!\!E_{\mathrm{T}} > 120$ GeV	2.3 ± 0.2	0.09 ± 0.09	2.5 ± 0.9
$\mathrm{H_T} > 330$ GeV	1.9 ± 0.1	0.09 ± 0.09	2.2 ± 0.8

Table 13: Expected number of background events for $t\bar{t}$, WW and QCD multijet processes. Only statistical uncertainties are shown.

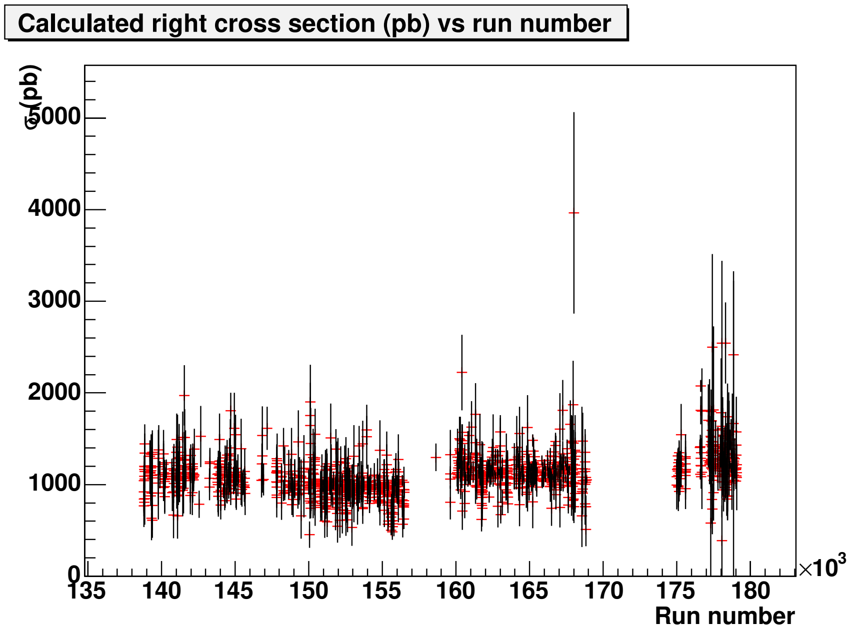

Figure 1: Cross section vs run number of the MET35 trigger. The plot includes a number of clean up cuts: GoodRun List v7 (0,0,0,0), $|V_z| < 60$ cm, raw $\not{E}_{\mathrm{T}} > 35$ GeV and 3 jets with raw $E_{\mathrm{T}}^{\mathrm{jet}} > 15$ GeV and $|\eta^{\mathrm{jet}}| < 2.3$.

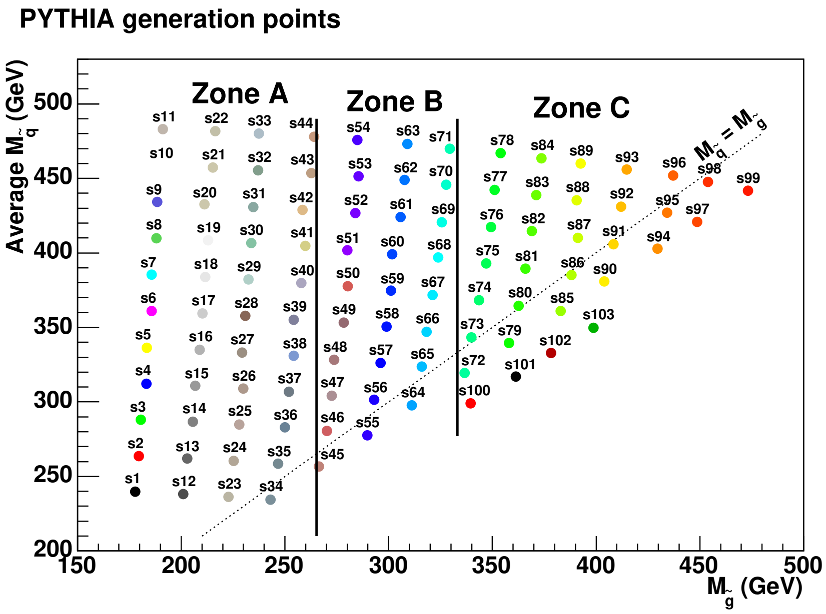

Figure 2: mSUGRA points generated with PYTHIA. The y-axis is the average mass of the 8 squarks of the first two generations. The x-axis corresponds to the mass of the gluino. 15,000 events were generated for each point. The plot is divided into the three zones obtained from the optimization study.

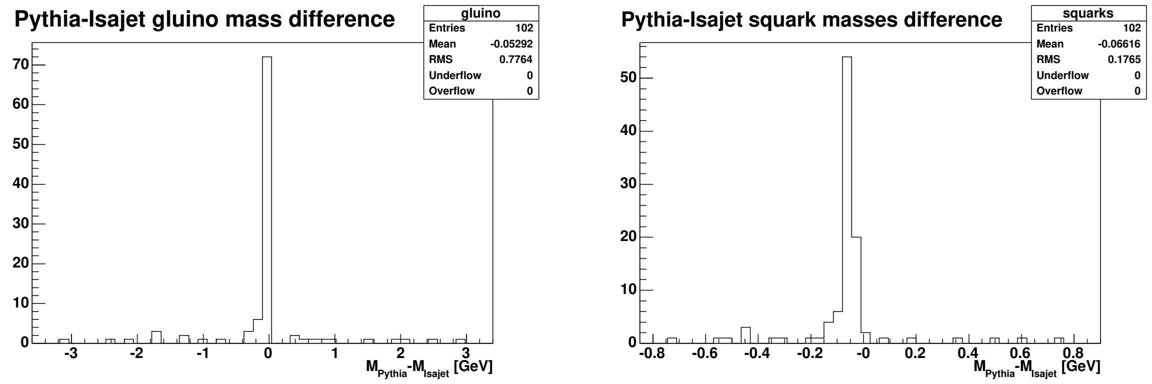

Figure 3: Mass differences between Pythia and Isajet for gluino (left) and squarks (right)

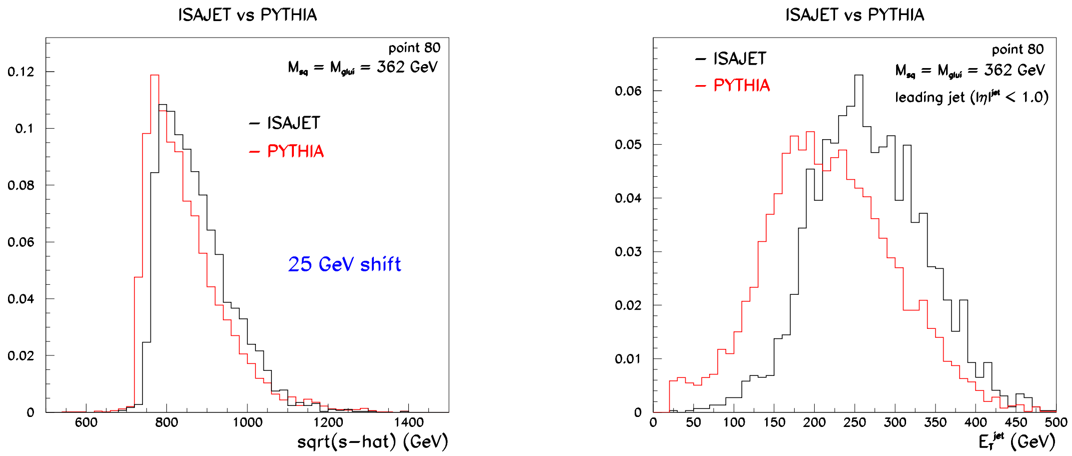

Figure 4: (left) Difference on $\hat{s}$ between ISAJET and PYTHIA. (right) Difference on the transverse energy of the leading jet at the hadron level.

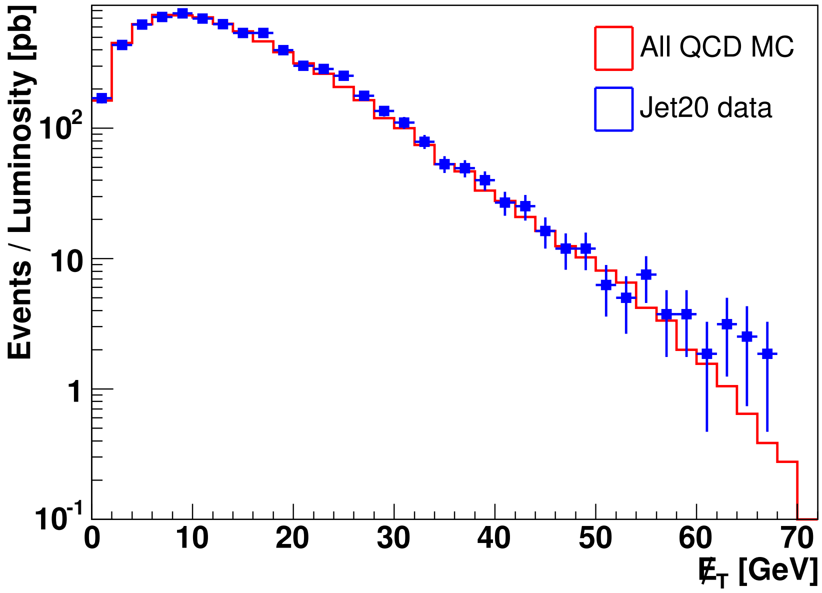

Figure 5: $\not\!\!E_T$ distribution for the JET20 data and all the QCD multijet MC.

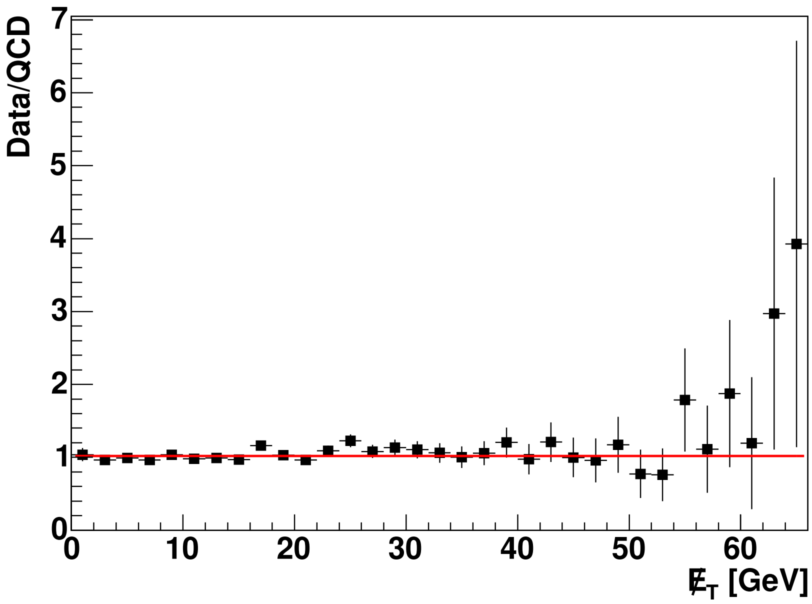

Figure 6: Ratio between data and QCD multijet MC for the $\not\!\!E_T$ distribution.

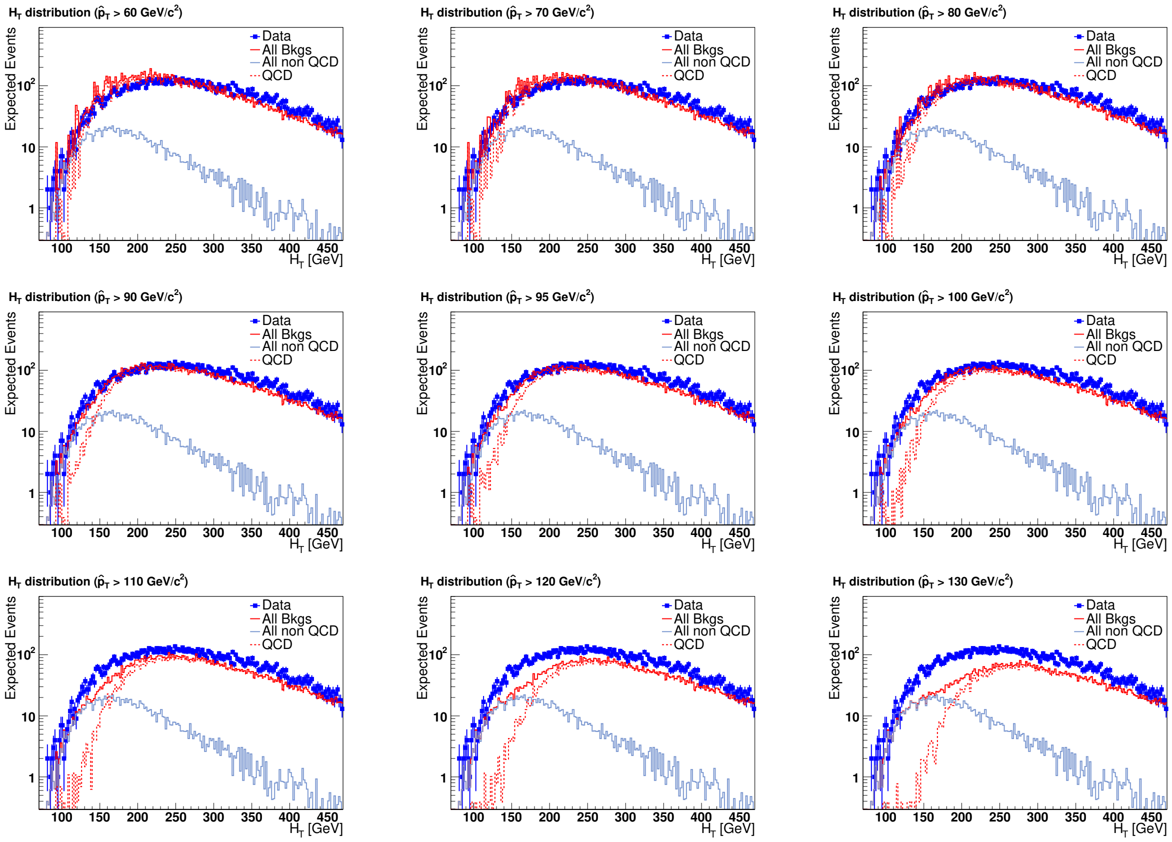

Figure 7: $\mathrm{H_T}$ distributions for different minimum $\hat{\mathrm{p}}_\mathrm{T}$ cuts.

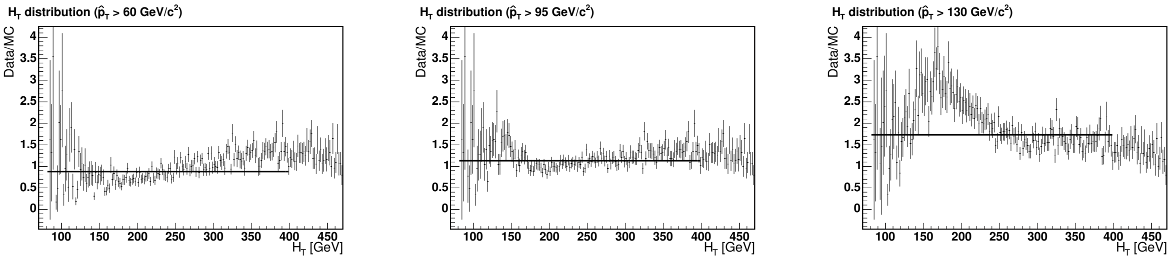

Figure 8: Ratio between the $\mathrm{H_T}$ distributions of data and MC for three different $\hat{\mathrm{p}}_\mathrm{T}$ cuts: 60, 95, and 130 GeV respectively. The black line corresponds to the fit of the distribution.

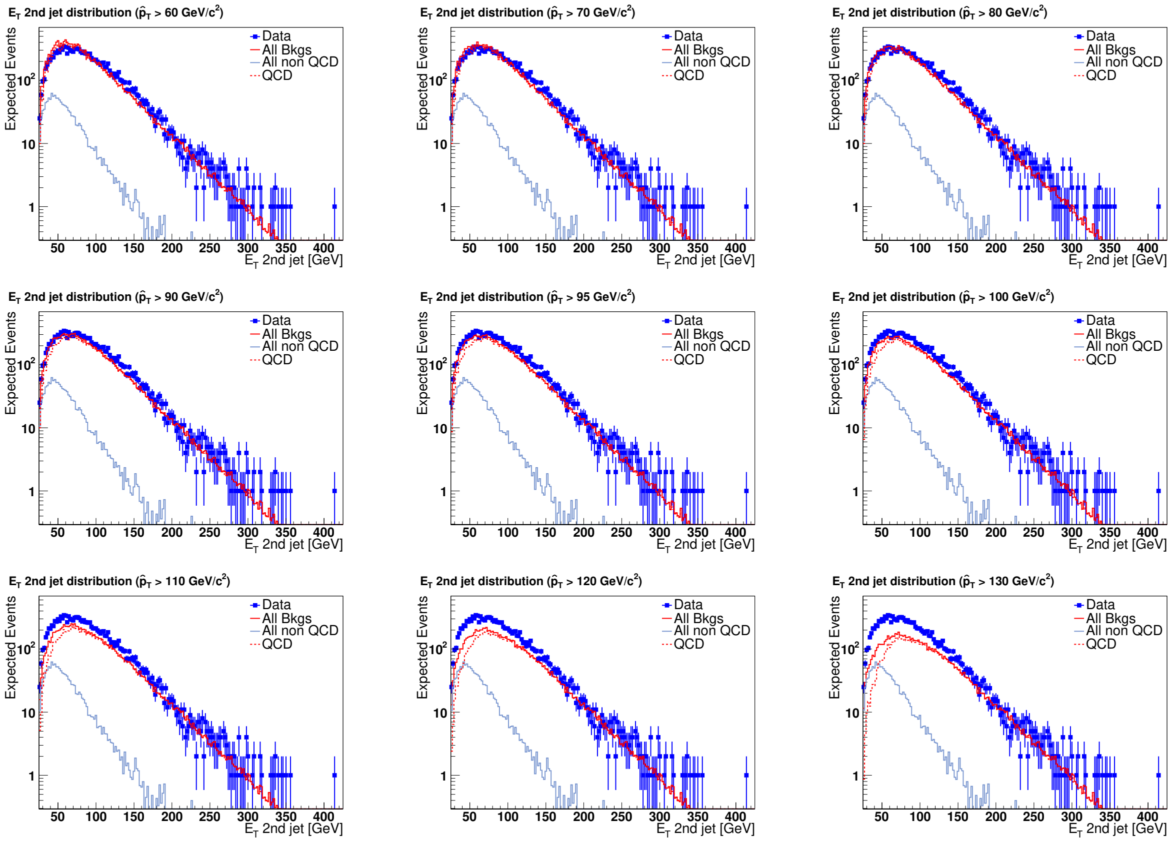

Figure 9: E_T distribution of the second leading jet for different minimum $\hat{p}_T$ cuts.

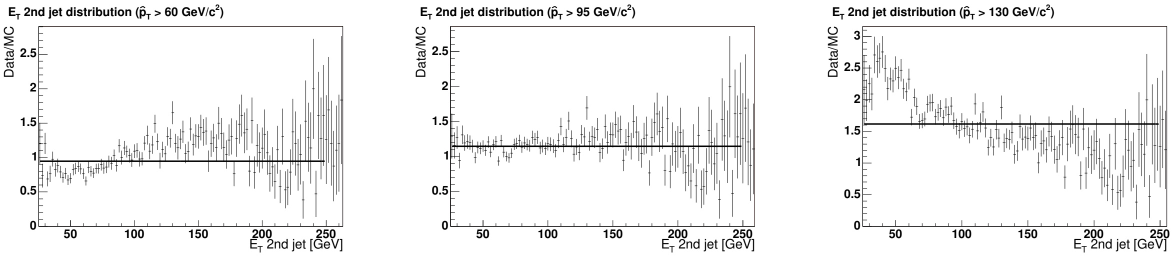

Figure 10: Ratio between the second leading jet's E_T distributions of data and MC for three different $\hat{p}_T$ cuts: 60, 95, and 130 GeV respectively. The black line corresponds to the fit of the distribution.

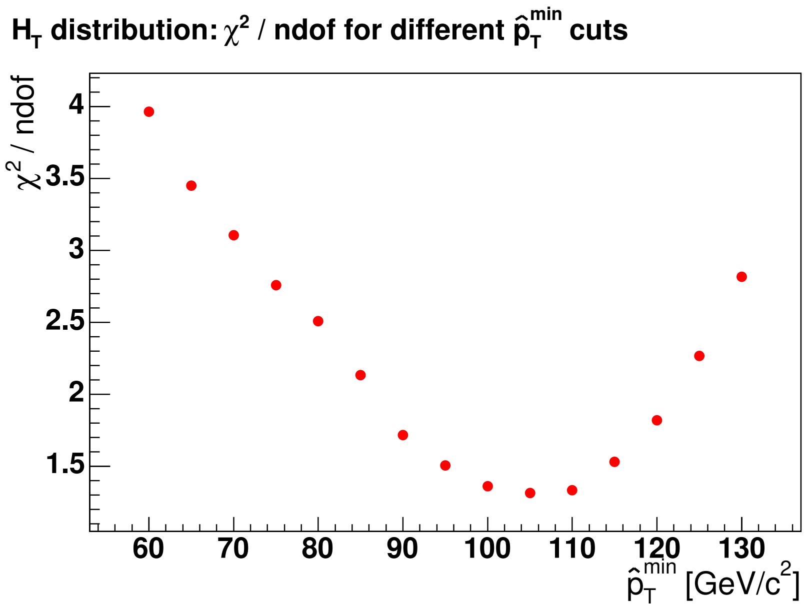

Figure 11: χ^2/d.o.f results from fitting the $\mathrm{H_T}$ distributions to the data. The results suggest a minimum $\hat{\mathrm{p}}_\mathrm{T}$ cut around 95 GeV.

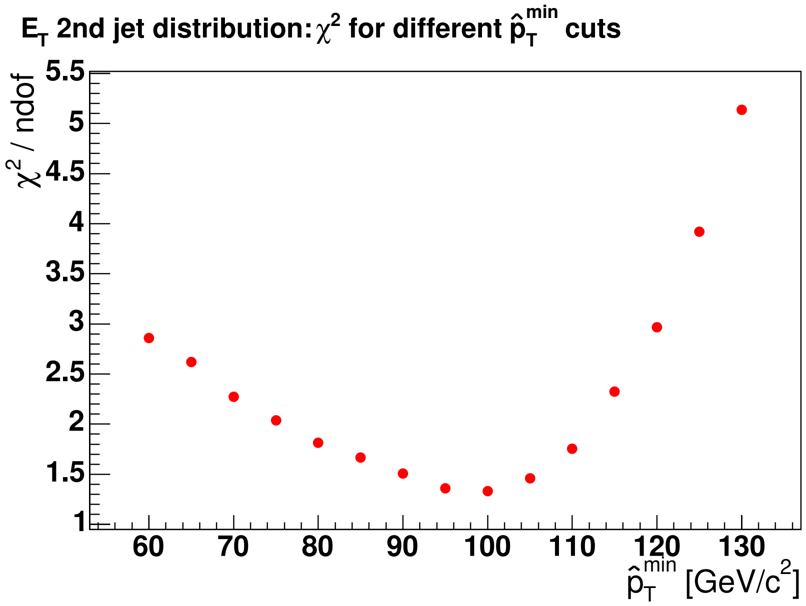

Figure 12: χ^2/d.o.f results from fitting the $\mathrm{E_T^2}$ distributions to the data. The results above suggest a minimum $\hat{\mathrm{p}}_\mathrm{T}$ cut around 100 GeV. This is consistent with the $\mathrm{H_T}$ results shown in figure 11

.

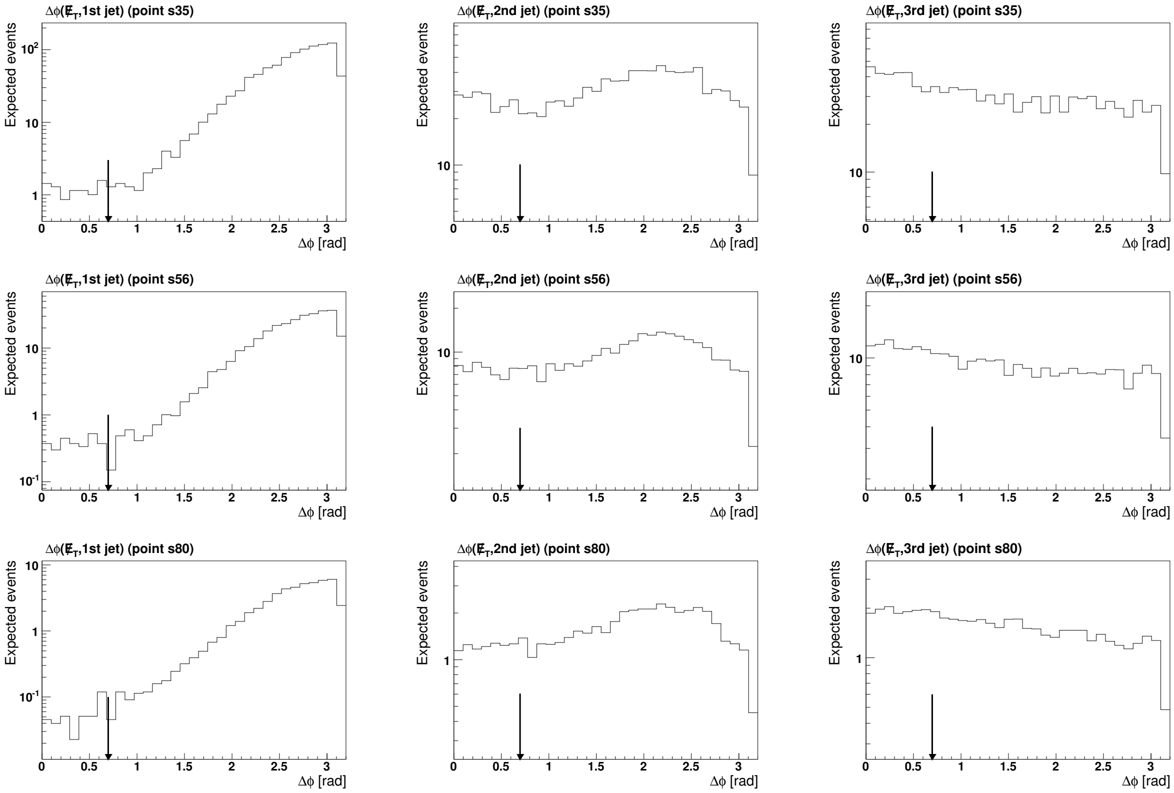

Figure 13: $\Delta\phi(\not\!\!E_{\rm T},\text{jets})$ distributions for the three leading jets of the representative mSUGRA point: s35 (top), s56 (middle), s80 (bottom). The $\not\!\!E_{\rm T}$ in signal events points in a direction away from the jets. The arrow indicates the value of the cut.

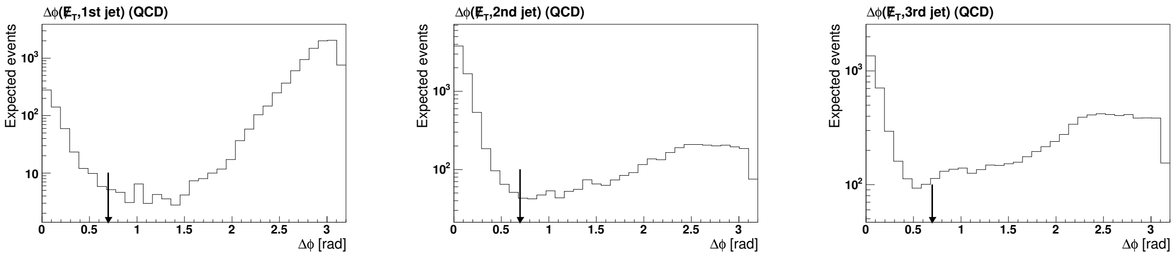

Figure 14: $\Delta\phi(\not\!\!E_{\rm T},\text{jets})$ distributions for the three leading jets of the QCD multijet sample. The peak at zero comes from events in which one of the jets is mismeasured resulting in a $\not\!\!E_{\rm T}$ aligned with the jet. The arrow indicates the value of the cut.

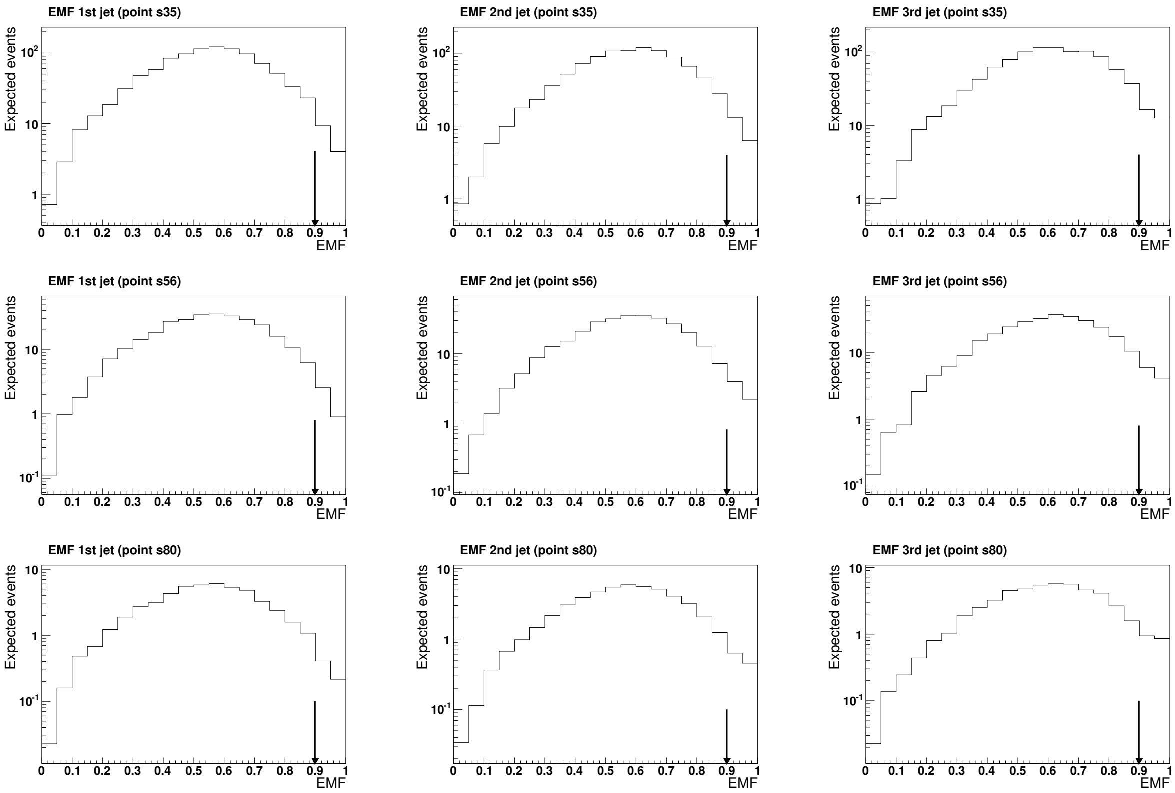

Figure 15: EMF distributions for the three leading jets of the representative mSUGRA point: s35 (top), s56 (middle), s80 (bottom). The arrow indicates the value of the cut.

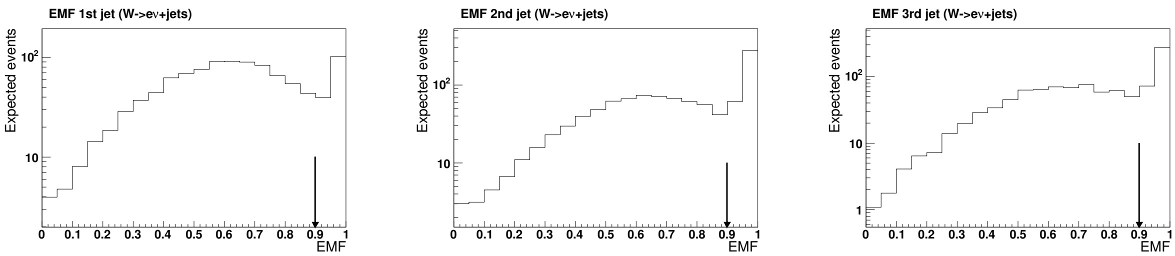

Figure 16: EMF distribution for the leading jets of the W $\rightarrow$ eν sample. A large fraction of the jets have an EMF close to one. These jets are most likely electrons. The arrow indicates the value of the cut.

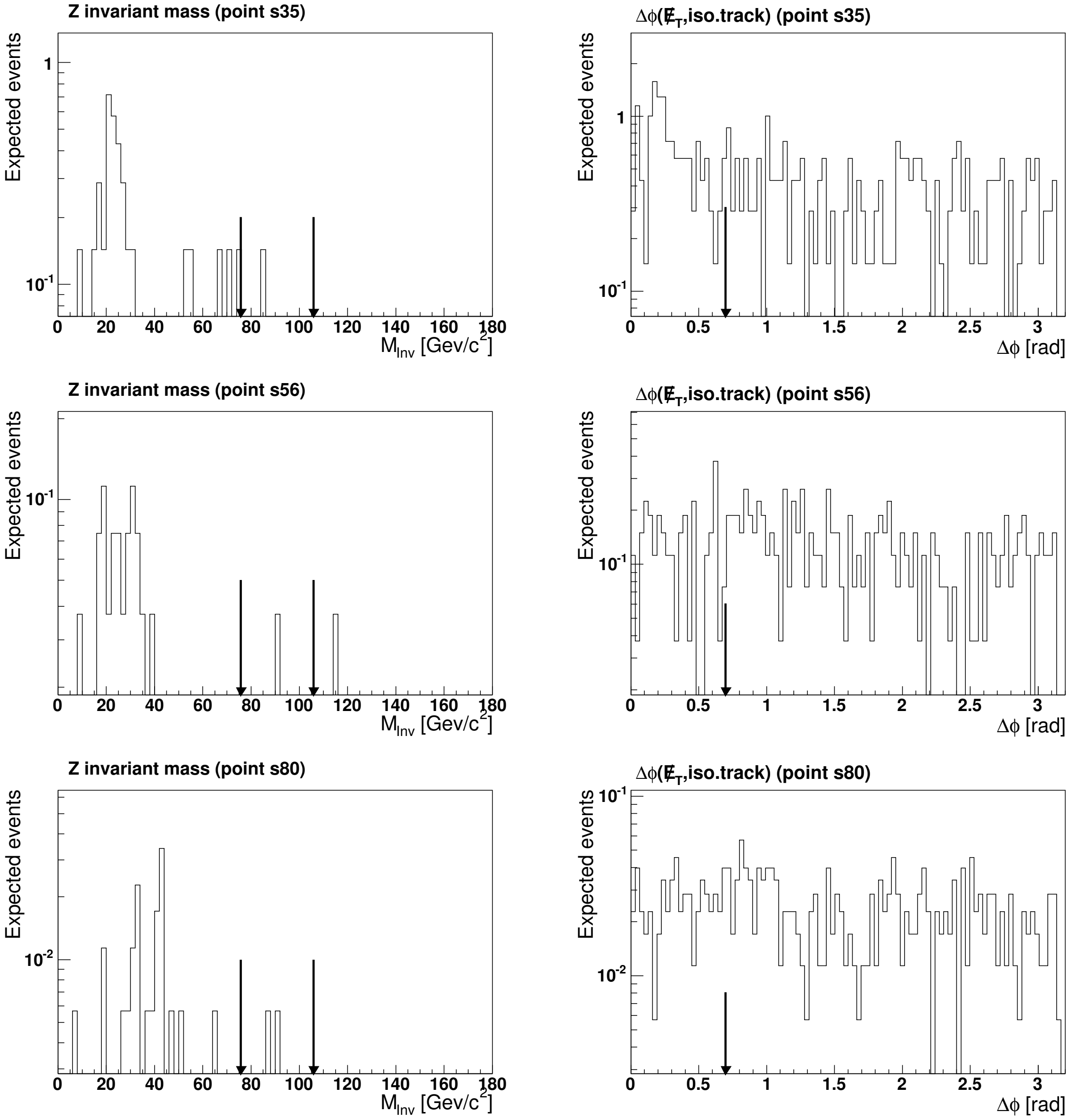

Figure 17: The left column shows the distribution of the invariant mass of the two highest isolated tracks. The right column shows the distribution of the azimuthal angle between the $\not\!\!E_{\mathrm{T}}$ and the highest isolated track. Plots are shown for s35 (top), s56 (middle), and s80 (bottom). The arrows show where the different cuts are placed.

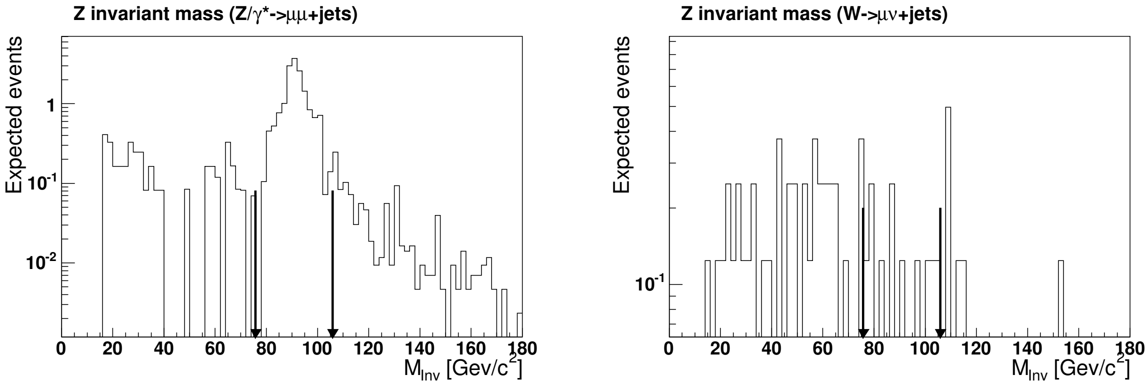

Figure 18: Invariant mass distribution of the two highest isolated tracks in the event. The plot on the left corresponds to $Z/\gamma^* \to \mu\mu$, while the plot on the right corresponds to $W \to \mu\nu$. This cut does little to reduce the $W \to \mu\nu$ background since not many of the events have two or more isolated tracks. However, it rejects most of the $Z/\gamma^* \to \mu\mu$ background. The arrows show were the invariant mass window cut is placed.

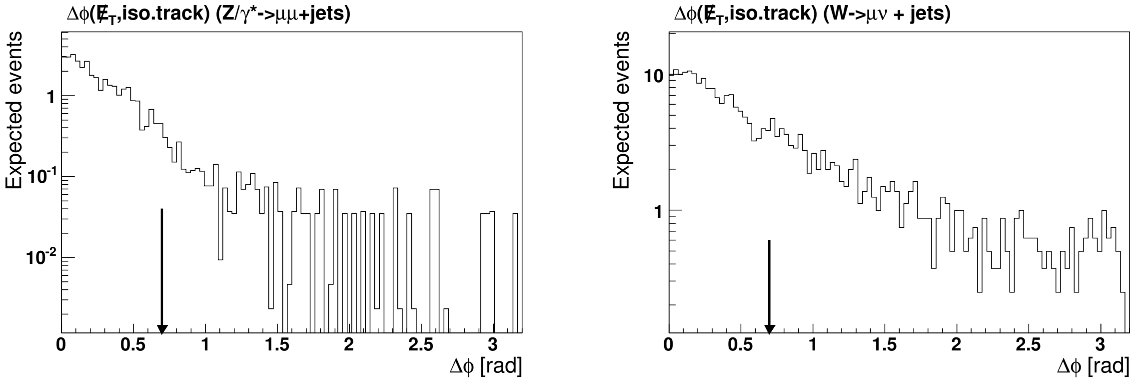

Figure 19: $\Delta\phi(\text{track}, \not{E}_{\mathrm{T}})$ distribution for $Z/\gamma^* \to \mu\mu$ events (left) and $W \to \mu\nu$ events (right). This cut rejects events in which the direction of the $\not{E}_{\mathrm{T}}$ is aligned with that of an isolated track. A significant fraction of the backgrounds is rejected by the cut placed where the arrow indicates.

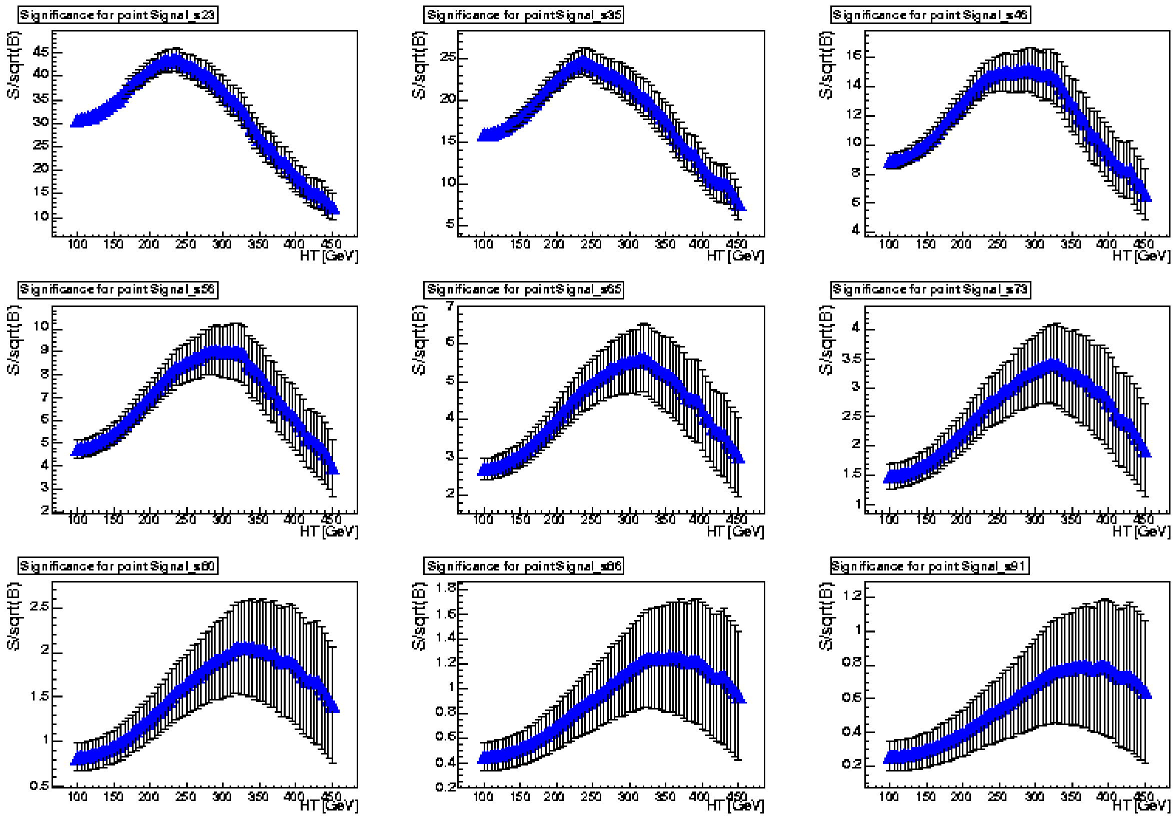

Figure 20: S/$\sqrt{\mathrm{B}}$ distribution for $\mathrm{H_T}$ of the mSUGRA points along the diagonal.

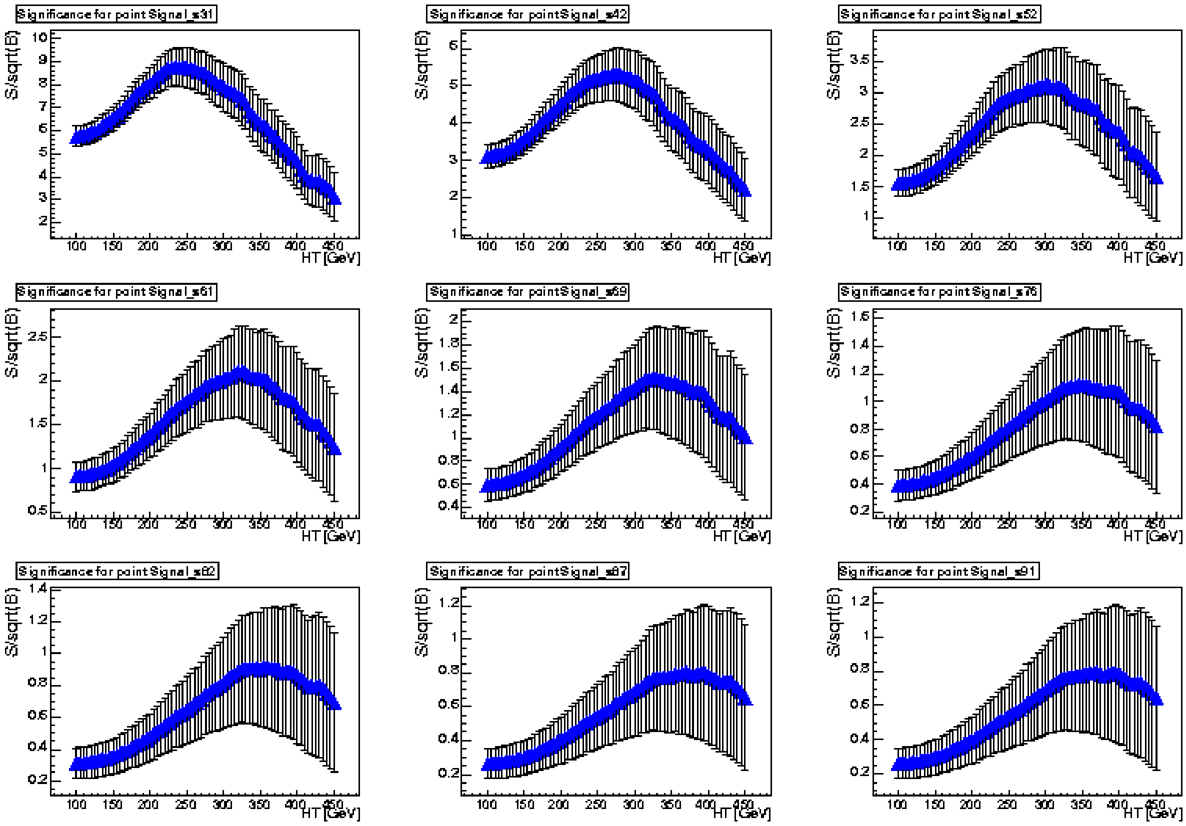

Figure 21: $\mathrm{S}/\sqrt{\mathrm{B}}$ distributions for $\mathrm{H_T}$ of the mSUGRA points along the row.

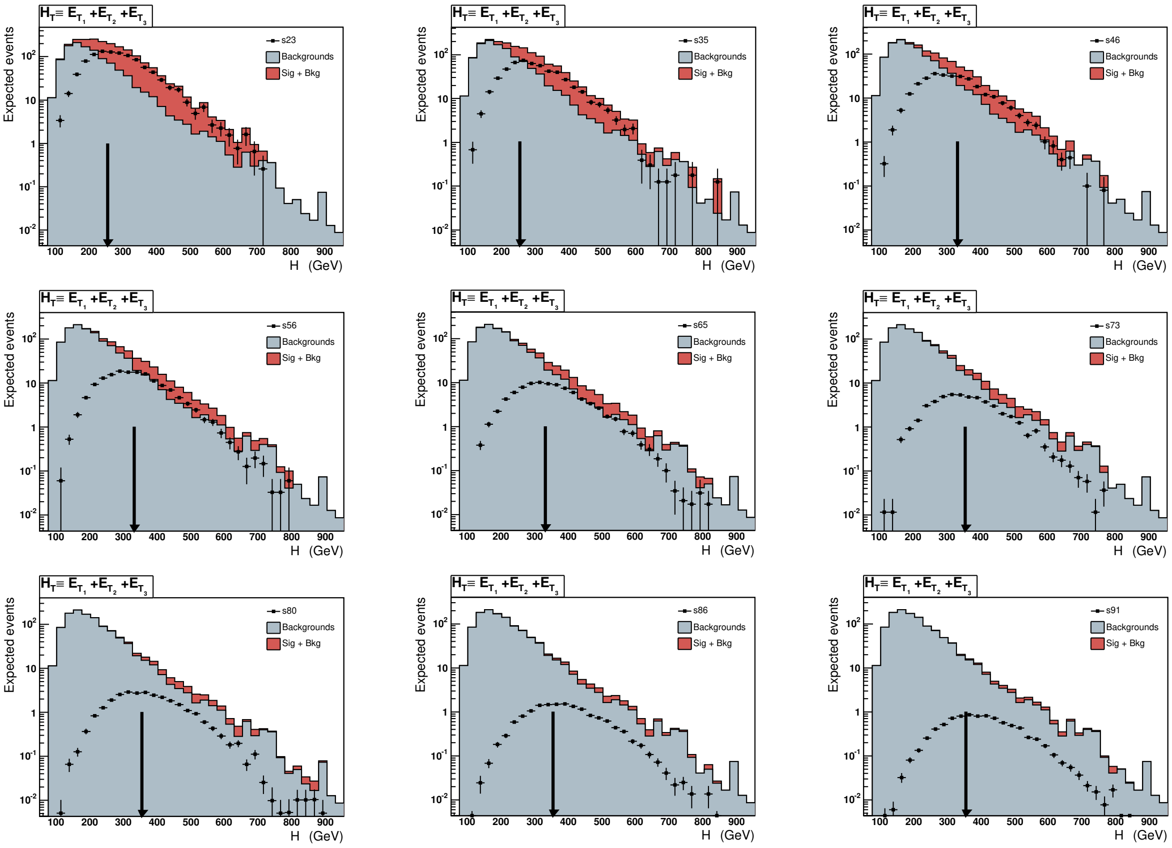

Figure 22: H_T distributions for all the points in the diagonal ($M_{\tilde{q}} \approx M_{\tilde{g}}$). The arrow shows where the cut is placed for each different zone. The first two plots correspond to zone A (points s23, and s35), the next four plots correspond to zone B (points s46, s56, and s65), and the last three plots correspond to zone C (points s73, s80, s86, and s91).

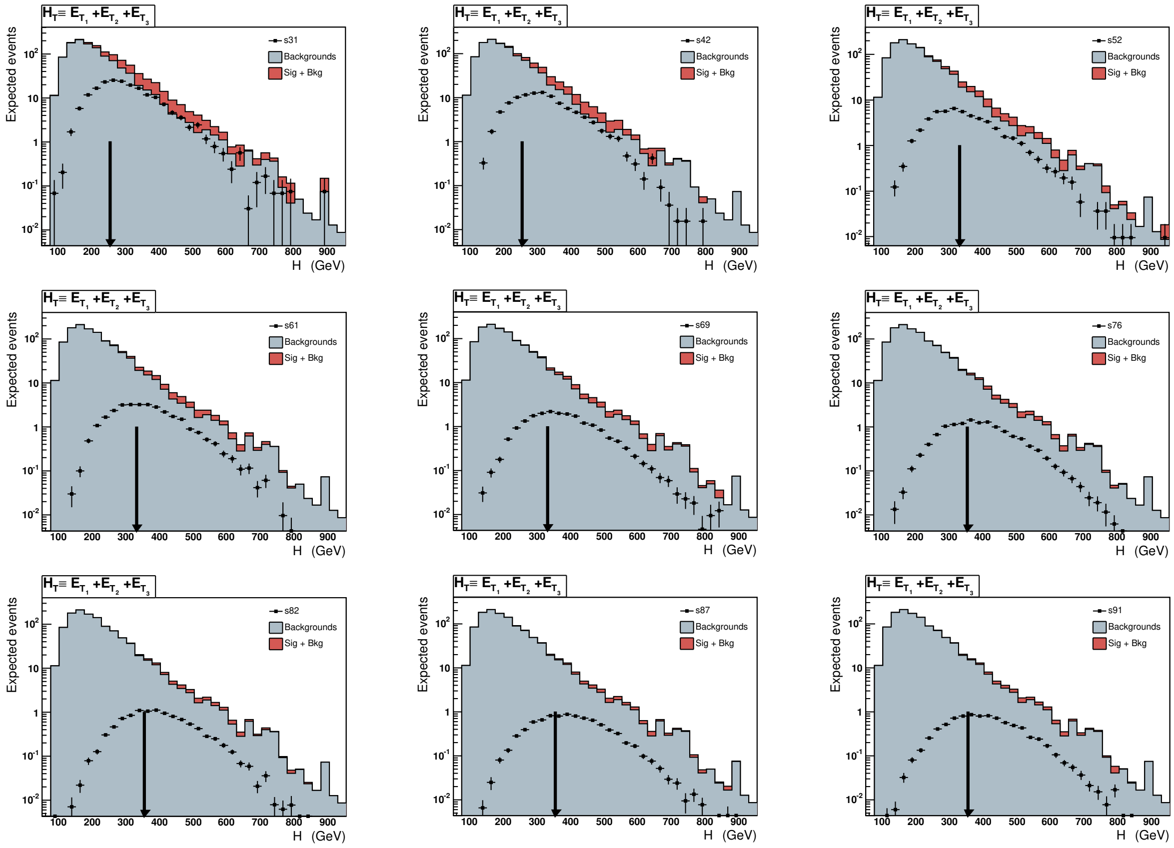

Figure 23: H_T distributions for all the points in the chosen row (gluino mass increases as the point number increases). The arrow shows where the cut is placed for each different zone. The first two plots correspond to zone A (points s31, and s42), the next four histograms correspond to zone B (points s52, s61, and s69), and the last three plots correspond to zone C (points s76, s82, s87, and s91).

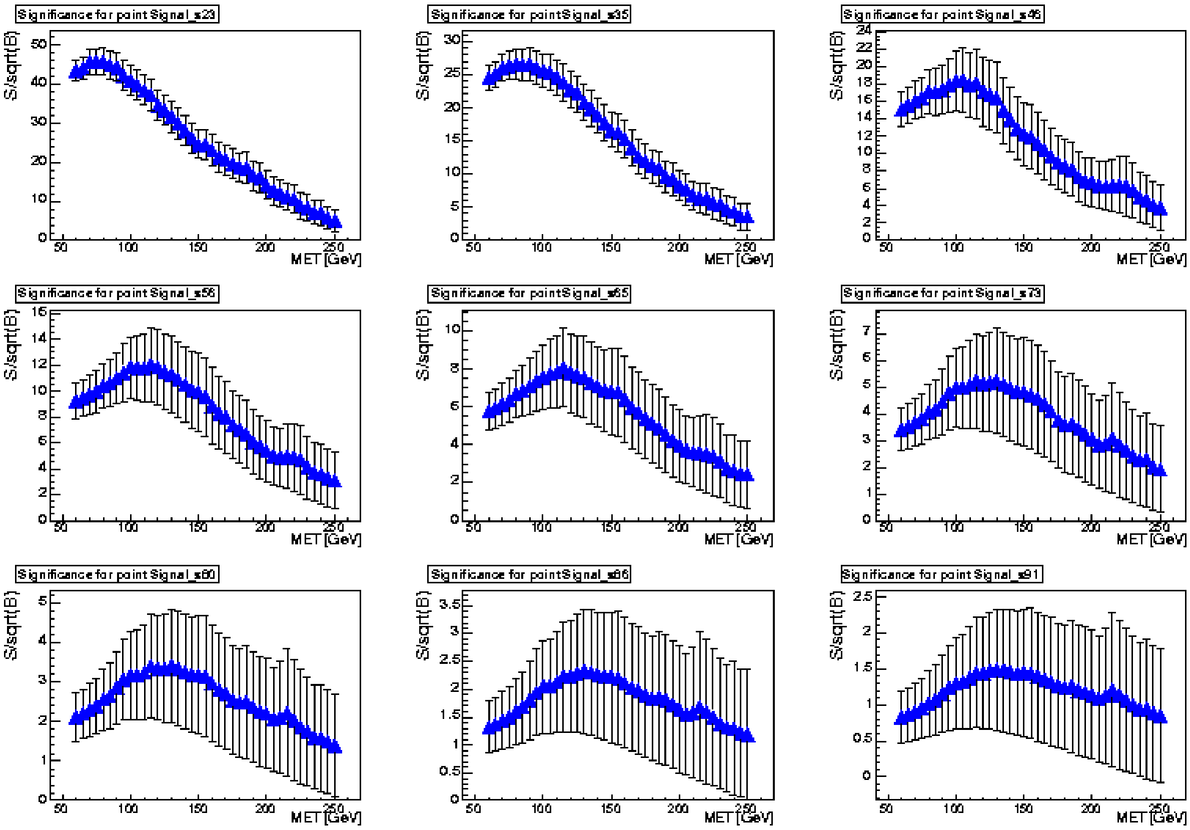

Figure 24: $S/\sqrt{B}$ distribution for $\not\!\!E_T$ of the mSUGRA points along the diagonal.

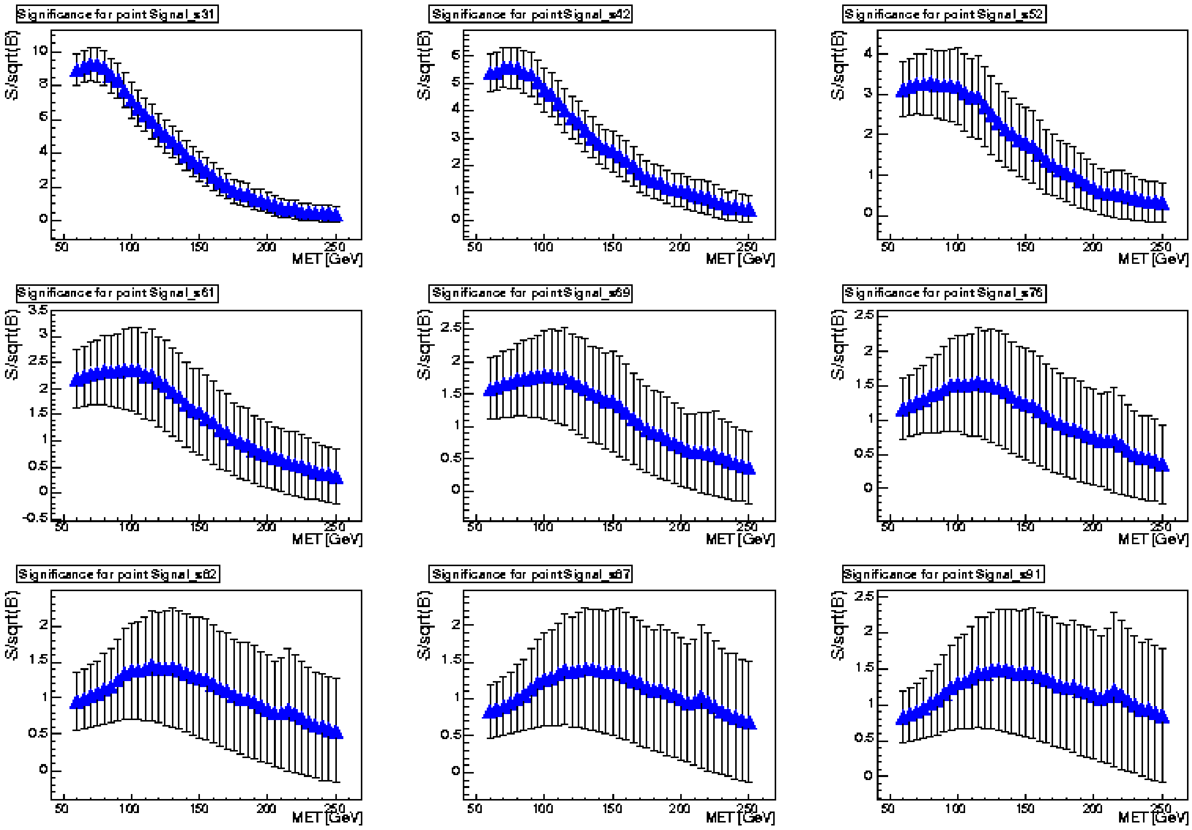

Figure 25: $\mathrm{S}/\sqrt{\mathrm{B}}$ distributions for $\not{E}_{\mathrm{T}}$ of the mSUGRA points along the row.

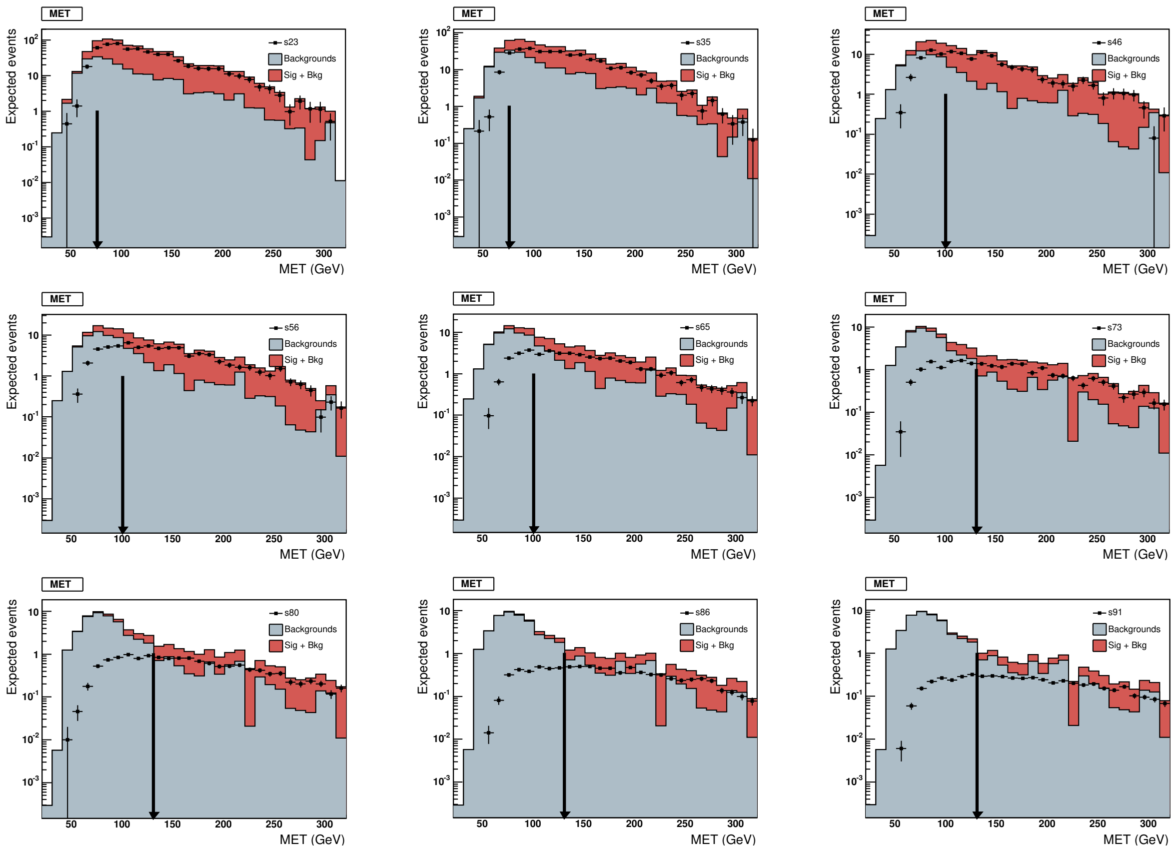

Figure 26: $\not\!\!E_T$ distributions for all the points in the diagonal ($M_{\tilde{q}} \approx M_{\tilde{g}}$). The arrow shows where the cut is placed for each different zone. The first two histograms correspond to zone A (points s23, and s35), the next four plots correspond to zone B (points s46, s56, and s65), and the last three plots correspond to zone C (points s73, s80, s86, and s91).

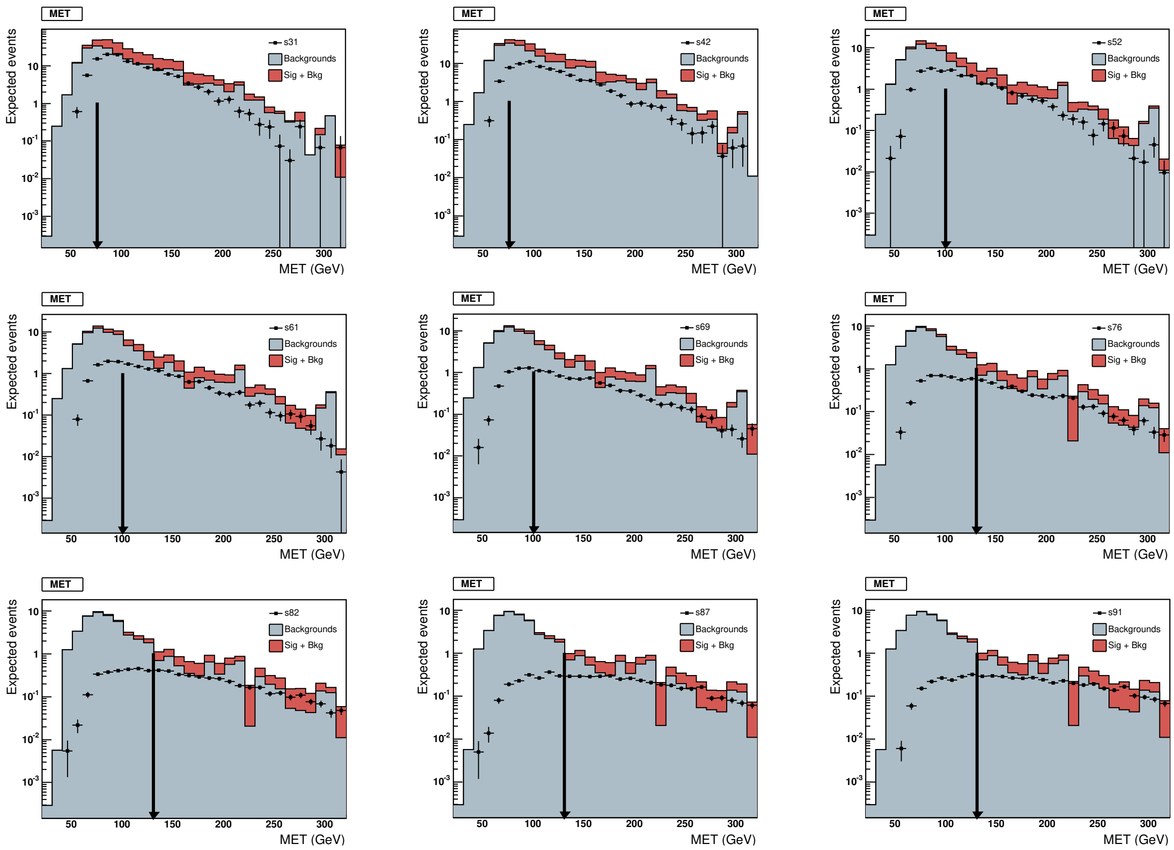

Figure 27: $\not\!\!E_{\mathrm{T}}$ distributions for all the points in the chosen row (gluino mass increases as the point number increases). The arrow shows where the cut is placed for each different zone. The first two plots correspond to zone A (points s31, and s42), the next four plots correspond to zone B (points s52, s61, and s69), and the last three plots correspond to zone C (points s76, s82, s87, and s91).

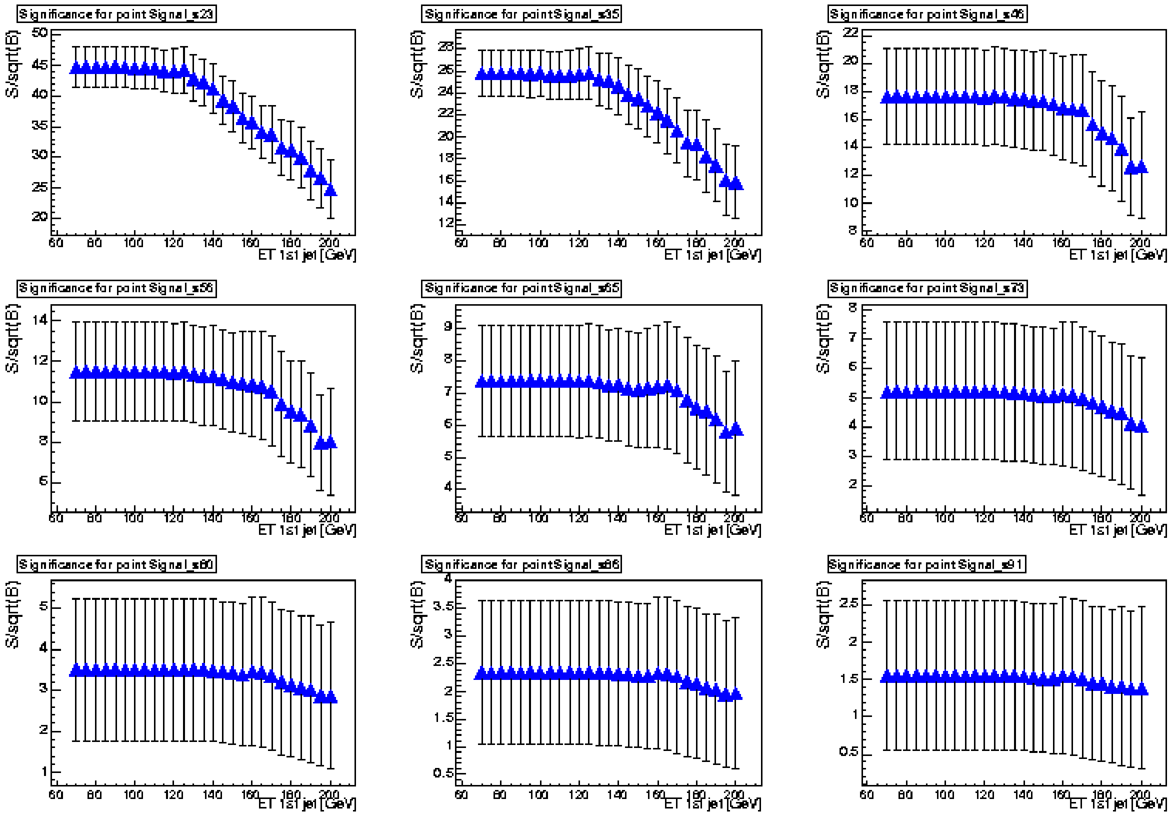

Figure 28: $S/\sqrt{B}$ distribution for $E_T^{\mathrm{jet}\,1}$ of the mSUGRA points along the diagonal ($M_{\tilde{q}} \approx M_{\tilde{g}}$). After applying the H_T and $\not\!\!E_T$, the signal and background distributions have the same shape. Therefore, the $S/\sqrt{B}$ becomes flat until it starts to drop.

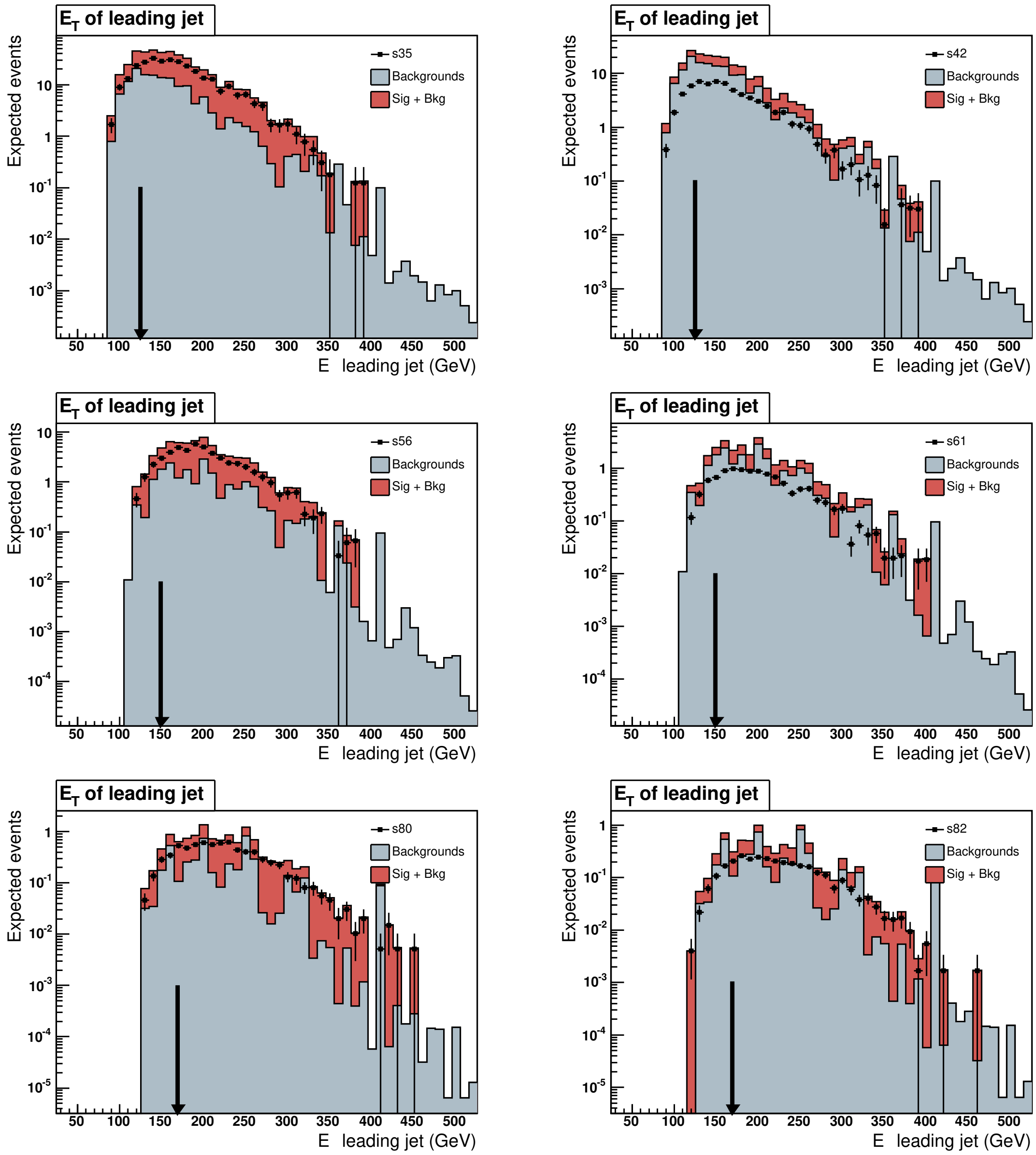

Figure 29: $E_T^{\text{jet }1}$ distributions for points s35, s56, and s80 on the left, and points s42, s61, and s82 on the right (each pair of histograms corresponds to points belonging to the same column (same gluino mass) in figure 2). The cut is chosen to remove the low-end tails of the signal distributions.

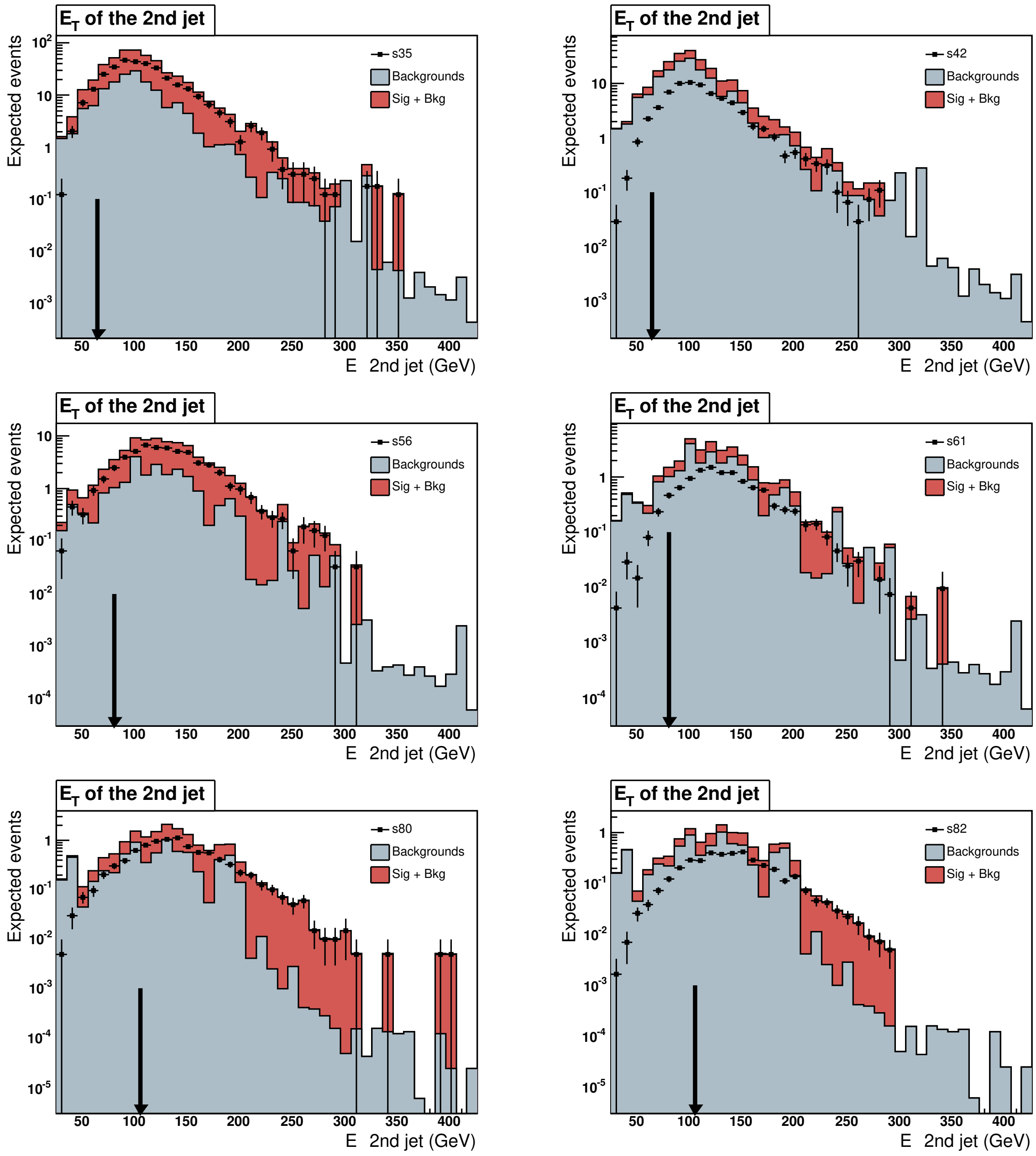

Figure 30: $E_T^{\text{jet 2}}$ distributions for points s35, s56, and s80 on the left, and points s42, s61, and s82 on the right (each pair of histograms corresponds to points belonging to the same column (same gluino mass) in figure 2). The cut is chosen to remove the low-end tails of the signal distributions.

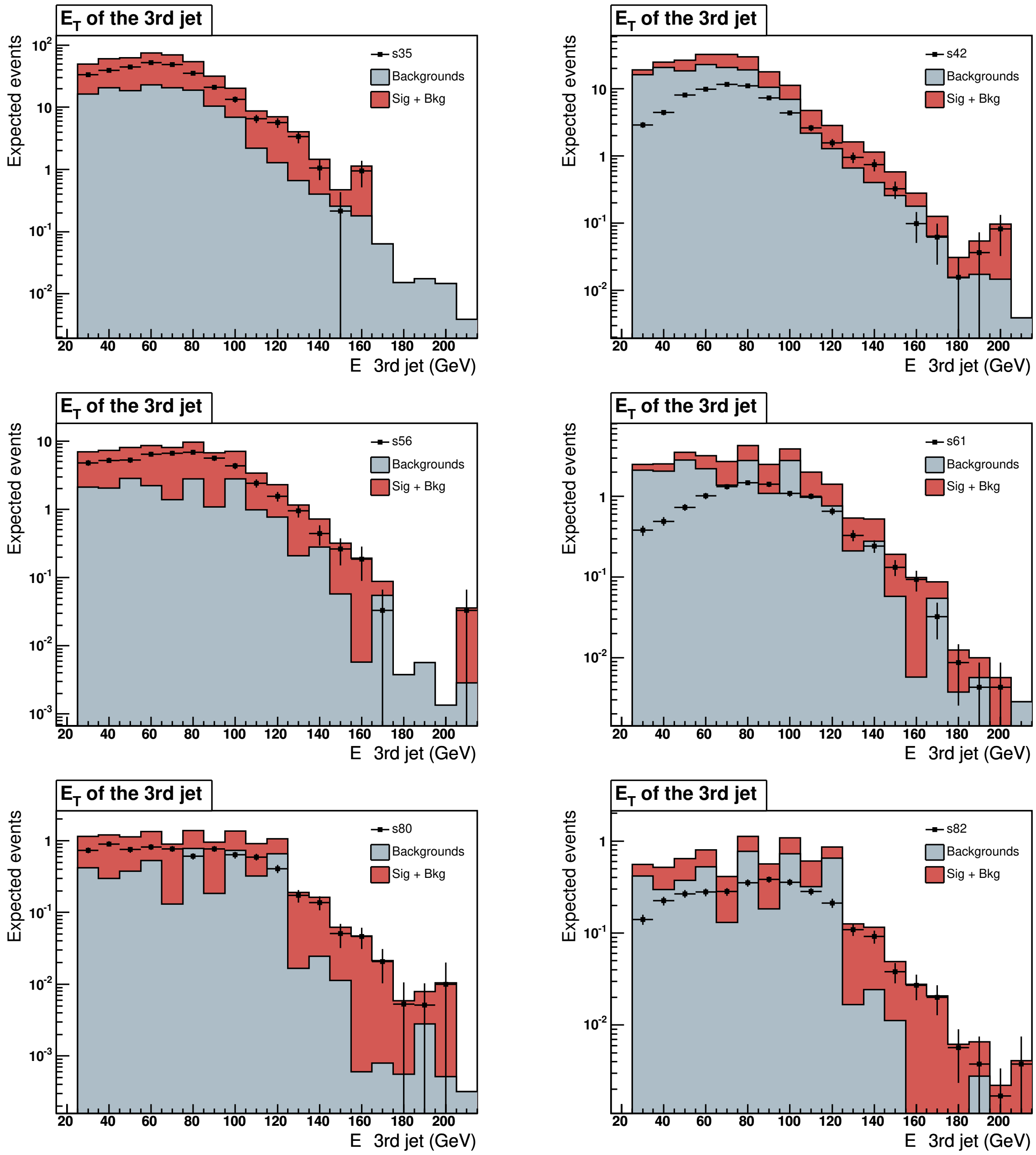

Figure 31: $E_T^{\mathrm{jet}\,3}$ distributions for points s35, s56, and s80 on the left, and points s42, s61, and s82 on the right (each pair of histograms corresponds to points belonging to the same column (same gluino mass) in figure 2). We do not apply a cut to the energy of the third jet except for the pre-selection cut of 25 GeV.

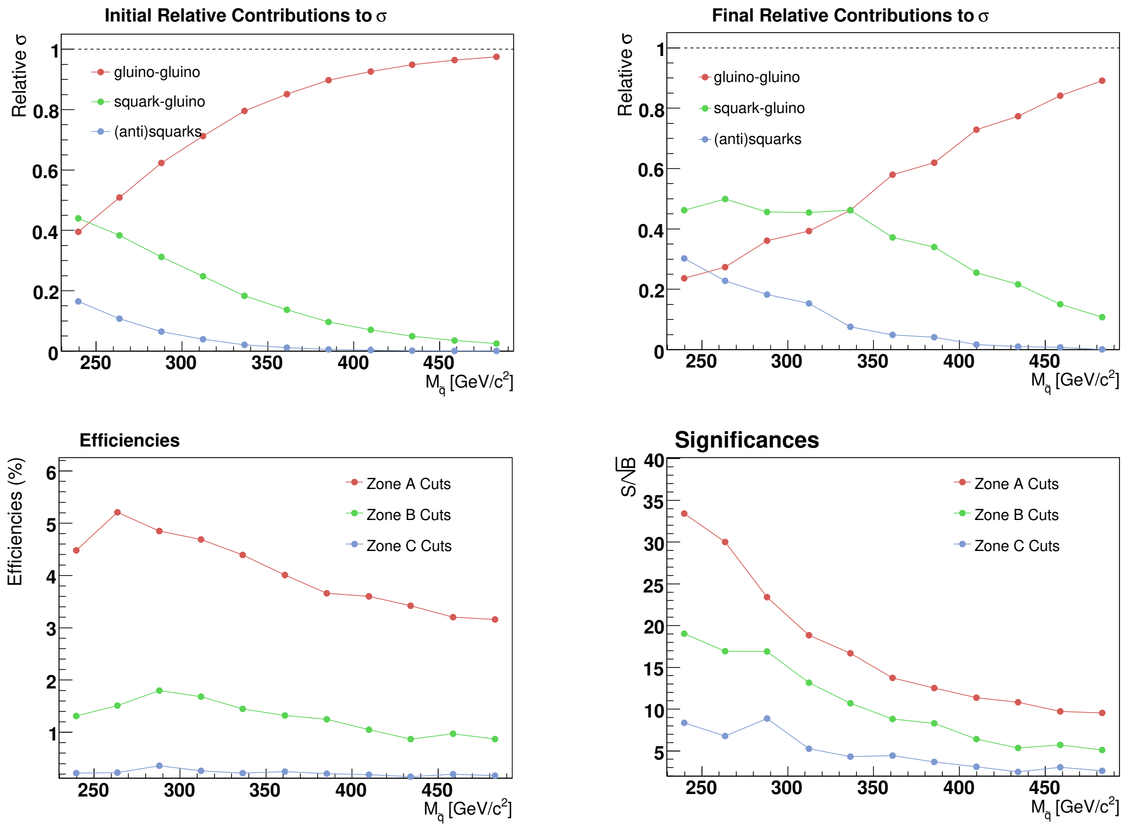

Figure 32: Different relative contributions of the signal production processes before the cuts (top-left), after the analysis cuts (top-right), the signal efficiencies (bottom-left) and significances (bottom-right) along a column ($M_{\tilde{g}} \approx 185\text{GeV/c}^2$).

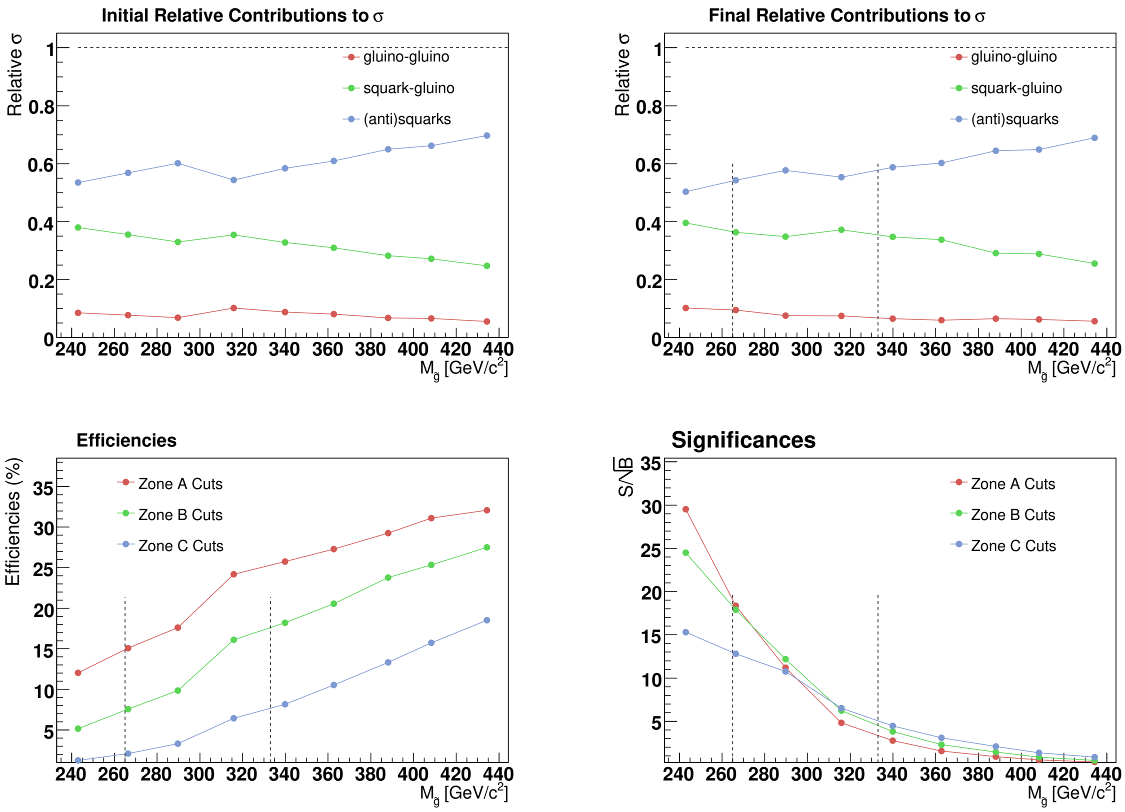

Figure 33: Different relative contributions of the signal production processes before the cuts (top-left), after the analysis cuts (top-right), the signal efficiencies (bottom-left) and significances (bottom-right) along the diagonal ($M_{\tilde{g}} \approx M_{\tilde{q}}$).

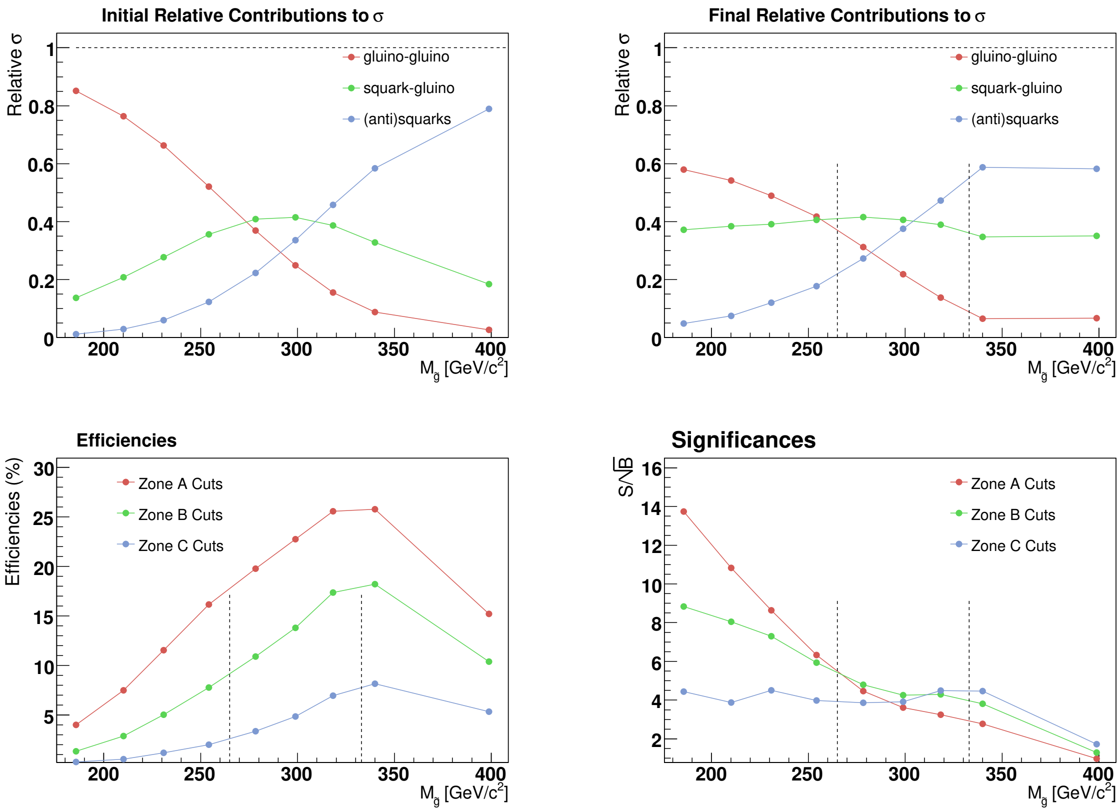

Figure 34: Different relative contributions of the signal production processes before the cuts (top-left), after the analysis cuts (top-right), the signal efficiencies (bottom-left) and significances (bottom-right) along a row ($M_{\tilde{q}} \approx 355\text{GeV/c}^2$).

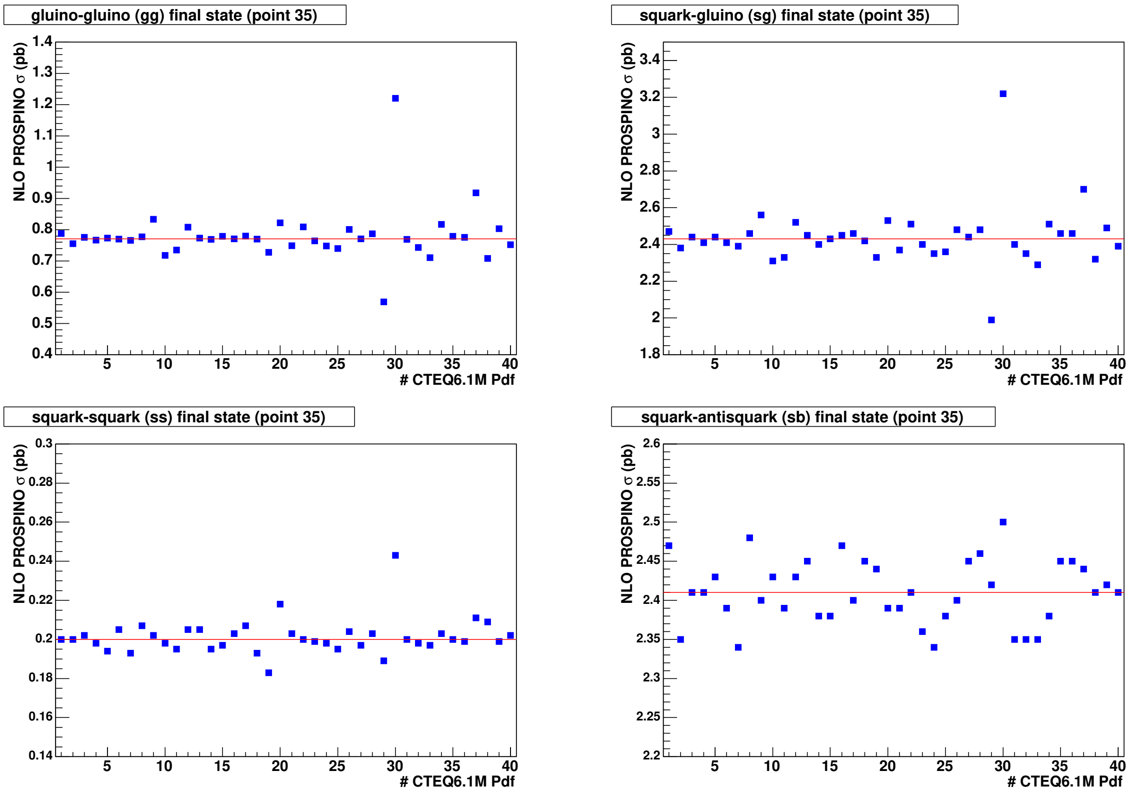

Figure 35: σ_{gg}, σ_{sg}, σ_{ss}, and σ_{sb} distributions for the 40 different PDFs (points) and the nominal PDF (line) for mSUGRA point 35. Each eigenvalue has its plus and minus deviation represented in successive points. The largest deviation corresponds to eigenvalue 15 which is associated with the high-x gluon content. The σ_{sb} plot does not show such deviation as it is dominated by $q\bar{q}$ annihilation.

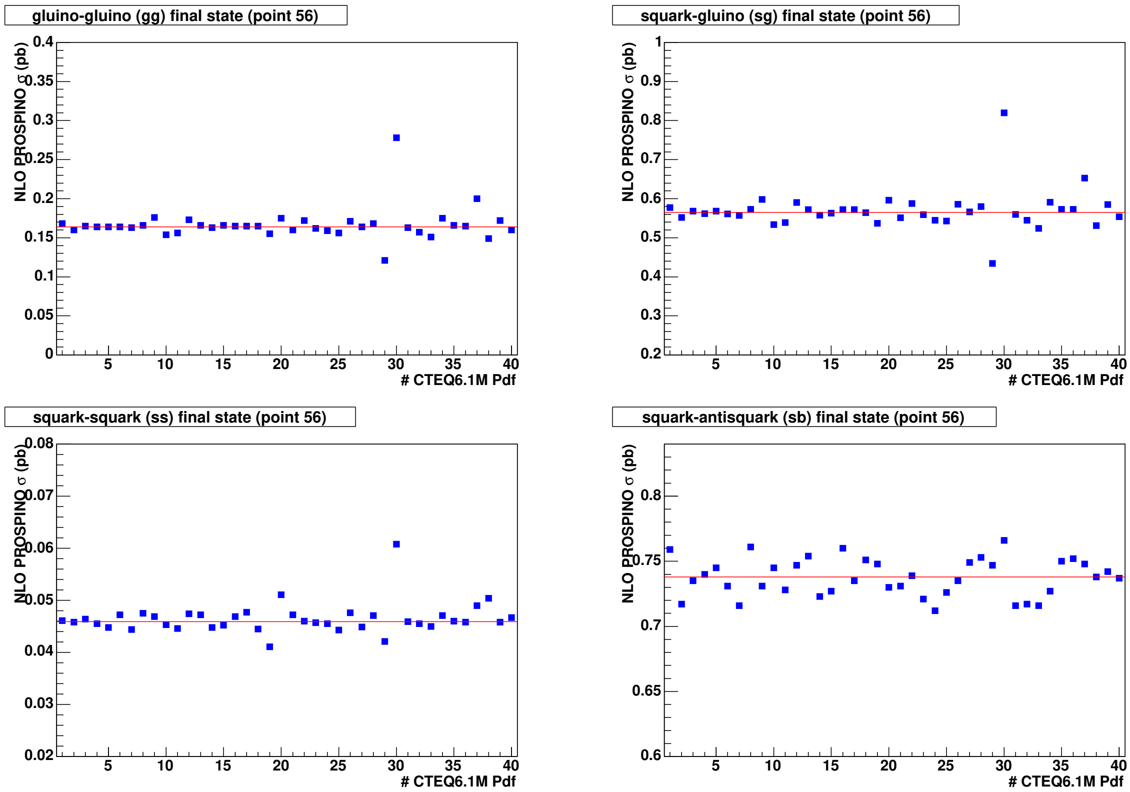

Figure 36: σ_{gg}, σ_{sg}, σ_{ss}, and σ_{sb} distributions for the 40 different PDFs (points) and the nominal PDF (line) for mSUGRA point 56. Each eigenvalue has its plus and minus deviation represented in successive points. The largest deviation corresponds to eigenvalue 15 which is associated with the high-x gluon content. The σ_{sb} plot does not show such deviation as it is dominated by $q\bar{q}$ annihilation.

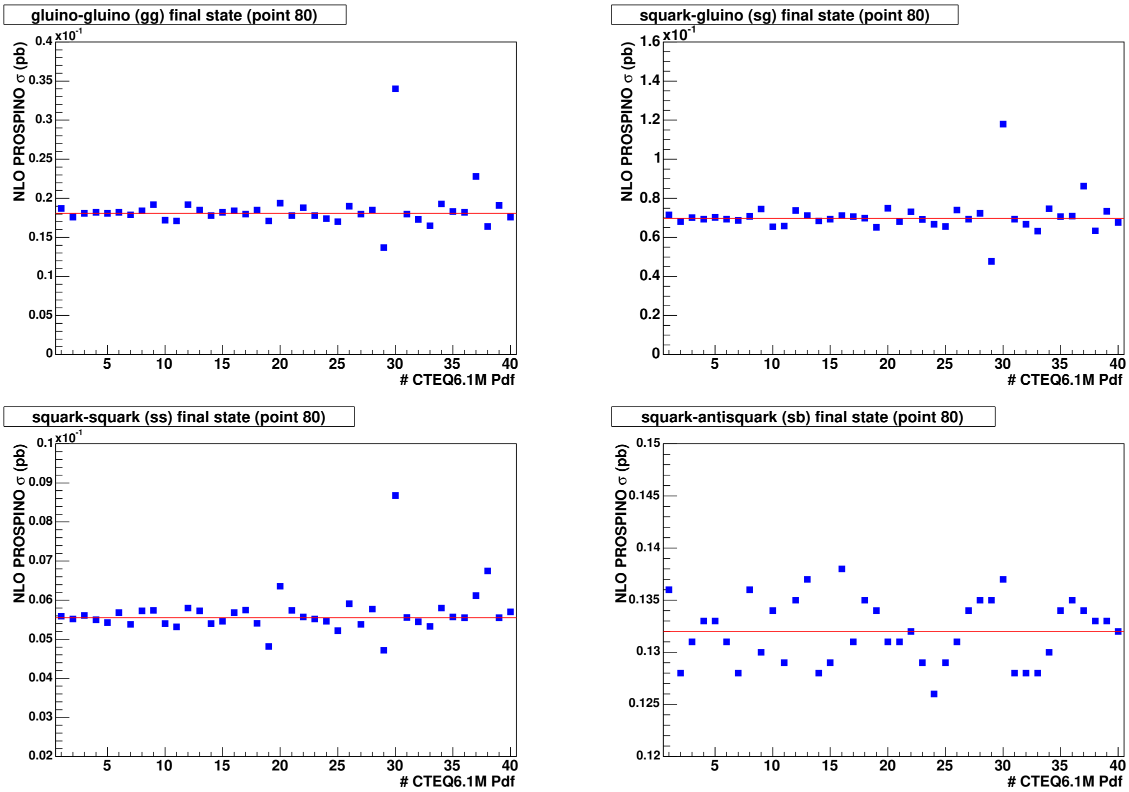

Figure 37: σ_{gg}, σ_{sg}, σ_{ss}, and σ_{sb} distributions for the 40 different PDFs (points) and the nominal PDF (line) for mSUGRA point 80. Each eigenvalue has its plus and minus deviation represented in successive points. The largest deviation corresponds to eigenvalue 15 which is associated with the high-x gluon content. The σ_{sb} plot does not show such deviation as it is dominated by $q\bar{q}$ annihilation.

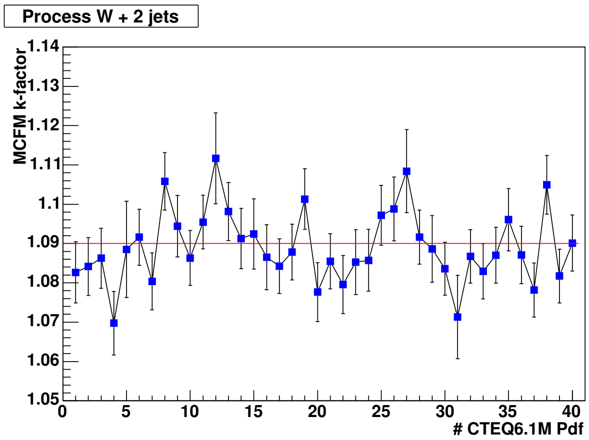

Figure 38: k-factors for the 40 different PDFs (points) and the nominal PDF (line). for W + 2 jets

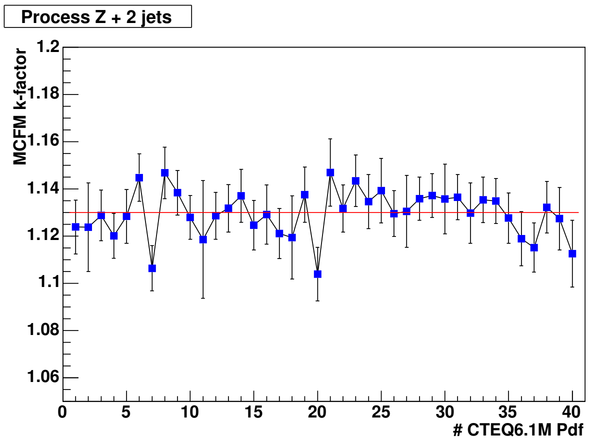

Figure 39: k-factors for the 40 different PDFs (points) and the nominal PDF (line) for Z + 2 jets.

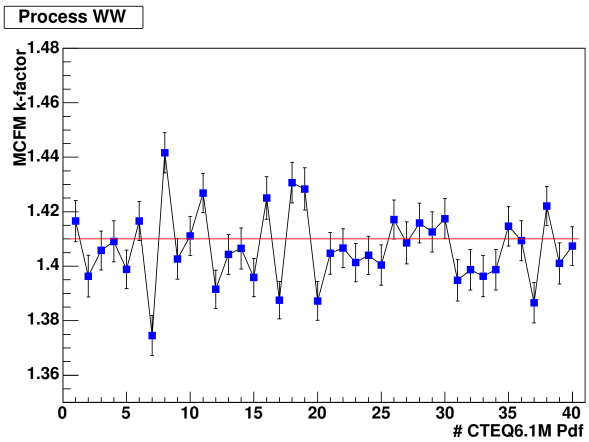

Figure 40: k-factors for the 40 different PDFs (points) and the nominal PDF (line) for WW production.

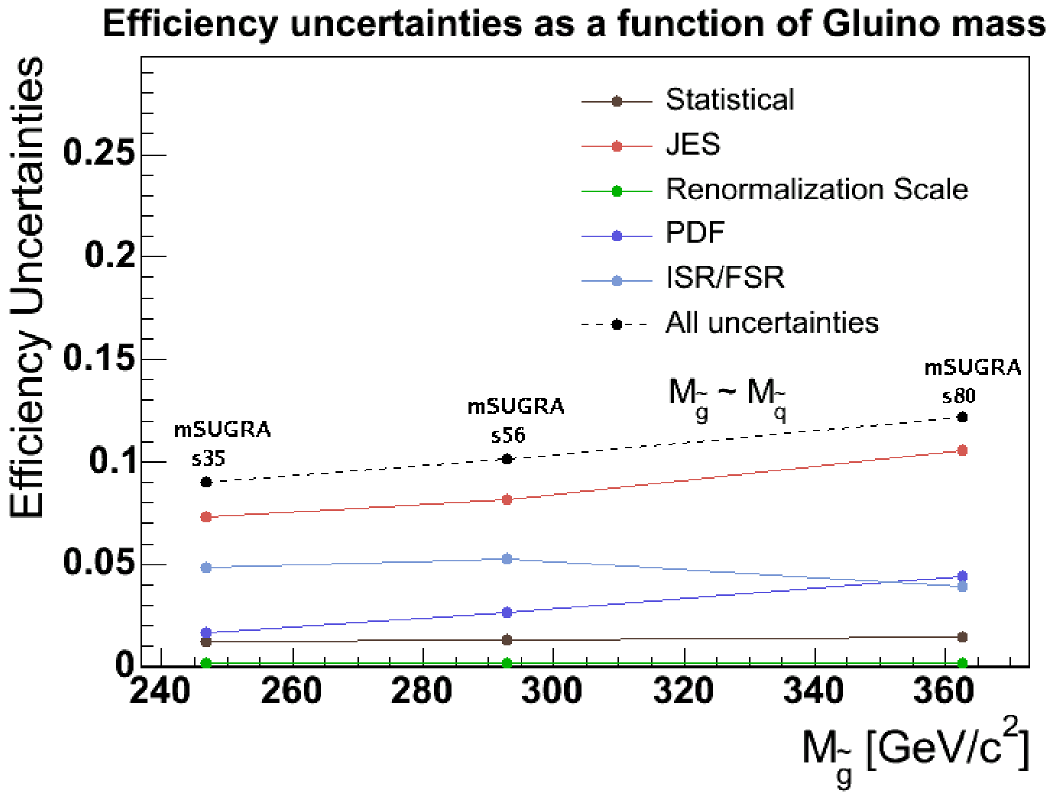

Figure 41: Systematic uncertainties relative to the signal efficiencies for the three representative mSUGRA points s35, s56 and s80.

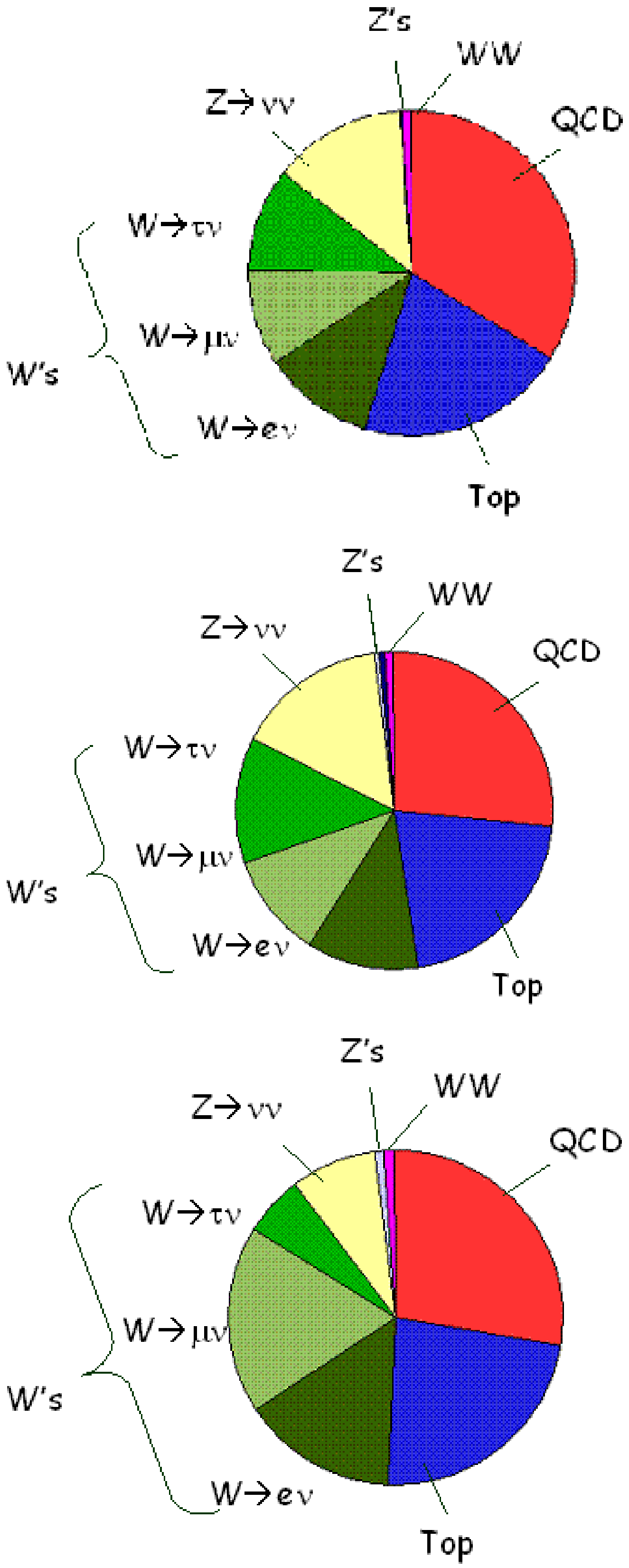

Figure 42: Individual backgrounds relative contributions to the total one after all the cuts have been applied for Zone A (top), Zone B (middle), Zone C (low).

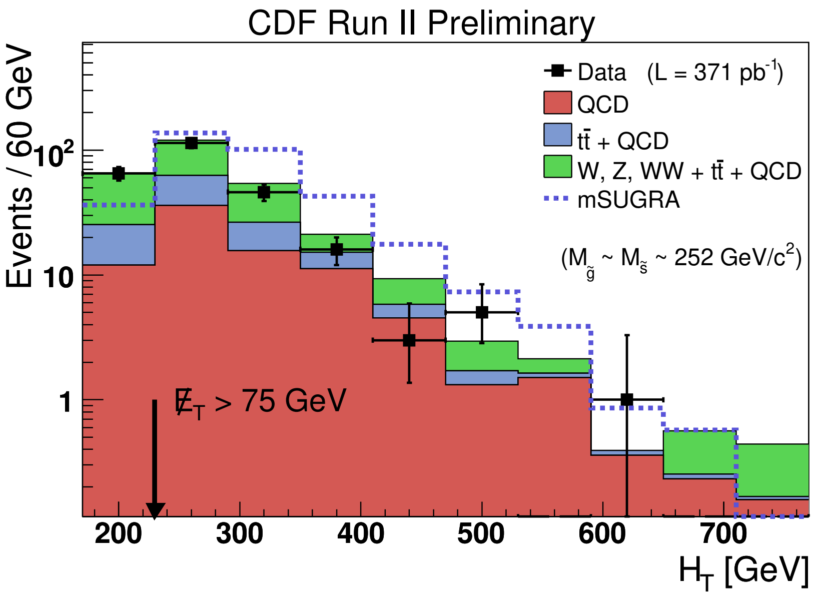

Figure 43: $\mathrm{H_T}$ distribution for the expected number of mSUGRA signal events, and background events in region A. The points correspond to the data events which pass the cuts for the region. Distributions have passed all the cuts except the $\mathrm{H_T}$ one.

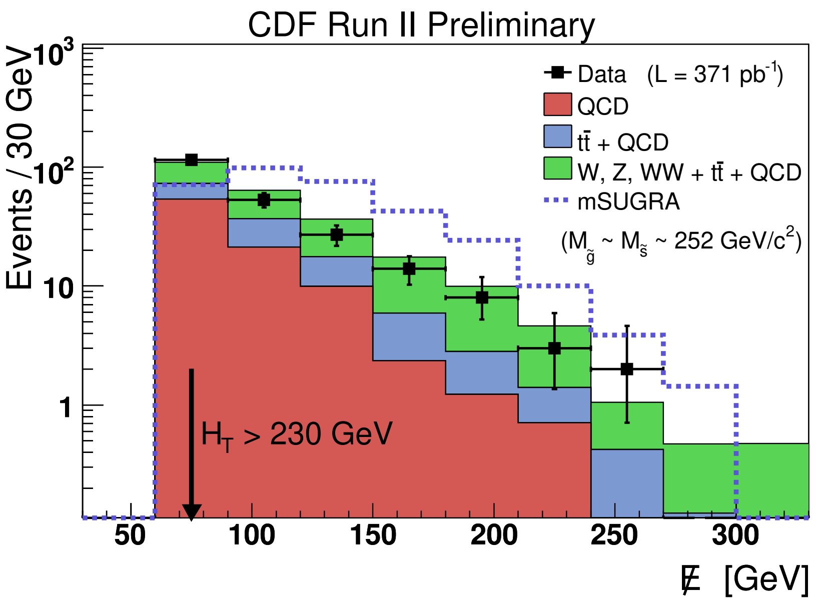

Figure 44: $\not{E}_{\mathrm{T}}$ distribution for the expected number of mSUGRA signal events, and background events in region A. The points correspond to the data events which pass the cuts for the region. Distributions have passed all the cuts except the $\not{E}_{\mathrm{T}}$ one.

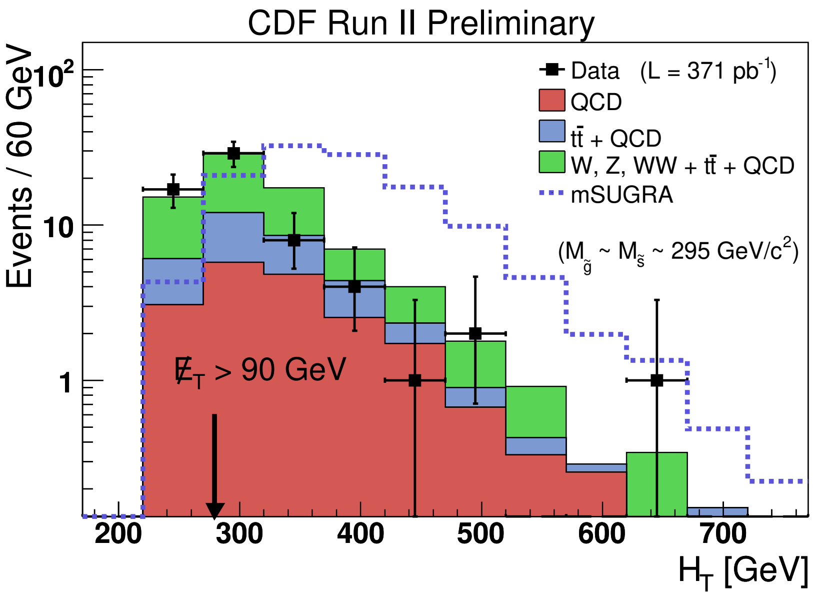

Figure 45: H_T distribution for the expected number of mSUGRA signal events, and background events in region B. The points correspond to the data events which pass the cuts for the region. Distributions have passed all the cuts except the H_T one.

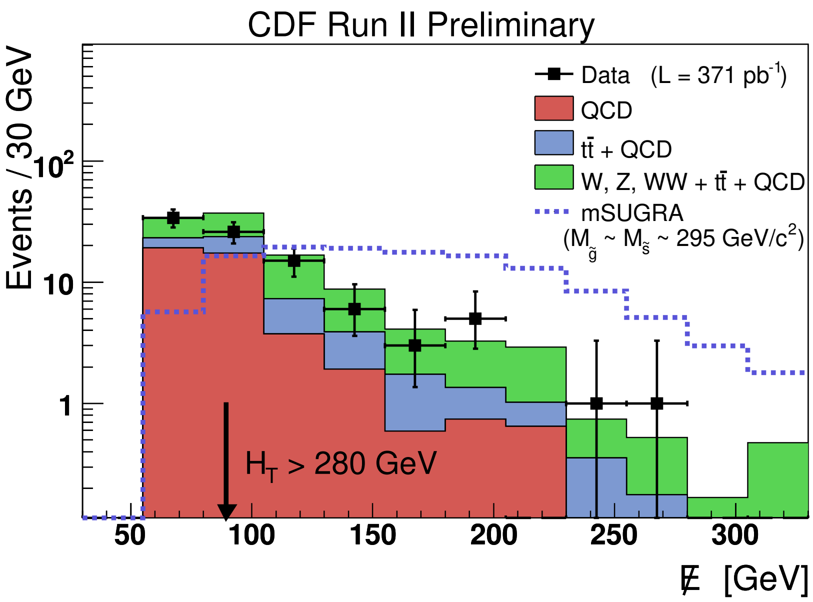

Figure 46: $\not\!\!E_T$ distribution for the expected number of mSUGRA signal events, and background events in region B. The points correspond to the data events which pass the cuts for the region. Distributions have passed all the cuts except the $\not\!\!E_T$ one.

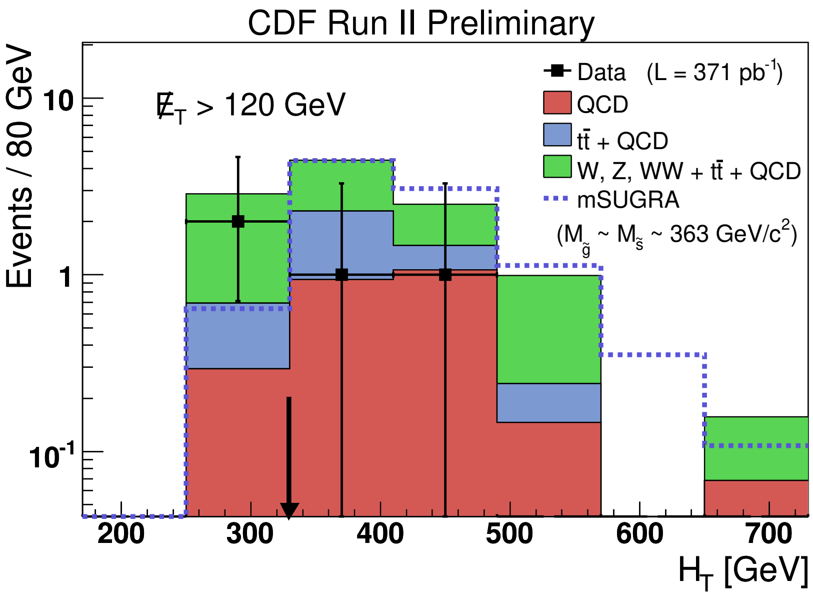

Figure 47: H_T distribution for the expected number of mSUGRA signal events, and background events in region C. The points correspond to the data events which pass the cuts for the region. Distributions have passed all the cuts except the H_T one.

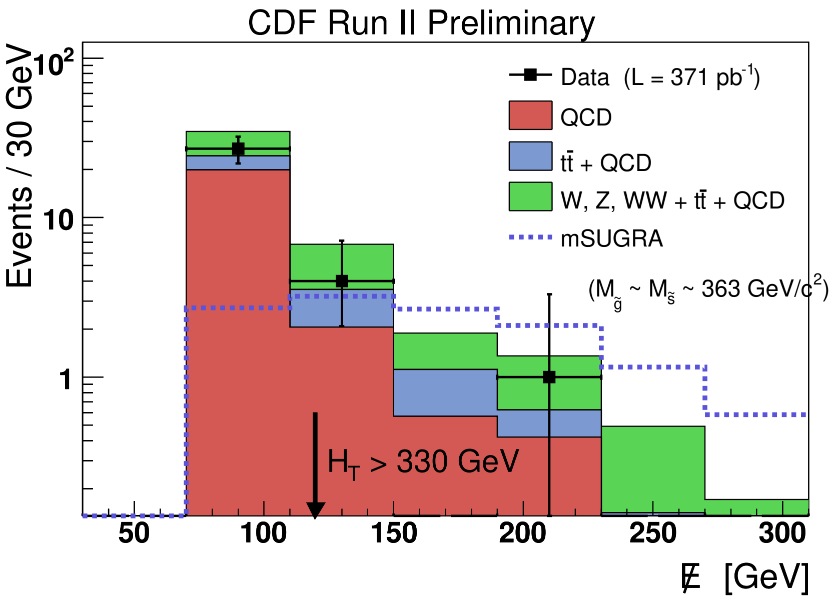

Figure 48: $\not\!\!E_T$ distribution for the expected number of mSUGRA signal events, and background events in region C. The points correspond to the data events which pass the cuts for the region. Distributions have passed all the cuts except the $\not\!\!E_T$ one.

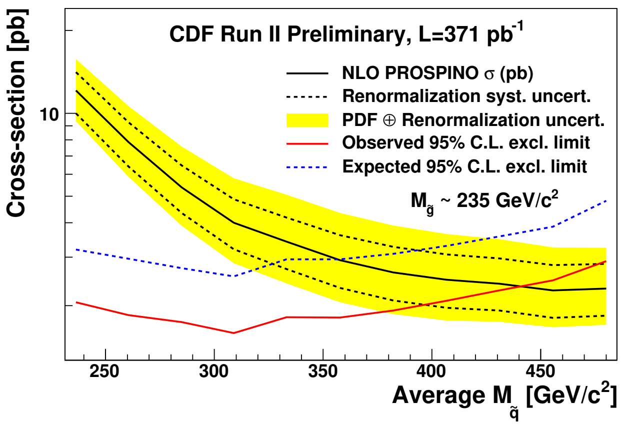

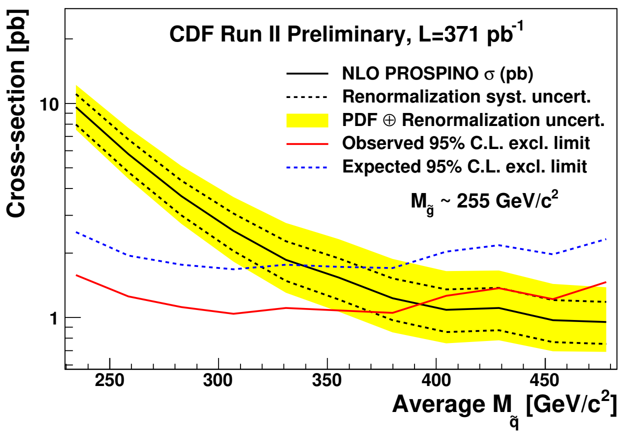

Figure 49: Cross section as a function of squark mass for two $M_{\tilde{g}}$ values (columns). The observed and expected limits at 95% C.L. are also shown. The yellow band shows the total effect of the PDFs and the renormalization scale uncertainties.

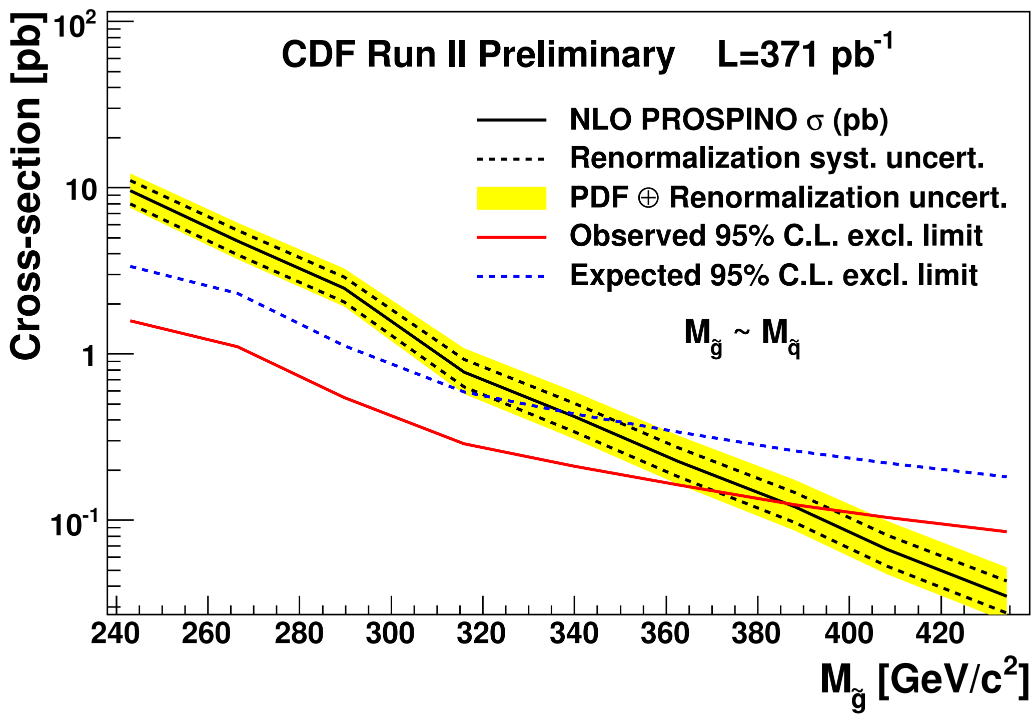

Figure 50: Cross section as a function of gluino/squark masses in the case of $M_{\tilde{q}} \approx M_{\tilde{g}}$ (diagonal). The observed and expected limits at 95% C.L. are also shown. The yellow band shows the total effect of the PDFs and the renormalization scale uncertainties.

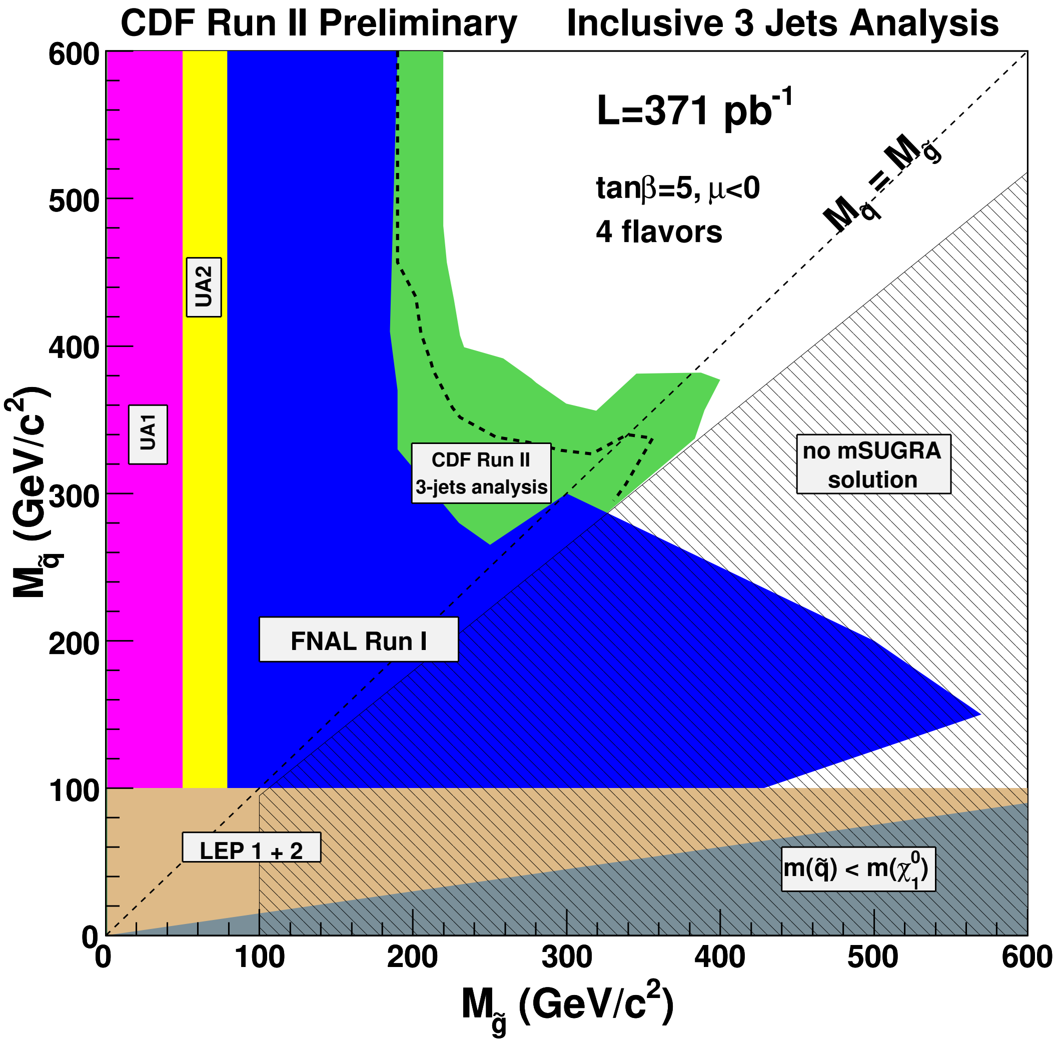

Figure 51: $M_{\tilde{q}}$ - $M_{\tilde{g}}$ exclusion plot at the 95 % C.L in the framework of mSUGRA assuming R-parity conservation. The pink region was excluded by the UA1 experiment [18]. The yellow region was excluded by the UA2 experiment [19]. The blue region was excluded by the CDF and DØ experiments after Run I [20]. The red region was excluded by DØ during Run II [21]. The brown region was excluded by the LEP experiment [22]. In the gray region, the squark mass is lower than the mass of the lightest neutralino. In the black hashed region there is no mSUGRA solution. The green region shows the area excluded by the present analysis with 371 pb^{-1} of CDF Run II data.

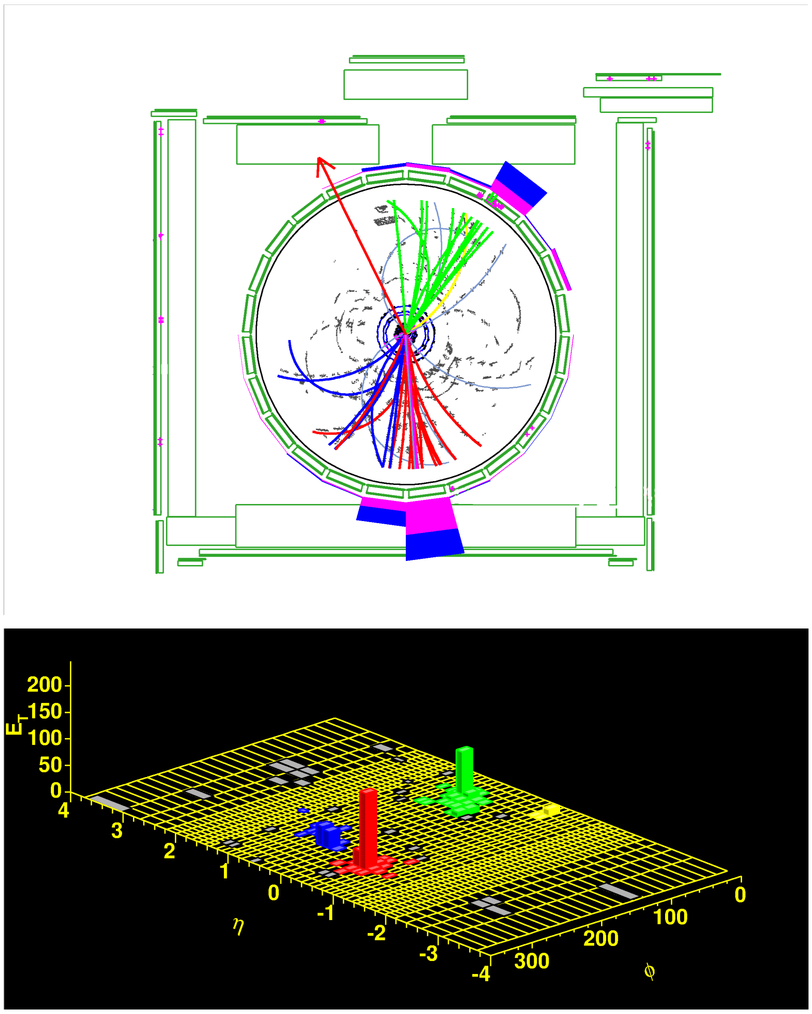

Figure 52: CDF central tracking chamber and calorimeter ($r-\phi$ view) (top) and Calorimeter "Lego" plot (bottom) for the event with the highest $\not\!\!E_T$ and $\mathrm{H_T}$. This event has three jets above 25 GeV ($E_T^1 = 236$ GeV, $E_T^2 = 150$ GeV, $E_T^3 = 84$ GeV) with $\mathrm{H_T} = 470$ GeV and $\not\!\!E_{\mathrm{T}} = 196$ GeV.

A Corrected $\not\!\!E_{\rm T}$ and Trigger Efficiency

A.1 Corrected $\not\!\!E_T$

The measured missing transverse energy is partially corrected for detector effects. The missing transverse energy, as measured in the calorimeter, is re-computed using average-corrected jet transverse energies for all the jets in the event. In addition, this procedure approximately accounts for remaining data vs Monte Carlo difference in calorimeter response via slightly different jet correction factors applied in data and Monte Carlo. In this analysis, no direct identification of muons is performed. Figure 53 shows the correlation between corrected and uncorrected missing transverse energy for the nominal and $\pm 1\sigma$ jet energy corrections. Figure 54 show the nominal distribution for different $\not\!\!E_T$ binnings. It can be observed that the measured $\not\!\!E_T$ is corrected by about 12% at low $\not\!\!E_T$ and the average correction decreases with increasing $\not\!\!E_T$. The r.m.s of the distribution indicates a rather broad correlation between raw and corrected $\not\!\!E_T$ at low values.

A.2 $\not\!\!E_T$ Trigger Threshold

We study the $\not\!\!E_T$ trigger efficiency in order to place the $\not\!\!E_{\rm T}$ pre-selection cut well above the trigger efficiency turn-on curve. The $\not\!\!E_T$ trigger that we are using (see Table 1) is a combined trigger in the sense that is requiring $\not\!\!E_{\rm T} > 25$ GeV at Level 1 (L1) and two jets of $E_T > 10$ GeV at Level 2 (L2). This trigger has been studied in detail by other analyses groups [23][24] and here we limited the discussion to show that no effects from the trigger are present in our final distributions given the selection criteria employed.

A.2.1 Level 1: $\not\!\!E_{\rm T} > 25$ GeV (L1_MET35)

To estimate the trigger efficiency, the high p_T muons (bhmu0d) and the Jet20 (gjt10d) data samples have been used. The efficiency is defined as

$$\epsilon(\not\!\!E_{\rm T}) = \frac{\rm N}{\rm N_T}$$

where N is the number of events from the unbiased trigger that pass the L1_MET35 requirement and N_T is the total number of events. Figure 55 show the turn-on curves. A 50 GeV value for the uncorrected offline $\not\!\!E_T$ is already in the plateau. This translates, using the mean value of the distributions in Figure 53, into a corrected $\not\!\!E_T$ value of 56 GeV, well below the final cut that we are applying (see section A.2.3).

A.2.2 Level 2: Two jets of $E_T > 10$ GeV (L2_MET35)

To study the L2 trigger efficiency, the pre-scaled trigger (PSMET25) for $\not\!\!E_T$ has been used. This trigger path is only asking for $\not\!\!E_{\rm T} > 25$ GeV at L1 and then it is pre-scaled

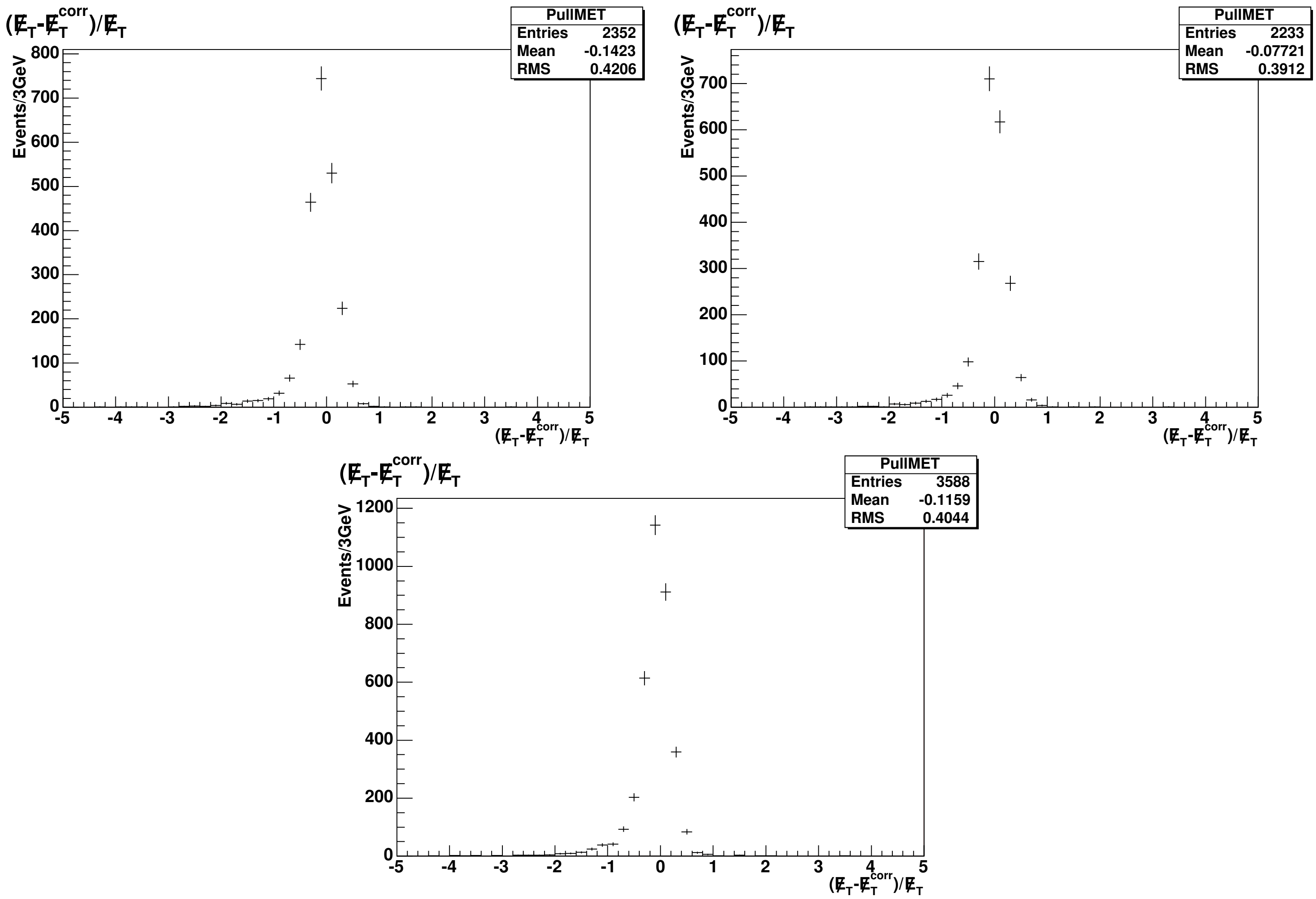

Figure 53: Relative difference between corrected and uncorrected $\not\!\!E_T$ varying energy scale systematics (top-left) $+1\sigma$, (top-right) -1σ and (bottom) nominal.

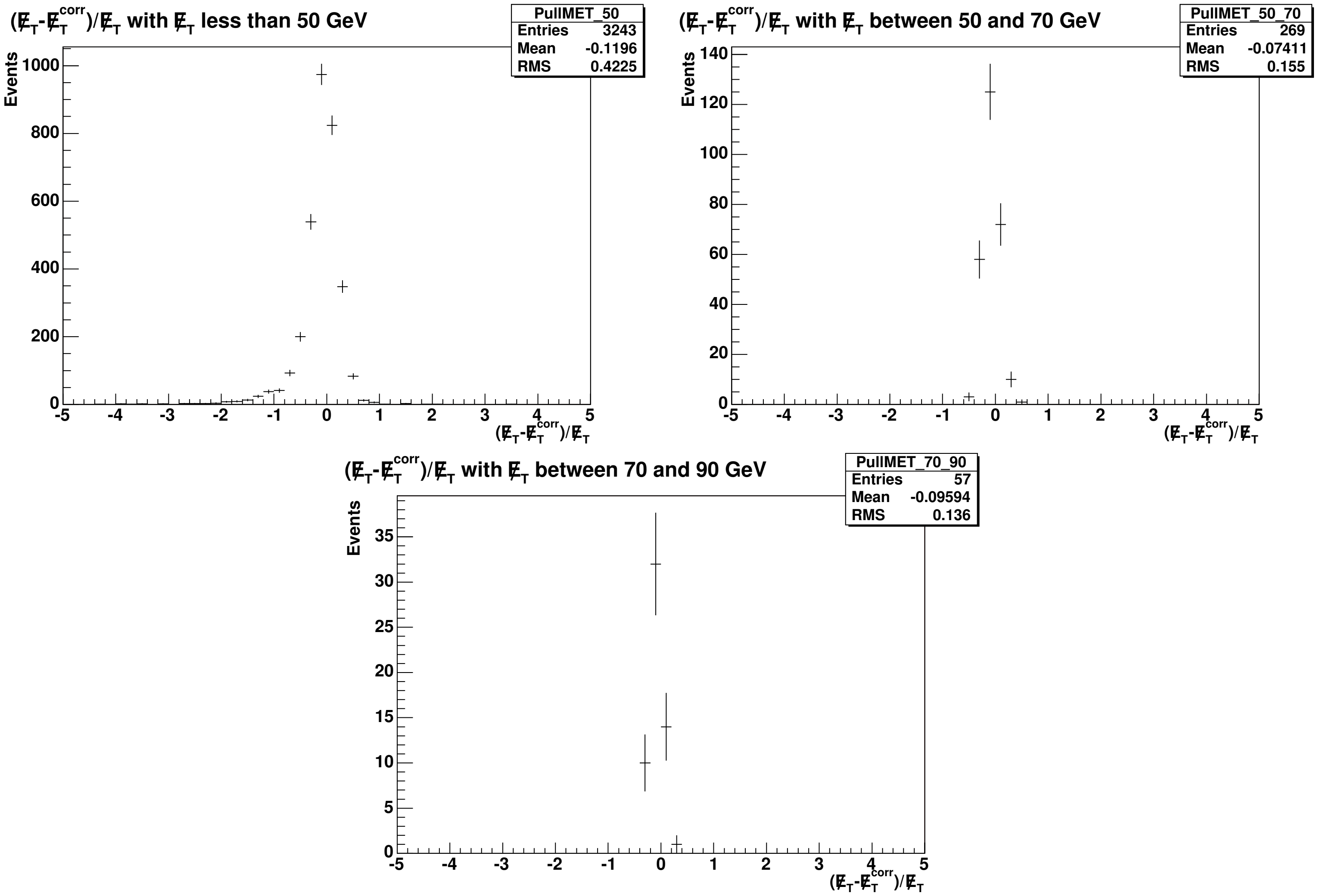

Figure 54: Relative difference between corrected and uncorrected $\not\!\!E_T$ considering different binnings of corrected $\not\!\!E_T$: (top-left) $\not\!\!E_{\mathrm{T}} < 50$ GeV, (top-right) $50 < \not\!\!E_{\mathrm{T}} < 70$ GeV and (bottom) $70 < \not\!\!E_{\mathrm{T}} < 90$ GeV.

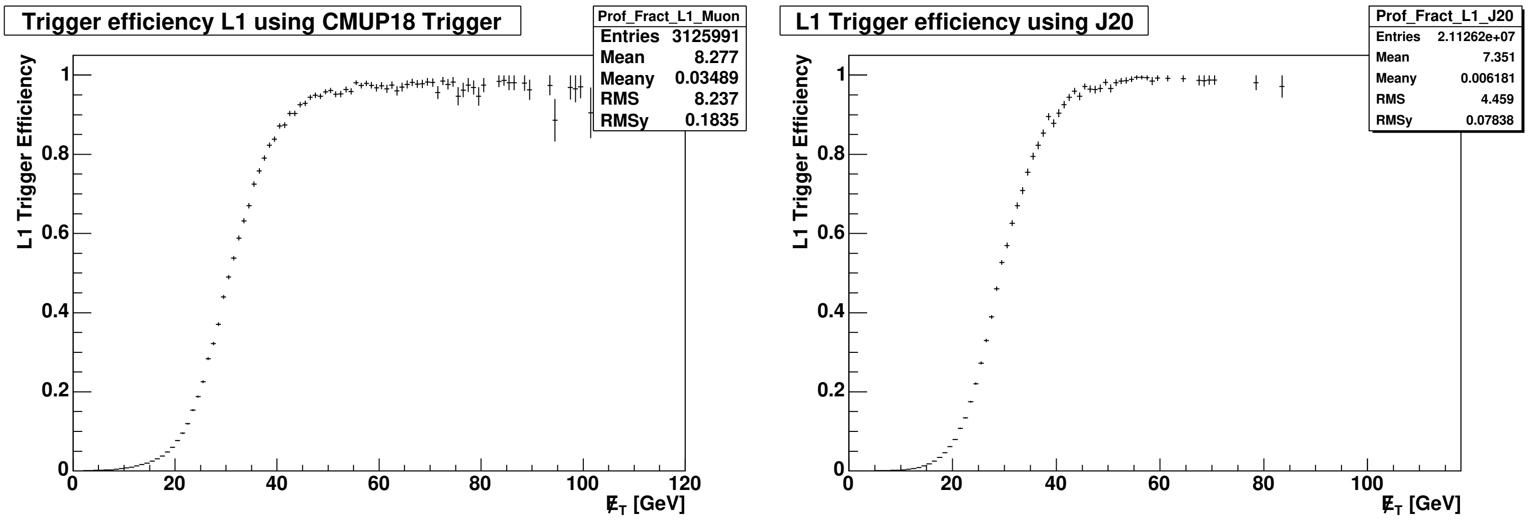

Figure 55: L1 trigger efficiency curve with respect to the offline $\not\!\!E_{\mathrm{T}}$ using high p_T muon sample (left) and Jet20 (right).

at the other levels but no further physical requirement is implemented. Therefore, we used:

$$\epsilon(E_T^{\text{2ndjet}}) = \frac{N}{N_T}$$

where N is the number of events from the PSMET25 trigger that passed the L2_MET35 requirement and N_T is the total number of events that are present in the PSMET25 trigger path. Note that the efficiency depend on the E_T of the second leading jet but there is not a direct dependence on the $\not\!\!E_T$.

The turn-on curve for L2 with the E_T of the second and the third jets can be seen in Figure 56. From the figures, the trigger achieves a 95% efficiency at 40 GeV for the second jet and at 25 GeV for the third. Table 14 shows the comparison of events from MET35 and PSMET25 trigger after each pre-selection cut used in the analysis.

Cut Applied	L1 MET25	+ L2 TWO-JET10
+ Vertex Cut	631723	249504
+ 3 jet Cut	25409	25251
+ Central jet	24561	24408
+ $\not\!\!E_{\mathrm{T}} > 70$ GeV	117	116
All Pre-sel. Cuts	99	99

Table 14: The center column is the number events passing the L1-MET25 trigger path along with any cut shown on the left column. The right column shows the number of events in the center column including the L2 TWO-JET10 trigger requirement. The numbers shown are not prescaled.

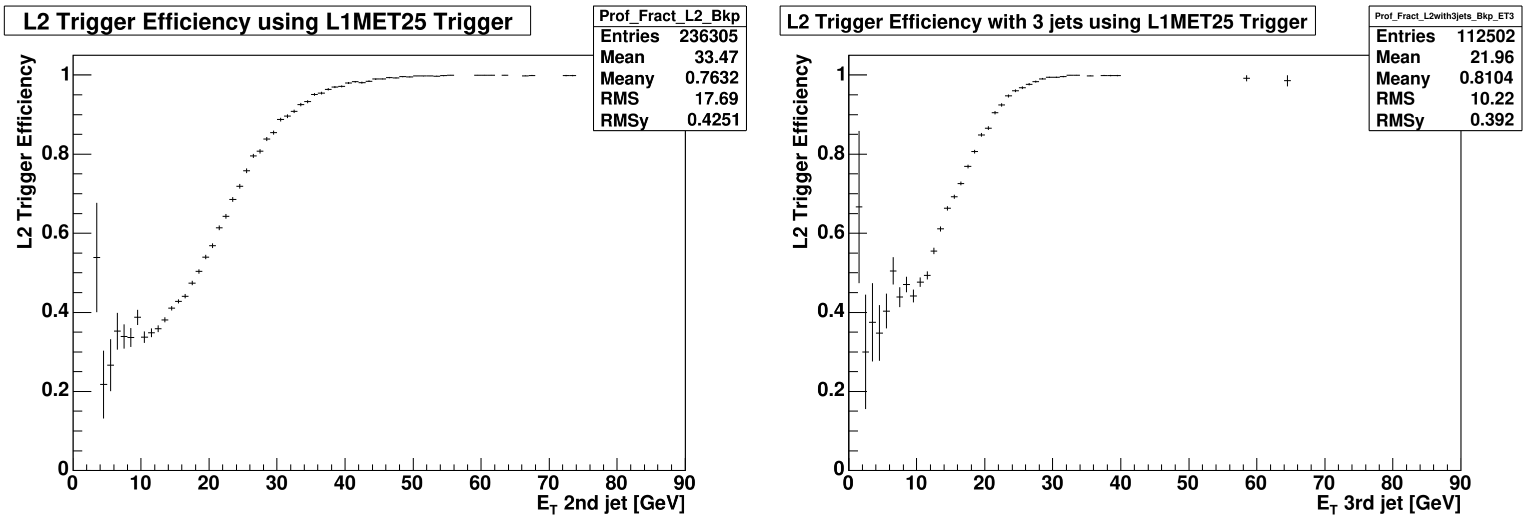

Figure 56: L2 trigger efficiency curve with respect to the transverse energy of the second jet (left) or the third jet (right). Both distributions are implemented using the pre-scaled missing transverse energy trigger.

A.2.3 Level 3: $\not{E}_{\mathrm{T}} > 35$ GeV (L3_MET35)

To study the L3 trigger the high p_T muon sample has been used. The efficiency has been defined as:

$$\epsilon(\not{E}_{\mathrm{T}}) = \frac{\mathrm{N}}{\mathrm{N_T}}$$

where now N is the number of events from the CMUP18 trigger that passed the complete MET35 trigger path and N_T is the number of events that passed the L1 and L2 requirements of the MET35 path. Figure 57 shows the turn-on curve with respect to the offline $\not{E}_T$. This figure has been used to decide the minimum $\not{E}_T$ cut to avoid trigger effects in the data used for this analysis. Being 50 GeV the value at 95% efficiency, we considered 60 GeV as the desirable threshold which takes into account the energy corrections fluctuations. This value becomes 67 GeV after applying the corrections to the $\not{E}_T$. Offline, we considered a final cut on 70 GeV.

B EEMF and ECHF Cuts

Beam-halo, beam-gas and cosmic rays are backgrounds, which are not reproduced by the Monte Carlo simulation. The EEMF and ECHF cuts proposed in section 2 help to reduce these type of backgrounds. However, the EEMF and ECHF cuts may require further explanation.

B.1 EEMF

Muons coming from the beam halo can deposit significant amounts of energy in the hadronic calorimeter causing a transverse energy imbalance. The purpose of the

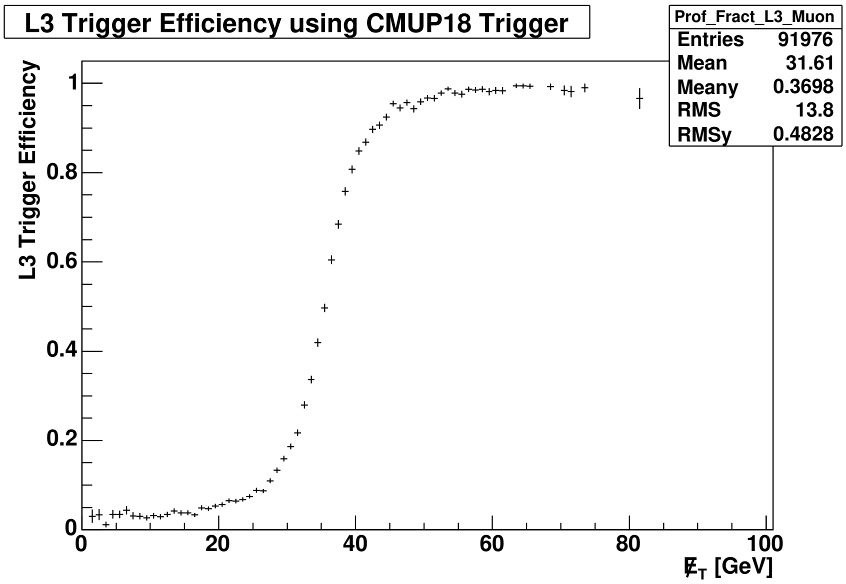

Figure 57: L3 trigger efficiency curve with respect to the offline $\not\!\!E_{\mathrm{T}}$ using high p_T muon sample

EEMF is to reject events of this kind. The EEMF is defined as:

$$\mathrm{EEMF} = \frac{\sum_{\mathrm{jets}} E_T^{\mathrm{jet}} \cdot f_{\mathrm{emf}}^{\mathrm{jet}}}{\sum_{\mathrm{jets}} E_T^{\mathrm{jet}}} \tag{16}$$

where $f_{\mathrm{emf}}^{\mathrm{jet}}$ is the fraction of the transverse electromagnetic energy of the jet, and the sum is performed over the three leading jets of the event.

It is expected that particles coming from the beam will deposit energy mainly in the hadronic calorimeter giving an EEMF close to zero. This situation can be seen in figure 58 where this quantity is shown for data and MC. We remove the major part of this background introducing a cut on EEMF > 0.15.

B.2 Track Validation

A dedicated study to validate the track definition given in section 2 was performed using the inclusive high $\mathrm{p_T}$ muon sample (bhmu0d). The integrated luminosity for the sample is 236 pb^{-1}, and the trigger path requires a CMUP track of 18 GeV/c.

We reconstructed the Z mass peak using the two highest isolated tracks in the event. To ensure that all the events correspond to $Z \to \mu\mu$ a tight mass constraint of $86 < \mathrm{M_{iso}} < 96$ GeV/c^2 was applied. Also, we required at least one central track with $|\eta| < 0.5$. Furthermore, a cosmic ray cut was applied. Figure 59 shows the reconstructed mass for data and Monte Carlo (ztop8i). The broader data distribution is understood as not all the corrections have been applied. Nonetheless, the normalization is fairly good: data has 24 events and Monte Carlo has 28 events in this region. We consider this enough to ensure a good definition for tracks in our selection criteria. As a final check the number of isolated tracks in our data sample

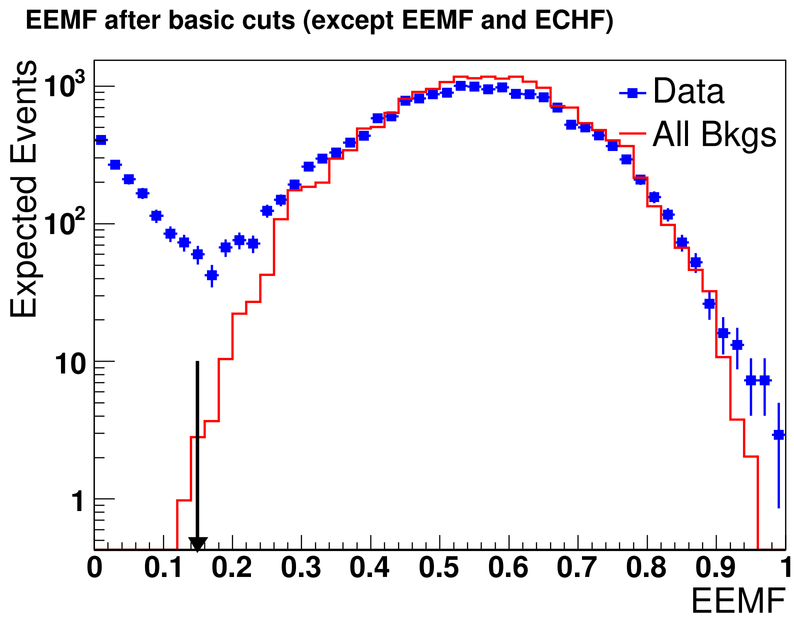

Figure 58: EEMF for data and MC. The plot includes the pre-selection (section 2 cuts except the cuts for EEMF and ECHF

used in the analysis with the one predicted by the MC just after the pre-selection cuts. The agreement is shown in Figure 60.

B.3 ECHF

Another characteristic of the beam background events is that tracks do not point to the region where the particle has deposited energy in the calorimeter. We define,

$$\mathrm{ECHF} = \frac{1}{N_{\mathrm{jets}}} \sum_{\mathrm{jets}} \frac{\sum_{\mathrm{tracks}} P_T^{\mathrm{track}}}{E_T^{\mathrm{jet}}}, \tag{17}$$

where the sum over jets consider only over central ($|\eta^{\mathrm{jets}}| < 1.1$) jets, among the three leading jets in the event, and the sum over tracks is done over all the ones pointing to the correspondent jet, using a cone of radius 0.4 around the jet direction. These tracks are required to pass the quality cuts described in section 2.

Figure 61 shows the ECHF distribution for data and MC. The shift seen in the data distribution with respect to the Monte Carlo is due to beam backgrounds in the sample.

C QCD Multijet Systematic Uncertainties

As discussed in [4], a good agreement is observed between QCD multijet data and the Monte Carlo predictions. Therefore, we concluded that no additional k-factor is needed to normalize the Monte Carlo predictions to the data. In that study, QCD

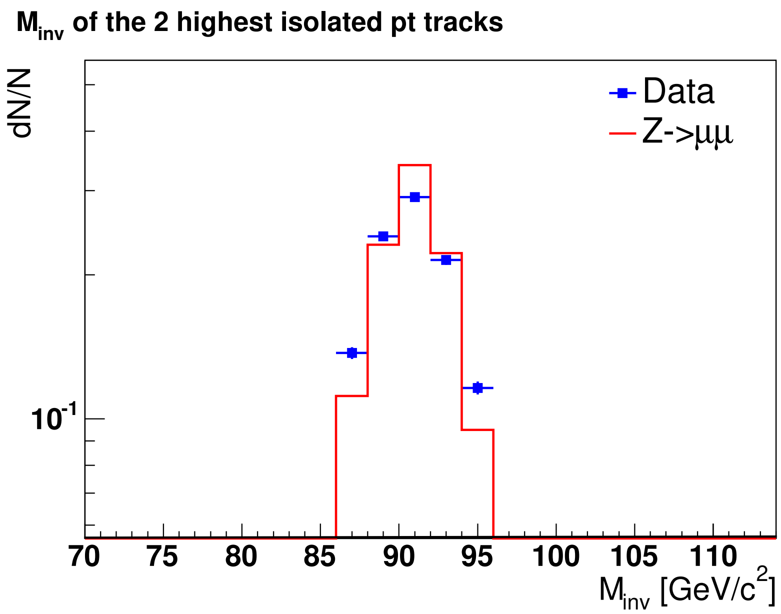

Figure 59: Invariant mass of the two highest isolated tracks for bhmu0d data and $Z \rightarrow \mu\mu$ Monte Carlo.

multijet events were selected applying a necessary cut on the $\not\!\!E_{\rm T}$ significance that removes beam-related backgrounds in the data, and allows a clean and well defined comparison with the Monte Carlo. As a consequence, most of QCD events with significant $\not\!\!E_{\rm T}$ were removed. However, the QCD events that constitute background to the mSUGRA analysis are characterized by the presence of large $\not\!\!E_{\rm T}$. A significant contribution comes from events with jets going into calorimeter cracks or close to the chimney region, where only a fraction of the jet energy is reconstructed.

Different quantities have been compared between data and Monte Carlo (see figures 62 through 64) to test the validity of the Monte Carlo description of the data for events with large $\not\!\!E_{\rm T}$, after pre-selection cuts as well as electron and muon removal cuts have been applied. The Monte Carlo distributions include a yellow band that reflects the uncertainty due to the calorimeter energy scale. The $\Delta\phi$ distribution between the $\not\!\!E_{\rm T}$ and each of the three leading jets in the event indicates, as expected, a dominant component for which the $\not\!\!E_{\rm T}$ is produced along the direction of the jets. A number of additional studies were carried out to further understand the origin of the small discrepancies shown in the distributions. Detailed comparisons were performed between data and Monte Carlo for jets reconstructed around the cracks, and the chimney regions. We conclude that the observed differences could be partially attributed to small defects on the simulation of the calorimeter response. After a cut on $\Delta\phi(\text{jet}, \not\!\!E_{\rm T}) > 0.7$ is applied (see figures 65 through 67), most of the QCD multijet background is removed and the discrepancies are within systematics.

The rather conservative systematic uncertainties on the QCD Monte Carlo normalization account for the remaining differences between data and Monte Carlo which, in addition to the energy scale, includes a 20 % uncertainty from PDFs and a 10 %

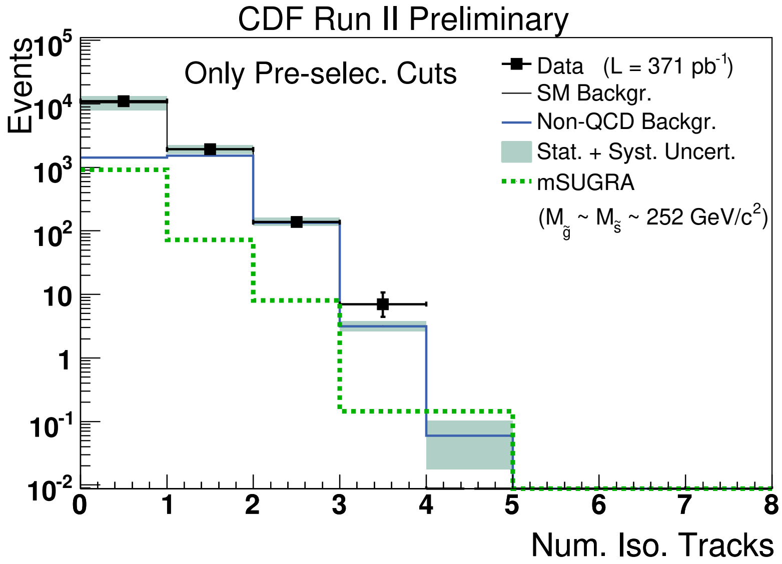

Figure 60: Number of isolated tracks just after the pre-selection cuts using the emet0d data sample.

uncertainty from hard scale dependencies. Figure 68 shows the $\not\!\!E_T$ and the $\mathrm{H_T}$ distributions after the pre-selection cuts. Figure 69 shows the $\not\!\!E_T$ and $\mathrm{H_T}$ distributions with all the systematics and after all other cuts are applied. The agreement between data and MC is good in all the zones.

The $\Delta\phi(\mathrm{jet}, \not\!\!E_\mathrm{T})$ and the EMF requirements were reversed to enhance the QCD and Boson+jets electromagnetic backgrounds separately, and test that the Monte Carlo properly describes each different background contribution (see figures 70 to 71). In addition, the muon contribution has been studied reversing the muon cuts (asking for at least one isolated track) as shown in Figure 72. All the distributions show a reasonable agreement between data and Monte Carlo.

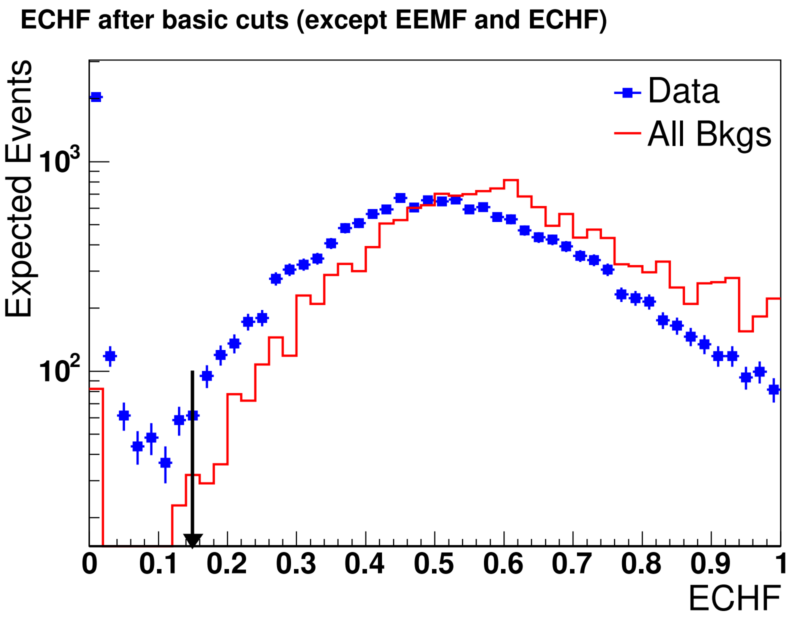

Figure 61: ECHF for data and MC. The plot includes the pre-selection (section 2 cuts except the cuts for EEMF and ECHF.

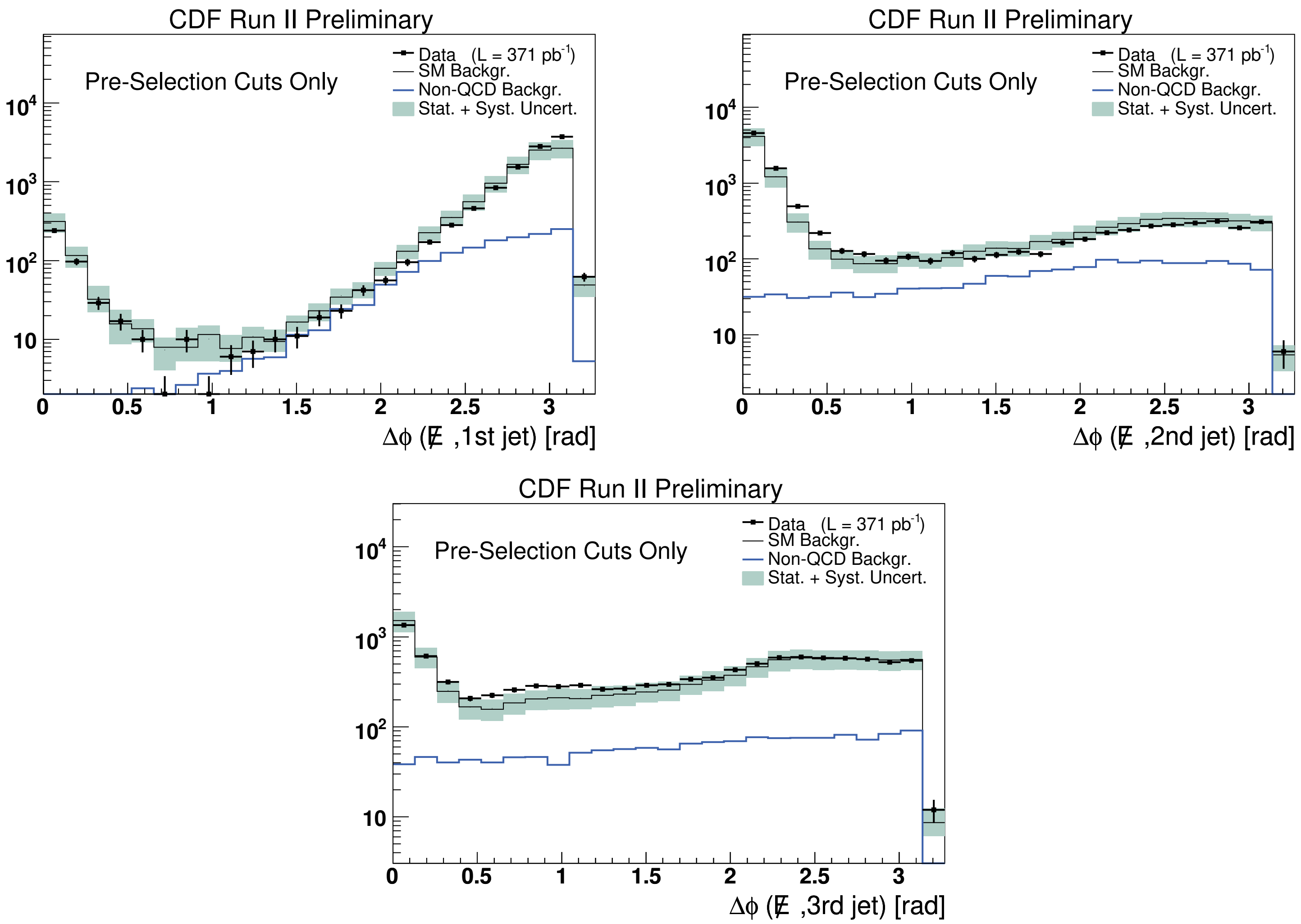

Figure 62: Azimuthal distance between $\not\!\!E_T$ and E_T of the three leading jets for data and MC after pre-selection, electron and muon removal cuts have been applied.

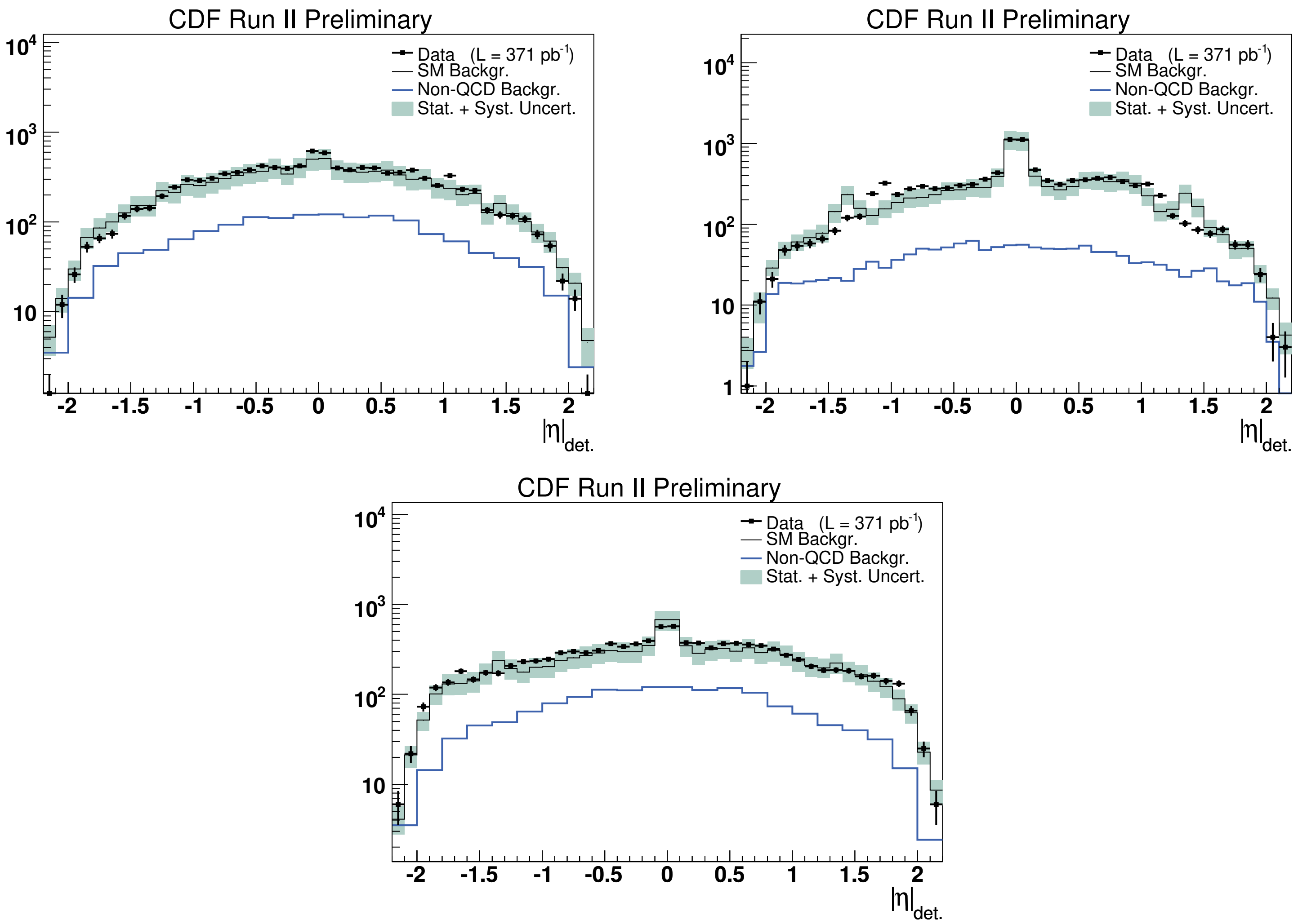

Figure 63: Detector η of the three leading jets for data and MC after pre-selection, electron and muon removal cuts have been applied.

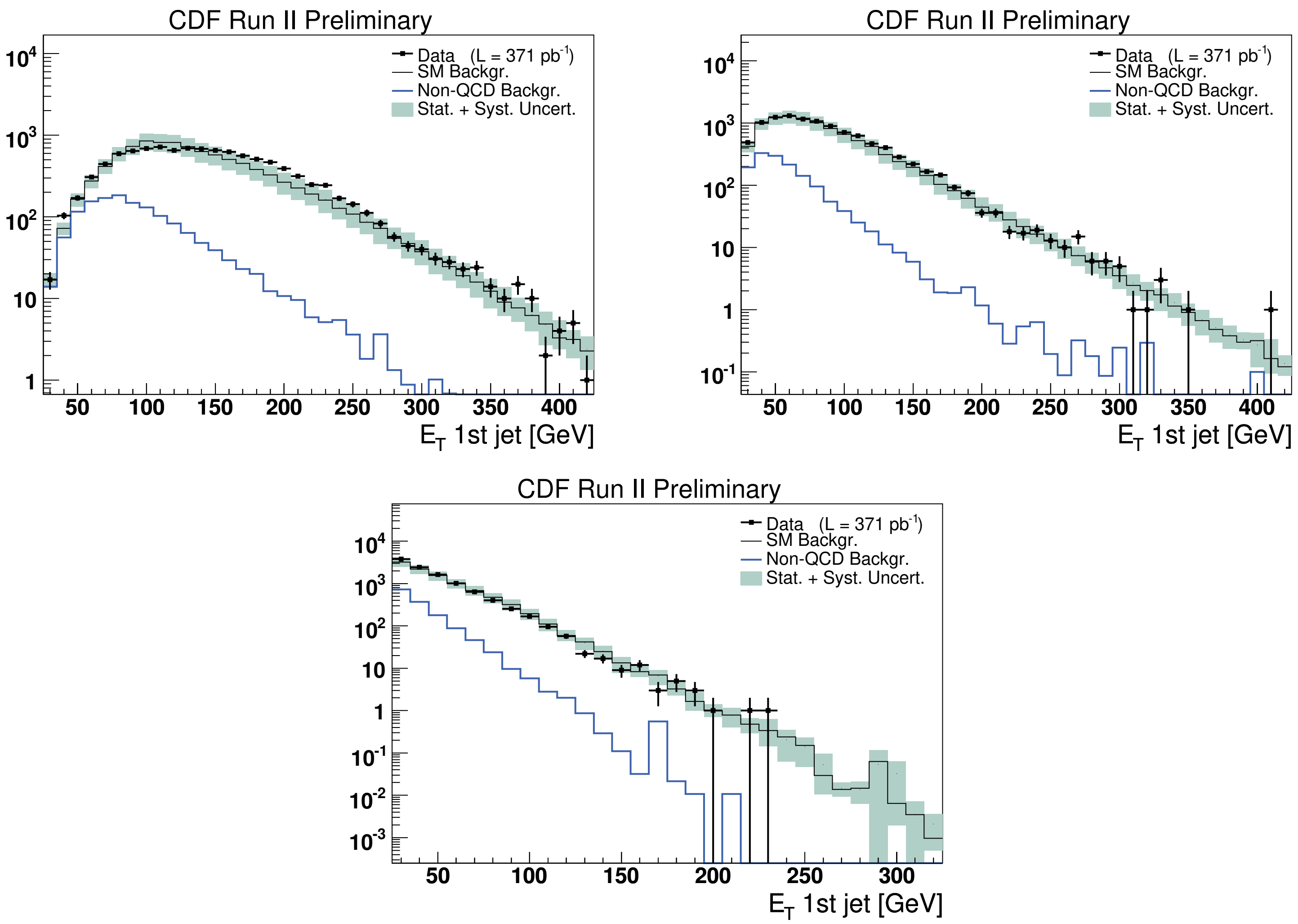

Figure 64: E_T of the three leading jets for data and MC after pre-selection, electron and muon removal cuts have been applied. There are 10551 data events and $9.87^{+1.35}_{-2.33} \cdot 10^3$ Monte Carlo events in the plots.

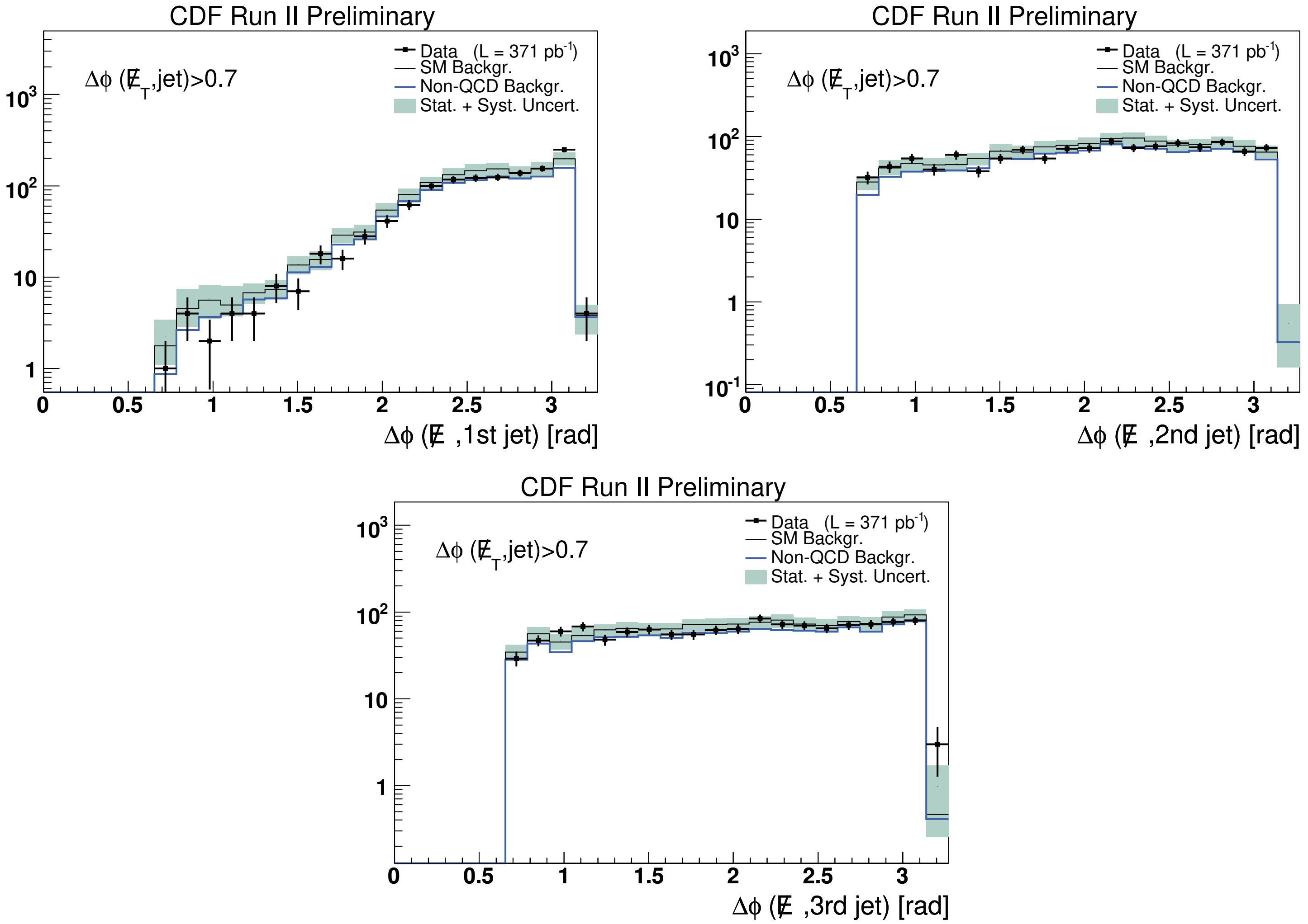

Figure 65: Azimuthal distance between $\not{E}_{\mathrm{T}}$ and $\mathrm{E_T}$ of the three leading jets for data and MC after the $\Delta\phi(\not{E}_{\mathrm{T}}, \mathrm{jets}) > 0.7$ cuts. Pre-selection, electron and muon removals cuts have also been applied. There are 1204 data events and $1.29^{+0.14}_{-0.17} \cdot 10^3$ MC events in the plots.

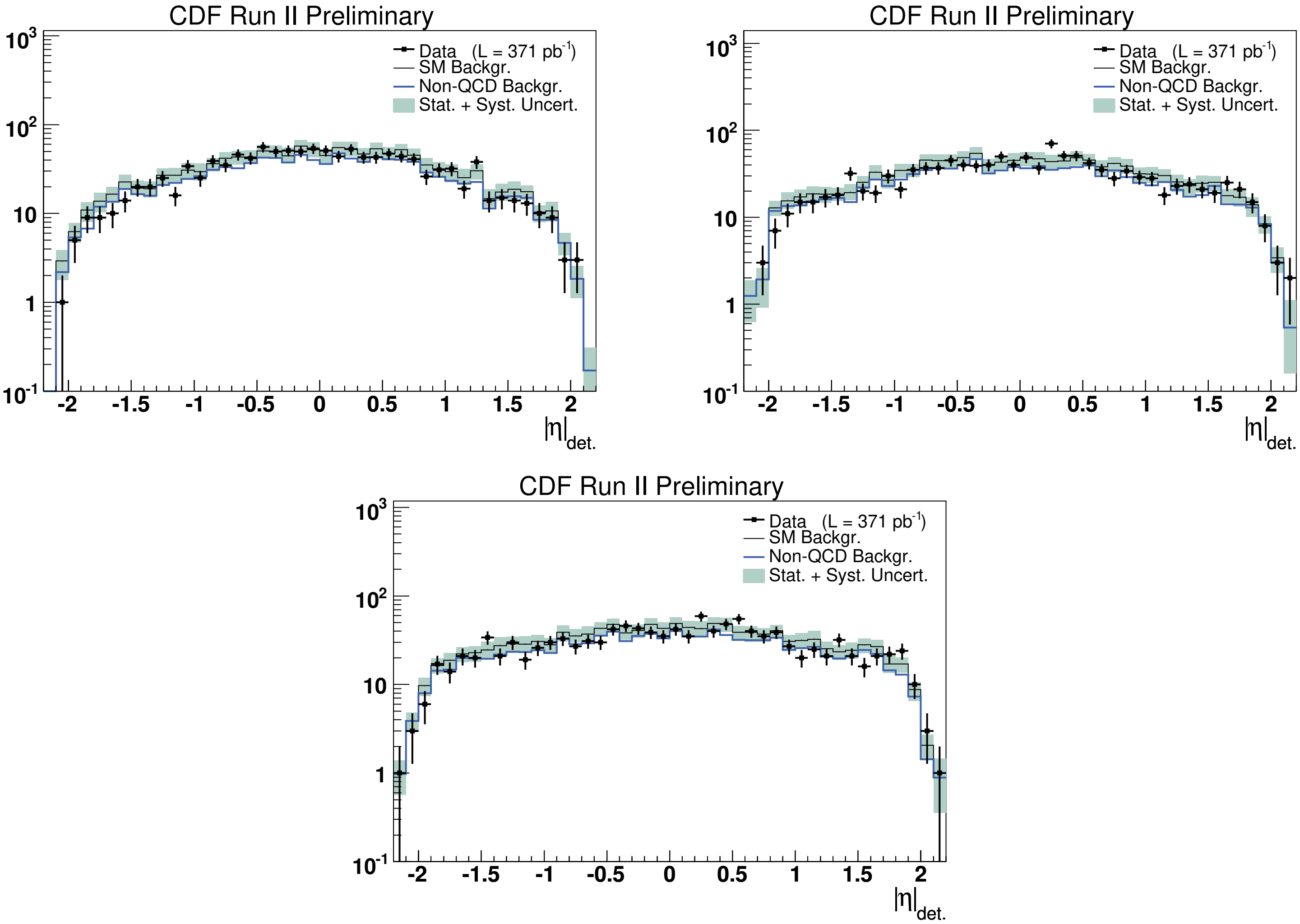

Figure 66: Detector η of the three leading jets for data and MC after the $\Delta\phi(\not{E}_T, \text{jets}) > 0.7$ cuts. Pre-selection, electron and muon removals cuts have also been applied.

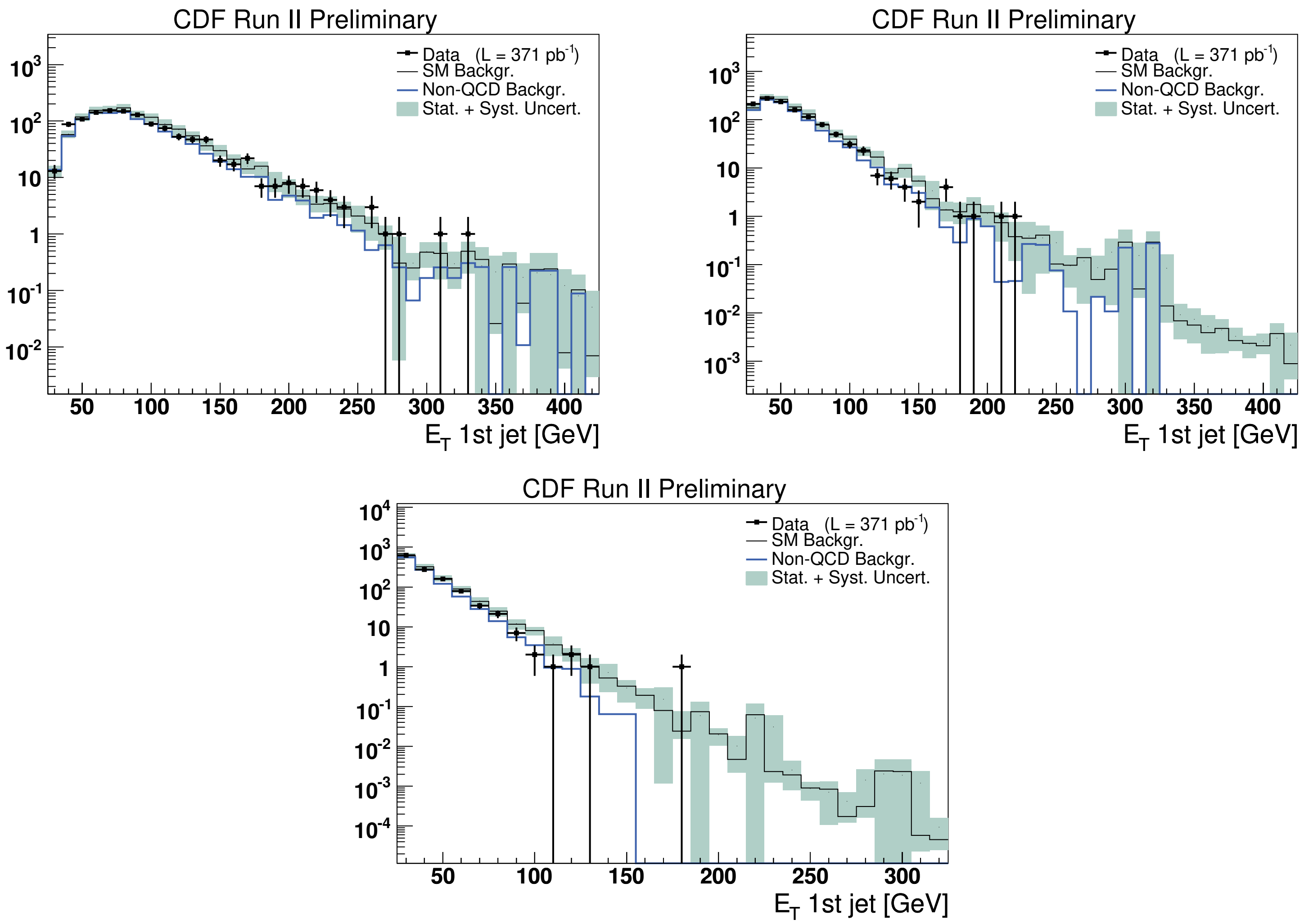

Figure 67: $\mathrm{E_T}$ of the three leading jets for data and MC after the $\Delta\phi(\not{E}_{\mathrm{T}}, \mathrm{jets}) > 0.7$ cuts. Pre-selection, electron and muon removals cuts have also been applied.

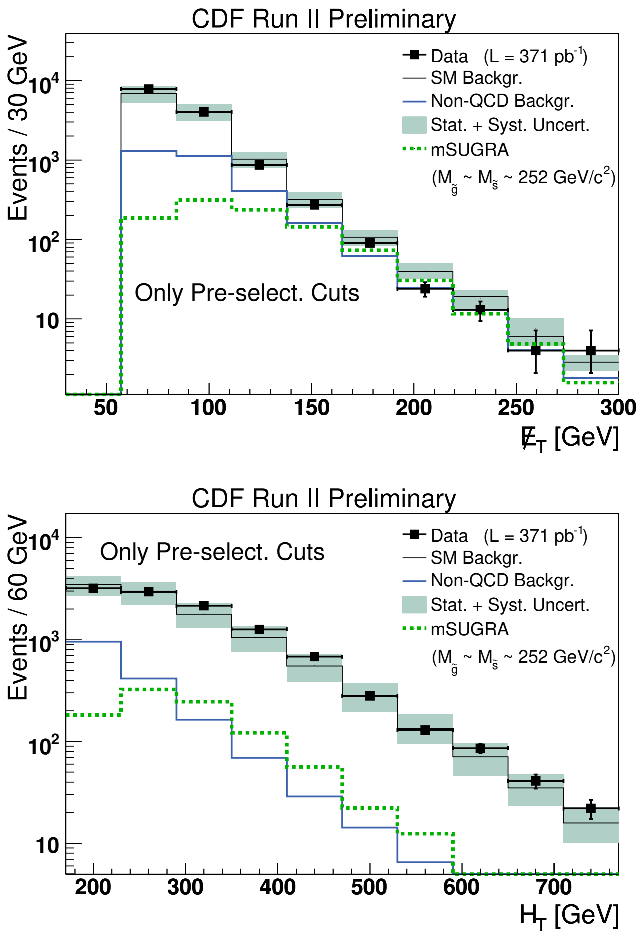

Figure 68: $\not\!\!E_T$ and H_T just after the pre-selection cuts.

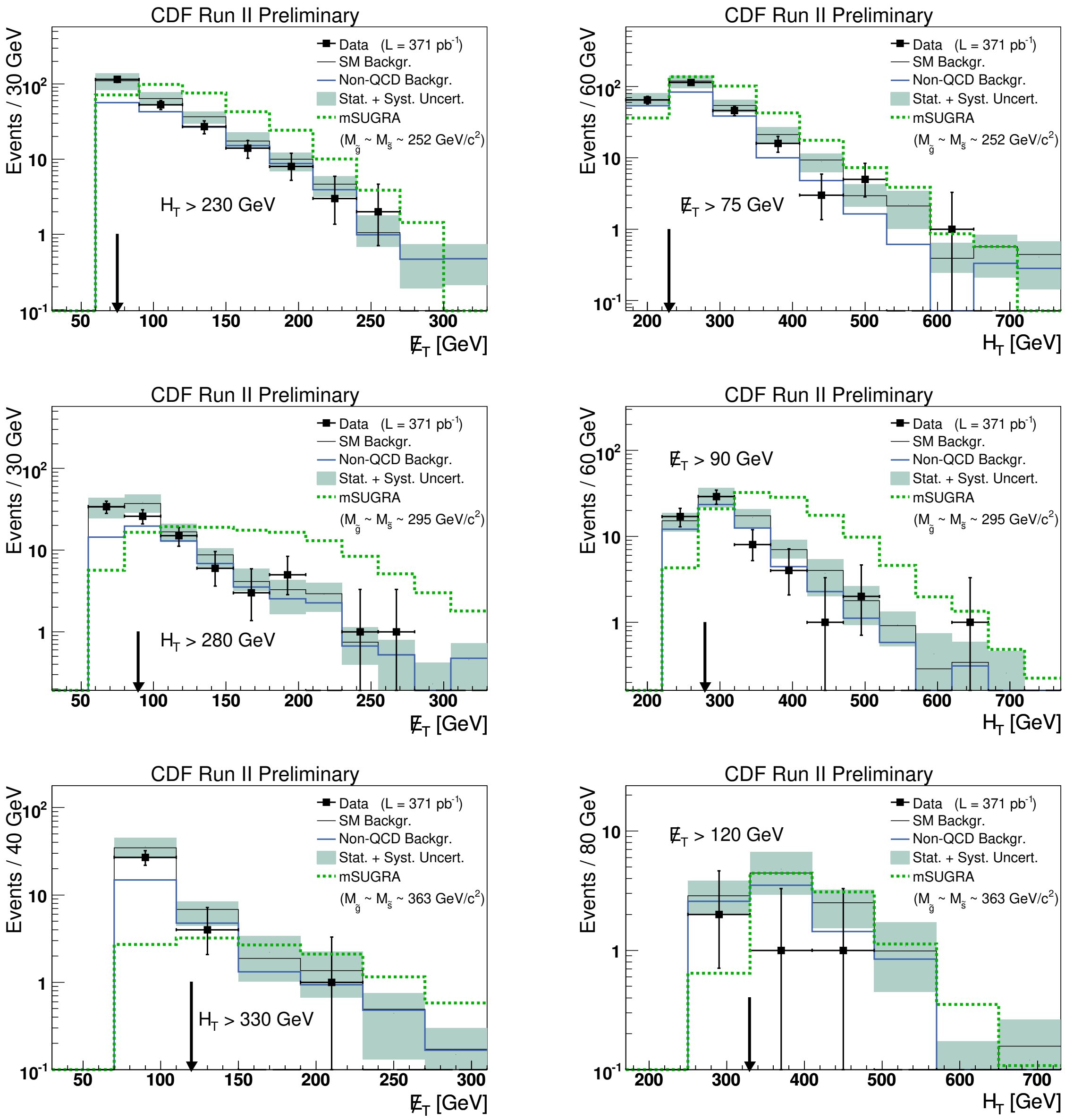

Figure 69: $\not\!\!E_T$ and H_T after all cuts in the analysis except the $\not\!\!E_T$ and H_T cuts respectively, but reversing the $\Delta\phi(\not\!\!E_T, \mathrm{jets}) > 0.7$ cut by asking at least one of the three jets to fail the condition. All three zones are shown.

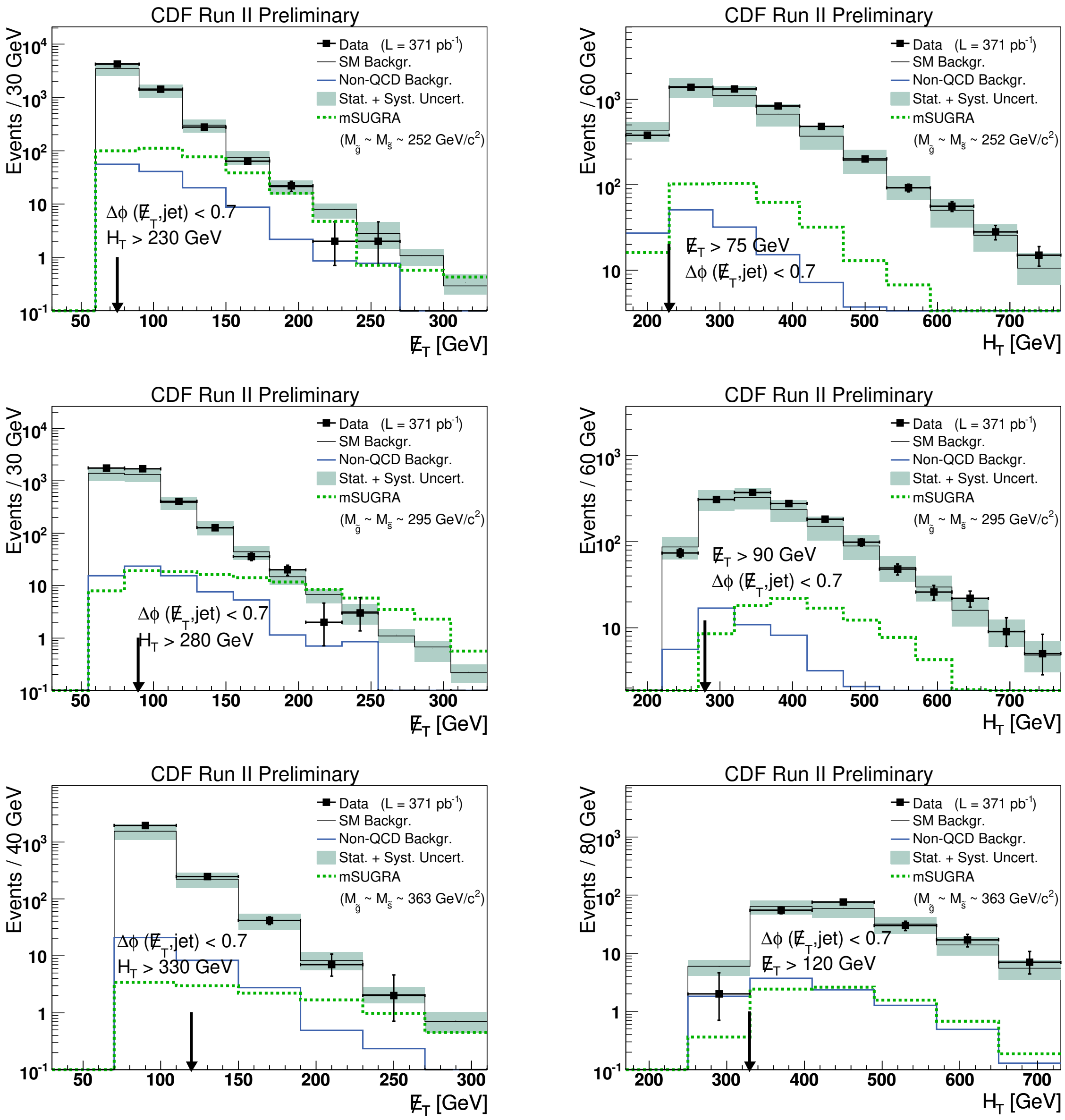

Figure 70: $\not{E}_{\mathrm{T}}$ and $\mathrm{H_T}$ after all cuts in the analysis except the $\not{E}_{\mathrm{T}}$ and $\mathrm{H_T}$ cuts respectively, but reversing the $\Delta\phi(\not{E}_{\mathrm{T}}, \mathrm{jets}) > 0.7$ cut by asking at least one of the three jets to fail the condition. All three zones are shown.

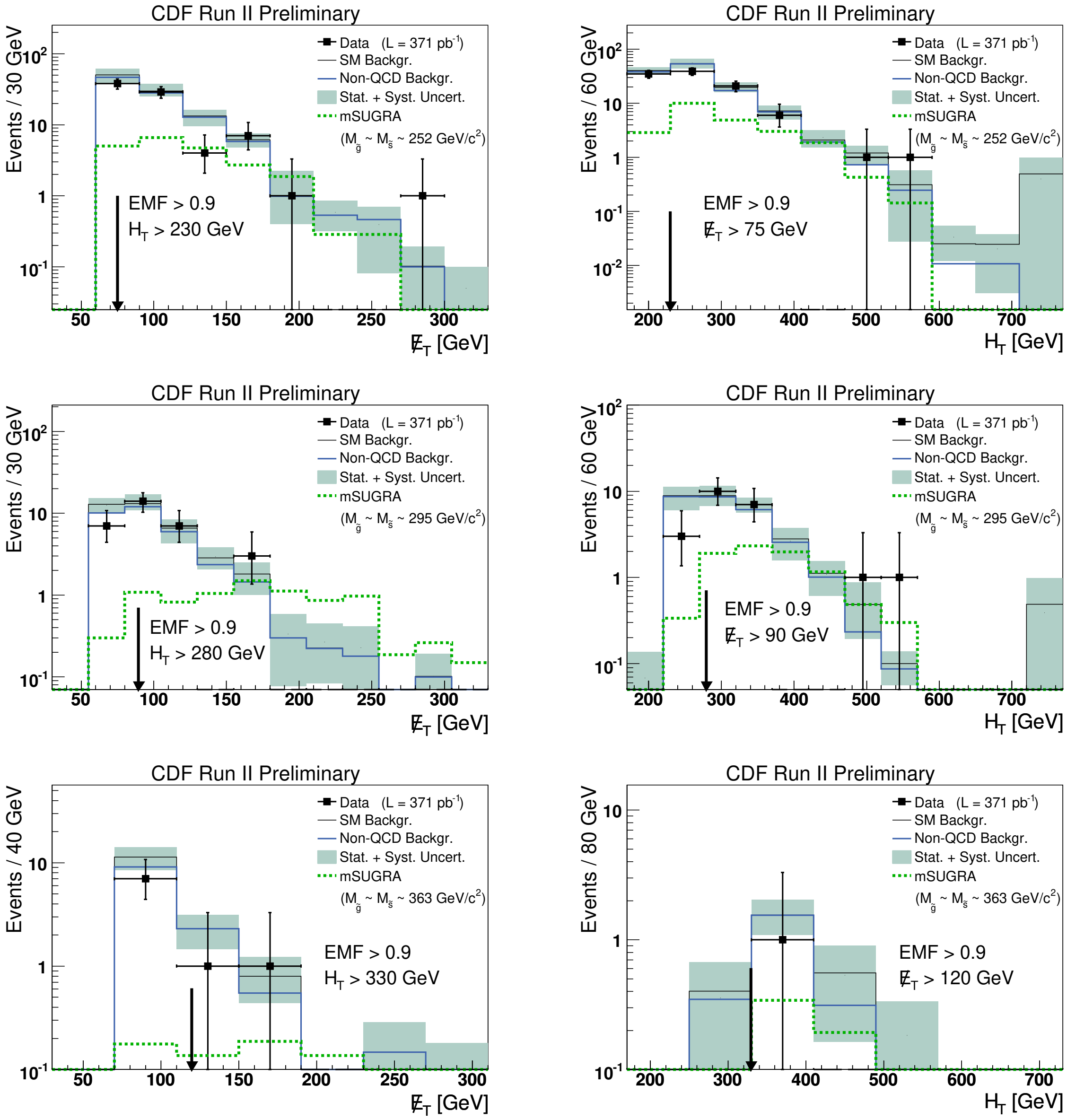

Figure 71: $\not\!\!E_T$ and H_T after all cuts in the analysis except the $\not\!\!E_T$ and H_T cuts respectively, but reversing the EMF > 0.9 cuts by asking at least one of the three jets to fail the condition. All three zones are shown.

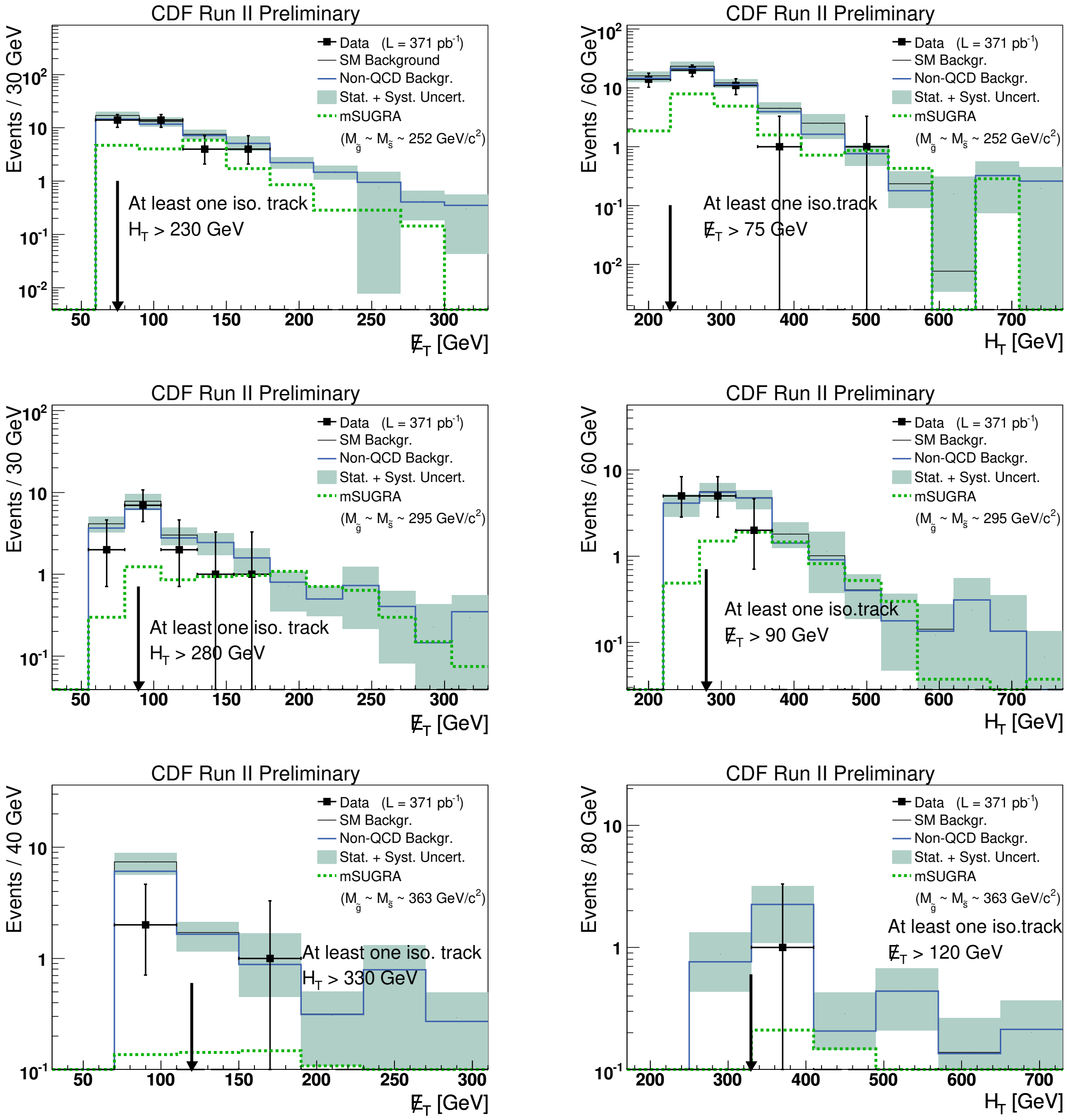

Figure 72: $\not\!\!E_T$ and $\mathrm{H_T}$ after all cuts in the analysis except the $\not\!\!E_T$ and $\mathrm{H_T}$ cuts respectively, but enhancing the muon contribution by requiring at least one isolated track. All three zones are shown.